FINAL REPORT

Characterization of Freshwater EM Sub Bottom Sediment Properties and Target Responses for Detection of UXO with Ground-Penetrating RADAR (GPR)

SERDP Project MM-1440

September 2008

Dr. Steven A. Arcone
ERDC/CRREL

Strategic Environmental Research and Development Program

Report Documentation Page

Form Approved
OMB No. 0704-0188

1. REPORT DATE	2. REPORT TYPE	3. DATES COVERED
SEP 2008		**00-00-2008 to 00-00-2008**

4. TITLE AND SUBTITLE	5a. CONTRACT NUMBER
Characterization of Freshwater EM Sub Bottom Sediment Properties and Target Responses for Detection of UXO with Ground-Penetrating RADAR (GPR)	5b. GRANT NUMBER
	5c. PROGRAM ELEMENT NUMBER
6. AUTHOR(S)	5d. PROJECT NUMBER
	5e. TASK NUMBER
	5f. WORK UNIT NUMBER
7. PERFORMING ORGANIZATION NAME(S) AND ADDRESS(ES) **Engineering Research & Development Center,Cold Regions Research and Engineering Laboratory (CRREL),72 Lyme Road,Hanover,NH,03755-1290**	8. PERFORMING ORGANIZATION REPORT NUMBER
9. SPONSORING/MONITORING AGENCY NAME(S) AND ADDRESS(ES)	10. SPONSOR/MONITOR'S ACRONYM(S)
	11. SPONSOR/MONITOR'S REPORT NUMBER(S)

12. DISTRIBUTION/AVAILABILITY STATEMENT
Approved for public release; distribution unlimited

13. SUPPLEMENTARY NOTES

14. ABSTRACT

15. SUBJECT TERMS

16. SECURITY CLASSIFICATION OF:			17. LIMITATION OF ABSTRACT	18. NUMBER OF PAGES	19a. NAME OF RESPONSIBLE PERSON
a. REPORT **unclassified**	b. ABSTRACT **unclassified**	c. THIS PAGE **unclassified**	**Same as Report (SAR)**	**66**	

Characterization of freshwater EM subbottom sediment properties and target responses for detection of UXO with Ground-Penetrating Radar (GPR)

SERDP Military Munitions Project UX 1440

Final Report: 2005-2007

December 1, 2007

PI: Steven A. Arcone
ERDC/CRREL
72 Lyme Road
Hanover, NH 03755-1290
Steven.A.Arcone@ERDC.usace.army.mil

SUMMARY

This project has answered the SERDP statement of need (SON) for site characterization and remediation technology to detect and characterize underwater UXO; i.e., existing within freshwater river or lake bottom sediments. Our objectives have been to prove and quantify the penetration of 100−400 MHz ground-penetrating radar (GPR) signals within freshwater subbottom sedimentation, and to define the electromagnetic and geologic matrix profile characteristics of buried, single, typical targets. Our approach is primarily field experimentation and observation, supported by laboratory experiments and numerical modeling designed to interpret the field data. Our most important field work has centered on a survey of JEP (JEP), a heavily UXO contaminated lake in New England. Our most important laboratory work has centered on resolving the causes of high attenuation in wet fine-grained sediments, as a proxy for any lake bottom material. Our most important findings are: 1) Likely UXO provide unique pulse waveform phase signatures that distinguish UXO from false targets; 2) UXO create their own stratigraphic disturbances such as small craters, new layers and draping of overburden sedimentation; 3) Resonance signatures are likely false metal targets; and 4) Subbottom penetration of as much as ten meters are likely to be caused by the lack of phyllosilicate clay minerals. At the time of this report, we have published one journal article with another accepted, two conference papers at the SERDP-supported Intl. Conf. on GPR, abstract presentations at Spring-06 and 07 AGU conferences and at URSI-07; 4 poster presentations at SERDP Symposia and support of one student and an MS thesis. Collaboration includes Prof. Lanbo Liu (numerical modeling, Univ. Conn.), Prof. Ben Bostick (X-Ray Diffraction, Dartmouth College) and Mr. Garry Kozak (side scan sonar, private consultant). Our technical outreach includes technology demonstrations to the Army (Ft. Greely, AK) and particularly to the Air Force (New Boston AFS, New Boston, NH). Involvement with GPR UXO detection will extend through 2008.

BACKGROUND AND PURPOSE

This project has answered the SERDP statement of need (SON) for site characterization and remediation technologies to detect and characterize underwater UXO; i.e., existing within freshwater river or lake bottom sediments. Lakes, rivers and wetlands are common on many military bases, especially within artillery and bombing ranges, some of which have been mandated for closing and conversion to public use. In at least one case (investigated here and not well known) a small lake itself was the actual bombing range; artillery exercises in Lake Erie are well known. Many ranges have been in use since the 1930s, but environmental mapping of stray ordnance has been implemented on some bases only within the last 20 years. Of particular concern are dangers associated with shallow lakes because UXO are then close to waders, fishermen, motors and paddles. Lakes and ponds may dry up and leave buried UXO dangerously close to the surface. The technology we offer and demonstrated in this project is ground-penetrating radar (GPR), a competing method against SONAR (sound navigation and ranging). As does SONAR, GPR can delineate subbottom strata and detect localized objects within it to decimeter resolution or better. Unlike SONAR, GPR is able to operate from either an ice or a water platform, propagate within a heavy suspended load, is not affected by vegetation or gaseous sediments, is not subject to masking reverberation in shallow water, and is far less expensive.

The purpose of this project has been to provide information and understanding of the interaction of pulsed GPR electromagnetic signals with UXO (unexploded ornance) targets embedded within a matrix of lake bottom stratigraphy. This will improve the ability of surveyors to identify and possibly characterize UXO. The project was based primarily on three hypotheses: 1) Buried UXO are detectable by a phase signature that is unique because metal is of higher complex permittivity than water and saturated sediments, whereas most other false targets such as logs and rocks have lower permittivity and produce the opposite phase in such an environment; 2) Radiowave penetration of at least 1–5 or more meters is generally the rule and enough to detect most UXO; and 3) Buried objects will likely distort stratigraphy in telltale manners. As such, our objectives were based on testing these hypotheses. They are:

Objectives of the project

1. Prove and quantify the penetration of 100−800 MHz GPR signals within freshwater subbottom sedimentation.

2. Determine the controls upon the dielectric properties of high water content, fine grain sediments typical of lake subbottom sedimentation.

3. Define the GPR pulse response to UXO within the geologic matrix of subbottom sedimentation.

4. Define the GPR pulse response to distortions and disruptions of the geologic matrix of subbottom sedimentation.

5. Describe the logistics needed to implement GPR for ordnance detection and characterization.

APPROACH

Our primary approach consists of field observations and field experimentation with GPR, which we carried out during the three years of this project. We complemented this with simplified field exercises of controlled UXO detection, numerical modeling of target responses, and laboratory investigations of sediment complex permittivity to aid our interpretation of field data.

In the field we used well developed commercial 16-bit GPR technology, which has never been applied to characterizing freshwater subbottom targets and their effect on the well developed stratigraphy of lake bottoms. The advantage of GPR is the shortening of its wavelengths by the high refractive index of water and saturated sediments. This shortening affords cm resolution of targets, and therefore the possibility of imaging larger targets such as bombs, or their effects upon the geologic matrix.

In the laboratory we adapted well known procedures to implement the time domain spectroscopy technique and applied it to measure the frequency dependent properties of wet sediments. In this method a pulse is reflected from a sediment sample and from a metal reflector, and the two reflections are then analyzed for their comparative Fourier components. The resulting ratios are used to calculate the complex permittivity at each frequency. There is no commercially available system for this; we developed our own system following the work of others. We are able to vary frequency over 6 orders of magnitude.

Numerically, we used pseudospectral finite element modeling to find the response of cylindrical targets and flat plates to GPR pulse excitation. The technique has been evolving for about the last 30 years. We are now able to perform calculations in 3-D, but 2-D suffices for this project.

Our work provides the scientific basis, technology and associated procedures to enable military bases to cost effectively characterize a site, estimate UXO presence, size and depth, and estimate extraction costs. Development will apply to survey procedures, antenna deployment and integration with GIS information systems.

By far the most significant accomplishments have been in the survey results of Joe English Pond (JEP) and the dielectric measurements of sediments. The rest of this report is a synthesis of three journal articles, one published, the second accepted for publication and the third in preparation. Our published article discusses the cause of resonances in GPR reflection profiles. Our journal article on complex permittivity was accepted 2 Dec, 2007. Our journal article in preparation is on the results of JEP and awaits a cleanup demonstration by the Air Force scheduled for spring, 2008.

Field methods: Sites and GPR

JEP

The main bombing area of JEP is approximately 500 m in maximum dimension and 8.5 m maximum depth (**Figure 1**). Sample water conductivity σ at the time of our survey June 14, 2006, ranged from 0.0037 to 0.0047 S/m and water temperature was 21–22^0 C. The lake is fed by a few streams, and is dammed at one end, which raises the level approximately 2 m. Therefore, much of the shallow area was not submerged before damming (date not known). JEP is surrounded by hills, which contain bomb craters and are posted for UXO. One UXO just above JEP was found in October 2006.

The area was formerly glaciated. The local direction of glacial flow was north to south and the surficial geology was mapped generically as till (Goldthwait, 1950), which we take to mean either lodgment till (densely compacted beneath an ice sheet), with or without a cover of

ablation till (less compacted englacial material). Nearby terrestrial GPR profiles showed clear bedrock responses but no significant overlying stratigraphy. The primary sediment input to the lake is silt-rich, most of which likely occurs in Spring, and is likely to be similar to that beneath

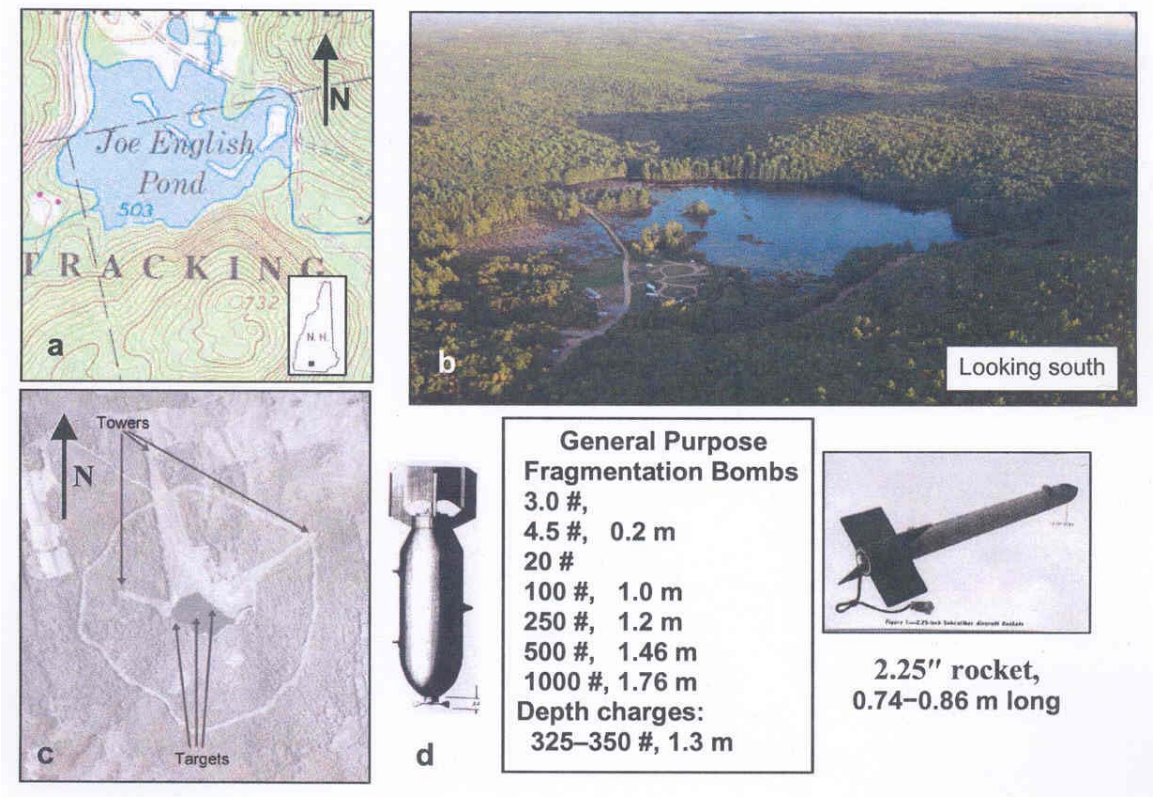

Figure 1. JEP topographic map and locations (a), aerial oblique photograph (b), high altitude photograph showing location of targets and 0bservatgion towers (c), and inventory of most used munitions with weight in pounds (#) and lengths in meters (m) or inches(″) if available (d).

nearby Squam Lake, discussed next. The underlying bedrock are metasedimentary slates and sandstones of the Littleton formation (Billings, 1955; Lyons et al., 1997), the ε of which are likely to lie between 6 and 10 given the strong presence of mica and quartz. Subbottom sampling by us was not permitted, but was later carried out by Shaw Environmental of Baltimore, MD for contaminant testing. Their bottom samples were superficial (surface only) and supersaturated and therefore probably not characteristic of the subbottom (probably contains metal fragments and explosive by products; after all, most bombs did explode).

Figure 2 shows transects superimposed on an aerial photograph of the lake. The labeled transects are discussed below. The transects cover areas in which water depth ranged from about 1–8.5 meters. The circle encompasses the approximate area of the main basin where depths ranged from about 5–8.5.

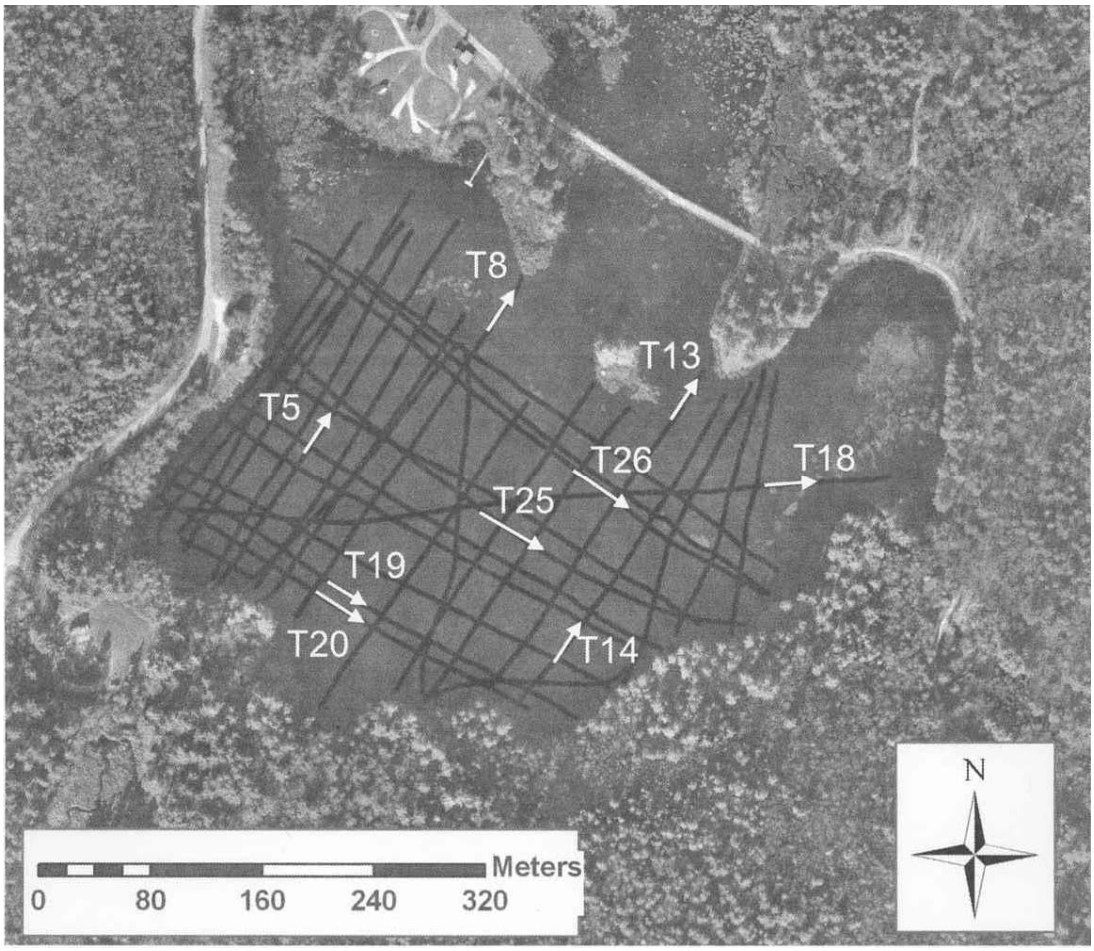

Figure 2. Transects on JEP for the 135-MHz survey, recorded June 14, 2006. Segments from the labeled transects are discussed here.

Squam Lake

Squam Lake is located in central New Hampshire (**Figure 3**). We measured $\sigma = 0.004$ at several locations. We recorded several profiles over the deepest part during September, 2006 at 60- and 135-MHz. In particular, we recorded many profiles in Squaw Cove because of its similar stratigraphy to that of JEP. Squaw Cove is located in the northern part, has a relatively high rate of sedimentation (Jeffrey Shloss, Univ. NH, personal communication, 2006) and is used for ongoing environmental studies. The maximum depth in Squaw Cove was about 8 m.

Glacial flow across the area was mainly NNW to SSE and the surrounding sediments are mapped as till (Goldthwait, Surficial Geology of NH, 1950). Later we discuss sediment analysis from this lake, which verifies the quartz-rich nature of both the silt and clay fractions. The underlying bedrock is quartz diorite (Billings, Geological map of NH, 1955), which is likely to have $6 < \varepsilon < 8$.

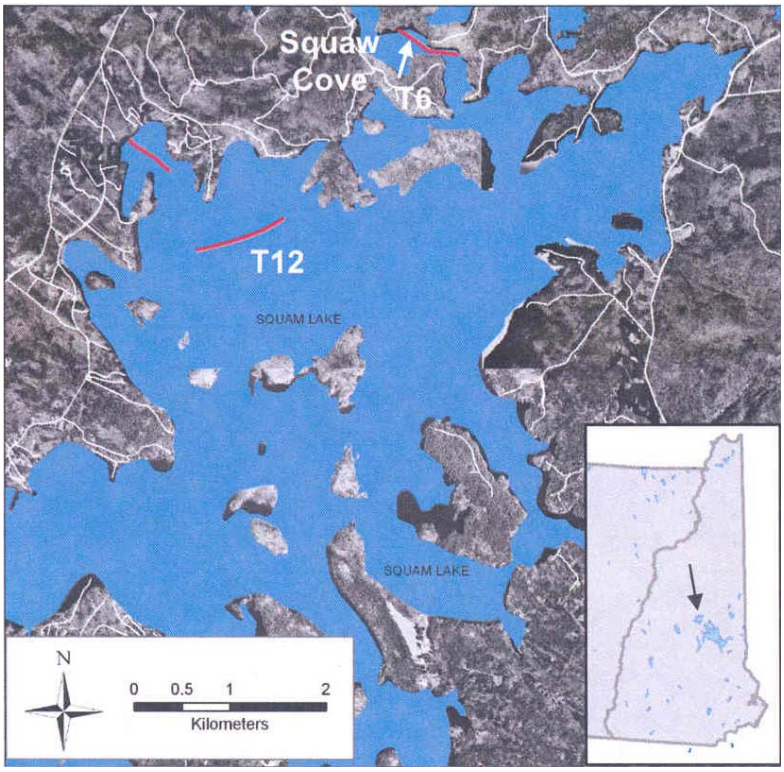

Figure 3. Squam Lake, NH area based on aerial photography, with roads superimposed. The red lines approximately locate the transects discussed here.

GPR control unit and antennas

We used a GSSI (Geophysical Survey Systems, Inc., Salem, NH) SIR3000 16-bit control unit and bistatic model 5106 antenna unit (nominally rated by the manufacturer at a pulse dominant frequency of 200 MHz) for our primary survey at JEP. This frequency decreased to 135 MHz because of antenna impedance loading by the water. The maximum rated peak power is about 8 W. The transmitter and receiver antennas are spaced 0.30 m from center to center. We also recorded profiles using different commercial antenna units operating near 270- and 60-MHz (GSSI bistatic model 5103 and monostatic model 3107 with transceiver, respectively). The former gives a peak power of about 1 W, while the latter is no more than 42 W. The former gave far improved subbottom resolution for water depths up to a few meters. The latter greatly improved water penetration but did not appear to improve penetration over the 135-MHz unit for subbottom penetration. Vertical resolution and beamwidth are discussed in the Results as they are important factors that contributed to the quality of the surveys.

We towed the antennas over the water surface in a small neoprene dinghy (**Figure 4**) at about 1 m/s with the antenna polarization orthogonally oriented to the transect direction. The absolute position of the antenna unit were recorded with differential GPS with an estimated accuracy of ±0.10 m, and which can be matched to any particular scan in our radar records. However, although the GPS and GPR recorded at constant rates, slight changes in boat speed resulted in slight, nonlinear deviations in the length scales of the reflection profiles shown later. Consequently, we interpolated an even distribution of profile distance locations between transect end points, with an estimated accuracy of no worse than about 1 m over most of the transects, and about 5 m within 10 m of the transect ends.

The radiated pulse waveform (**Figure 4**) has a polarity sequence of − + − for the successive major half cycles. This sequence is retained for a reflection or diffraction from an

interface between a relatively high ε medium over a relatively lower, such as water over sediment. The opposite sequence + − + occurs when reflected from metal or from an interface between a relatively lower ε medium over a relatively higher. This difference in polarity sequence distinguishes metal target diffractions because almost all other horizons within the bottom sediment, and diffractions from rock or sunken logs have the + − + sequence within the relatively high ε matrices of water and saturated sediment.

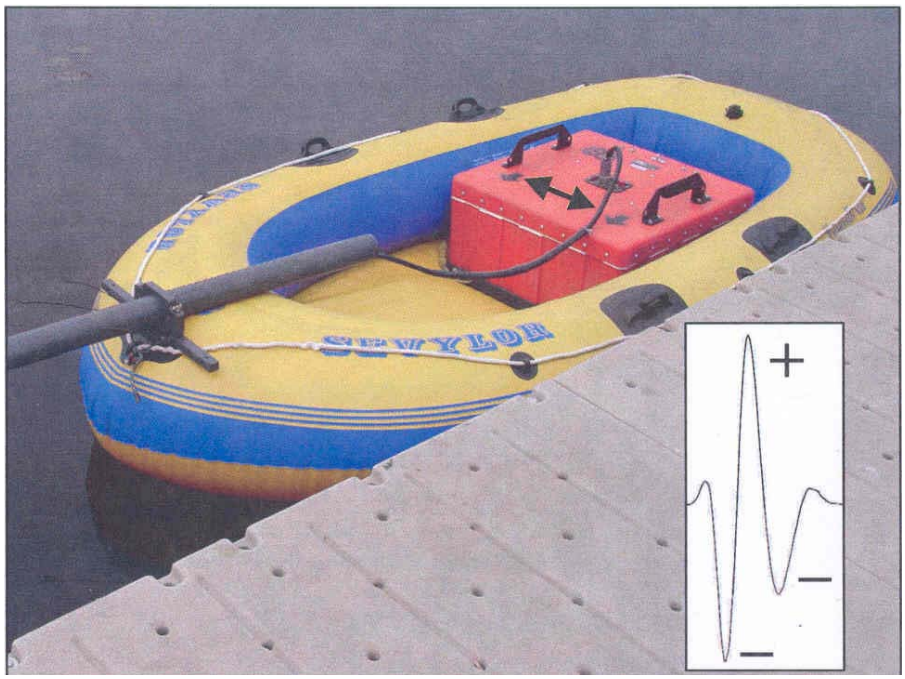

Figure 4. GSSI Model 5106 bistatic antenna unit, which produced a 135 MHz pulse when in the dinghy on the water. The inset shows the approximate shape of the transmitted pulse, which is similar for all bistatic units from the manufacturer. The polarity of each half-cycle is labeled. The dominant period is about 7.4 ns. The double ended black arrows indicate the antennas' polarization.

Processing

We recorded all data with range gain, no stacking other than the 2X stacking built into the system, and wide band IIR (infinite impulse response) filters between 25 and 300 MHz. Our post-processing used the GSSI RADAN software package. We did not correct the range gain to compensate more exactly for spherical beam spreading because we could not compensate for the defocusing that occurred upon wave passage from water into sediment along with the variable depth of the sediment surface. We applied a 50−200-MHz FIR (finite impulse response) filter to alleviate high frequency noise and low frequency modulation for the 135-MHz surveys. We did not use a background removal, horizontal filter to alleviate antenna ringing because it affected the bottom horizons, which changed by meters of depth within distances of tens of meters. Our migration was a 2-D Kirchhoff routine with constant velocity. The collapse of most hyperbolas to small localized events confirms the narrow beamwidth, as discussed later

An FIR filter is acausal, which generally results in an extra half-cycle being added to the beginning of a waveform. In some cases, this addition will reverse the waveform phase polarity sequence. Consequently, the phase structure of all waveforms displayed below were checked in the original recording to make sure that subsequent FIR processing did not significantly alter the phase.

Depth interpretation and timing accuracy

We used the echo transit time formula, $d = ct / 2\sqrt{\varepsilon_r}$, where $c = 0.3$ m ns^{-1}, to transform the round trip echo transit time, t, measured in nanoseconds (ns), into thicknesses or depths, d, in meters, and ε_r is relative dielectric constant. All time scales are plotted in this two-way transit time. We recorded a time range of 800 ns at 1024 16-bit samples/trace with the 135-MHz pulse. We estimate an error of ±0.8 ns ($\pm$ 1 sample) in picking the correct value of time zero (time of transmission), and the depth of any event. We display our profiles in a nonlinear gray scale line intensity format that gives greater emphasis to weaker signals.

Laboratory methods: TDS

Time domain spectroscopy

We measured ε^* using time domain spectroscopy (TDS). We recorded the complete time (t) domain reflection sequence, $R(t)$ (**Figure 5**), of a fast rise time step-like pulse from a dielectric sample within an open-ended (open circuit) coaxial waveguide sample holder. A reference reflection from a "short" (a metal termination), $V(t)$, was also recorded and served as the incident waveform. We picked the same time for the start of both waveforms. The ratio of these two quantities in the frequency (f) domain was then used to derive ε^*.

We processed data following methods of Cole et al. (1989) and refinements by Ishida et al. (2000), Berberian and King (2002), and Mashimo et al. (1987). In the frequency domain, the Laplace Transforms of $R(t)$ and $V(t)$ are $\mathcal{R}(\omega)$ and $\mathcal{V}(\omega)$, respectively, where $\omega = 2\pi f$ is radian frequency. The reflection coefficient, $\Gamma = \mathcal{R}(\omega)/\mathcal{V}(\omega)$, for the open-circuit sample holder is

$$\Gamma = (\rho + \exp(ikd))/(1 + \rho \exp(ikd)), \qquad (1)$$

where $\rho = (1 - \sqrt{\varepsilon^*})/(1 + \sqrt{\varepsilon^*})$, d is the length of the inner conductor, known as the "pin," $k = (\omega/c)\ \varepsilon^{*1/2}$, $c = 3 \times 10^8$ m s^{-1} is the speed of propagation in vacuo and $i = \sqrt{-1}$. Through use of trigonometric identities and derivatives of Laplace transforms Cole et al. (1989) arrived at

$$[\mathcal{V}(\omega) - \mathcal{R}(\omega)]/[\mathcal{V}(\omega) + \mathcal{R}(\omega)] - (i\omega\varepsilon^* d/c)\ (\tan z/z) = 0, \qquad (2)$$

where $z = kd$. The roots of equation (2) produce values of ε^* that satisfy this equation. Equations (1) and (2) require propagation within the coaxial waveguide and sample to be described by $\exp\{i(\omega t - k_0 z)\}$ and $\exp\{i(\omega t - kz)\}$, respectively, where $k_0 = \omega/c$ and z is distance. For this dependency ε' and ε'' are then related to ε^* as

$$\varepsilon^* = \varepsilon' - i\varepsilon''. \qquad (3)$$

The pin length d must be small to keep z away from $\pi/2$ and tan$z$ away from infinity, where equation (2) becomes unstable. For this work we used $d = 2.02$ mm for our grain fractions, 10.53 mm for our clay minerals, and both sizes plus a 0.15 mm size for calibrations with ethanol

and water. In both soil cases ε' was generally > 16. Then, at 2 GHz, $z = 4.8^{o}$ and 25.2^{o} for 2 and 10.5 mm, respectively, which are acceptable. As frequency increases or as ε' decreases z becomes larger and a smaller value of d is needed to obtain good results above 2 GHz. Cole et al. (1989) show that the d to be used in equations (1) or (2) is an effective length, though close to the actual length, which we determined by calibration with known permittivity standards.

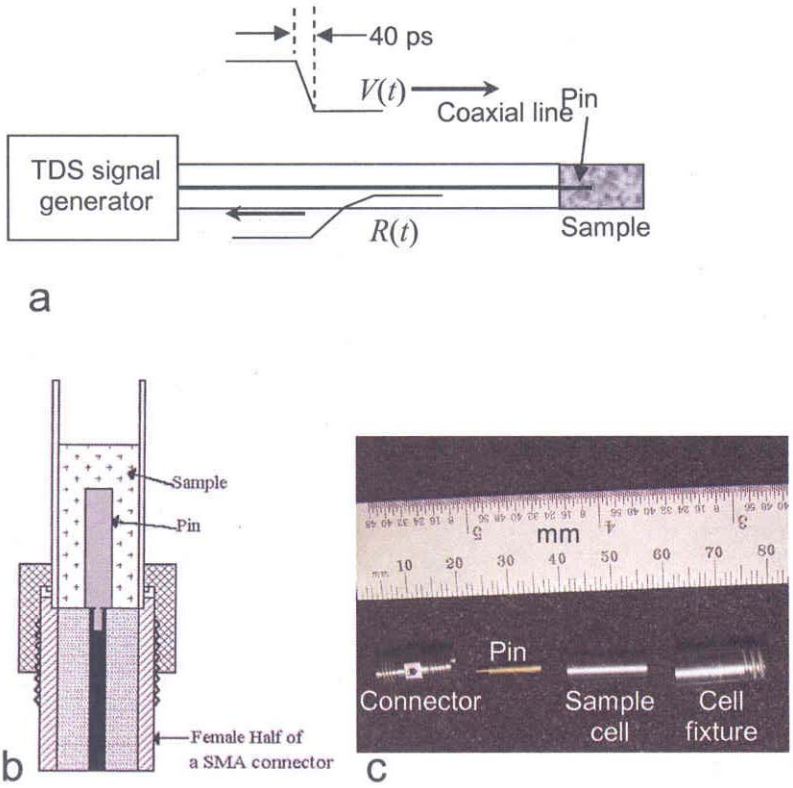

Figure 5. Schematic of TDS system setup and basic dynamics of pulse reflection (a) schematic of the sample cell (b), and photograph of sample cell and pin (c). In (a) $V(t)$ is the incident waveform with a 40-ps rise time, and $R(t)$ is the waveform reflected from the sample. The full structure of the 10.53-mm pin is shown in (c).

The inside diameter of the sample cell was 3.69 mm and the cell was 15 mm long. The 2 mm pin had a 1.58 mm outer diameter. The 2 mm length is shorter than the length of the cell (Figure 2) and provided a basic sample volume of 17.6 mm^3 for our grain fractions. The cell was filled with sample, thus providing about 13 mm of sample above the pin. The effective length of the sample cell is, essentially, the length of the pin as long as the pin is well covered by the sample; no reflections appeared from the end of the sample cell. Interchanging pins changed the contact pressure between pin and sample, and the sample density, volume and volumetric water content, all of which affected the measurements. At the expense of data quality, mainly in ε'' above about 1.5 GHz, we present 10.53 mm pin data for our clay minerals because the sample volumes resulted in volumetric water contents close to those of the grain fractions.

We used an Agilent 86100C oscilloscope equipped with a 54754A differential TDS module and a pulse rise time of 40 ps. For each of the grain fractions we performed three recordings of 4096 points at sampling rates of 0.61, 2.44, and 9.77 ps. We merged these recordings into a single set of ~ 65,000 data points of ~ 40 ns duration with an interpolated

sampling rate of 0.61 ps. The 0.61 ps sampling rate gives a Nyquist frequency of 820 GHz, but our practical bandwidth extended to 2–4 GHz; calibration runs with liquids of known parameters showed good data to about 4–6 GHz. The clay mineral recordings used sampling rates of 2.44, 9.77 and 39.06 ps which we merged into a single 160 ns data set. Our practical limit for the pure clay mineral measurements was about 1.5 GHz. We averaged 256 waveforms, which increased the signal to noise ratio and reduced variance, primarily caused by time jitter.

Post-processing of permittivity data

We computed the complex refractive index n^* from the measured values of ε^* such that $n^* = \sqrt{\varepsilon^*}$. We computed phase velocity $v_{ph} = c/\text{Real}(n^*)$. We computed the one-way attenuation rate β (dB m^{-1}) from the imaginary part of the wave number in the exponential propagation term exp ($-ikz$), where z = 1 m. The expression is

$$\beta = 8.686(\omega/c)\left(\varepsilon'^2 + \varepsilon''^2\right)^{1/4} \sin\left[\frac{\tan^{-1}(\varepsilon''/\varepsilon')}{2}\right]. \quad (4)$$

In field situations, β must be added to the loss of signal intensity caused by geometric spreading of the radar beam in order to find the total signal attenuation, and this total must be doubled for round-trip radar propagation. Consequently β values of 10–15 dB m^{-1} can extinguish a reflection within a few meters depth.

The imaginary part ε'' includes any relaxation or conduction process. The contribution of DC conductivity, σ, to ε'' is expressed through the term $-i\sigma/\omega\varepsilon_0$, where σ is conductivity in S m^{-1} and $\varepsilon_0 = 8.854 \times 10^{-12}$ F m^{-1} is the permittivity of free space. The DC conductivity dominates ε'' when the low-frequency asymptotic behavior of ε'' becomes logarithmically linearly dependent on frequency. In that case ε'' may then be used to determine σ. If the asymptotic logarithmic dependence is non-linear, then the low-frequency behavior is termed anomalous, for which (Kaviratna et al. (1996) describe several possible causes. Theoretically, in the linear case one may subtract the σ term from the measured ε'' to isolate relaxations within the permittivity spectra (Ishida et al, 2000). Although we see linear trends in ε'' as frequency decreases, we do not perform this subtraction exercise because relaxations are known to exist near the low end of and below our bandwidth (Ishida et al., 2000; Rotenberg et al., 2005).

Grain size fractions

We obtained our size fractions from the whole soil (< 200 μm) by chemical pretreatment to remove soluble salts, organic matter, and free iron oxides (**Figure 6**), and then by adding sodium bicarbonate to facilitate separation by gravitational settling. The whole soil sample for which we measured ε^* was not treated for oxide removal. We followed procedures in Kunze and Dixon (1986) and base our clay and silt terminology on the USDA classification of particle size (clay is < 2 μm; silt is 2–67 μm). Our fractions are < 2 μm, 2–10 μm, 10–20 μm and >20 μm. The fractions were then equilibrated with deionized water to yield an expected volumetric water content θ_W of 0.30. We measured a specific surface area of 54.7 m^2 gm^{-1} for the whole soil using ethylene glycol monoethyl ether retention.

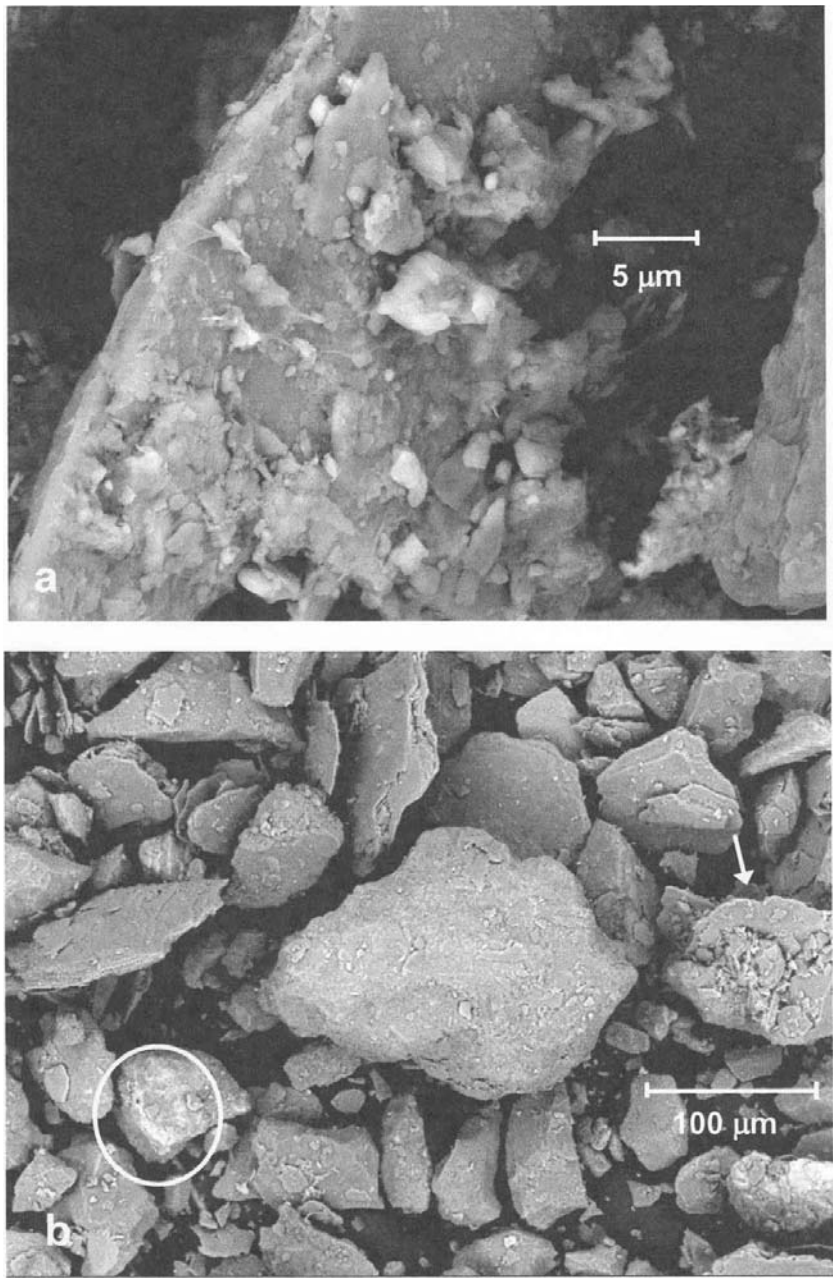

Figure 6. SEM images of Fairbanks silt at two resolutions. In (a), many of the smaller particles adhere to a larger particle of quartz or feldspar. In (b) the rough surfaces and edges are apparent. The platey particles are mica, the large quartz sand particle at center in (b) is near the upper size limit of 200 μm for this soil, and the arrow indicates a sand-size particle of mica to which silt- and clay-size particles adhere. Most ferric oxides have been removed, as indicated by the almost total lack of luster (seen in oval) on the particles.

The final values of θ_w varied between samples because they depended on sample density and porosity (θ_a; **Table 1**). For example, the dry density varies by 22% over the grain size fractions and is significantly higher for the whole soil. This is logical because the whole soil experiences filling within the interstices at successively smaller pore sizes and so shows the

lowest porosity. Subsamples (splits) obtained within each sample varied in θ_w. For example, our 2–10 μm calibration has a higher θ_w than does the 2–10 μm sample discussed in the Results. Therefore, we were fortunate that our values of θ_w were close among the fractions, and that the 10.53 mm pin could provide comparable values of θ_w for the clay minerals.

Grain size	Dd (gm^{-3})	Por.	θ_w	θ_a
Whole	1.66	0.39	0.29	0.10
> 20 μm (84.4%)*	1.43	0.48	0.27	0.21
10–20 μm (7.5%)	1.37	0.50	0.30	0.20
2–10 μm (5.7%)	1.48	0.46	0.33	0.13
< 2 μm (2.4%)	1.21	0.56	0.34	0.22

* > 63 μm (31.3%)

Table 1. Parameters of the Fairbanks silt fractions. The percentages of composition in column one are based on weight and were determined from the sample prepared for XRD. Dry density (Dd) and porosity (Por.) are based on a solid mineral density of 2.65 g cm^{-3}. θ_w is total volumetric water content and θ_a is volumetric air content.

X-Ray Diffraction

We performed our own X-Ray Diffraction (XRD) and also contracted with a private company (Technology of materials –TM-, Wildomar, CA) to determine mineralogy and weight percentages. We fractionated splits by first using a sodium acetate and acetic acid buffer (pH=5) solution to remove soluble salts and carbonates, but we did not remove iron oxides (none appeared in our spectra) because they could have been an important factor. We dispersed with ultrasound in a 0.005-M sodium metaphosphate solution. We then separated fractions of < 2 μm, 2–10 μm, 10–20 μm, 20–63 μm, and >63 μm by gravity separation, at weight percentages given in **Table 1**, and obtained XRD patterns for each fraction. We combined the 20–63 μm and >63 μm using a weighted average where necessary to make comparisons with the ε^* data. TM used similar procedures, did not remove iron oxides, and did not report the presence of any iron oxides.

We used a Siemens D-5000 diffractometer run at 40 kilovolt (kV) and 40 milliamperes (mA). TM used a Phillips diffractometer at 30 kV and 20 mA. Both instruments used a Cu K alpha radiation source, a scintillation detector, and scans at two theta (2 Θ) from 2 to 50° (TM) and to 60° (ours). TM additionally scanned oriented and glycolated clay mounts from 2 to 30° 2 Θ. We used Soller slits and prepared our samples and standards in a shatterbox to homogenize particle sizes. We mounted all samples in identical fashion to minimize quantitative errors associated with non-random orientation. Both labs identified minerals using the JCPDS database. We assessed mineral weight percentages from the ratios of integrated areas for strongly diffracting lines, and we calibrated against integrated areas of pure minerals (zinc oxide and illite) at known fraction sizes collected under identical conditions. The empirical nature of our calibration provides a means of accounting for orientation effects, which can strongly impact measured sample intensities. TM made semi-quantitative estimates of mineral components from peak intensities compared to quartz and kaolinite reference standards. Both laboratories estimate percentage weight figures are accurate to $\pm$ 8–10%.

The laboratories had differences in the results. Aside from differences in mineral weight percentages, discussed later, we estimated the weight fraction of amorphous material in our 10–20, 2–10 and < 2 μm fractions at 9%, 29%, and 49%, respectively, with 3.4% for the whole soil.

The independent laboratory estimated that of the whole soil at < 15% by weight. We did not differentiate illite from vermiculite, but doubt its presence; TM found no vermiculite. TM did not differentiate illite from mica, which we did. Later, in our modeling, we used our own determinations of mineral weight percentages because our calibration procedure used standards we established.

ACCOMPLISHMENTS: JEP SURVEY

This section gives the results, analysis and interpretations we have obtained during the three years of this project. The descriptions of these phases are drawn from the three journal articles we have either published (Arcone et al., 2006), accepted for publication (Arcone et al., in press) and in preparation (Arcone et al., in prep.). The preparation of these latter two has been the primary work accomplished in FY2007. As stated above, the purpose of this project is to understand how GPR technology works to detect subbottom UXO, and how the results are to be interpreted. The term "works" includes the effect of water on antenna patterns, the effect of water conductivity and sediment complex permittivity on propagation, the effects sedimentary stratigraphy on reflections and the effects of UXOs on scattering. Interpretation is the meaning of the results; i.e., how UXO are to be interpreted from the GPR profiles.

Overview

Buried unexploded ordnance (UXO) is a common target for detection with ground-penetrating radar (GPR). Although the higher resolution GPR signals centered from 300–1000 MHz typically provide a meter or more of ground penetration, identification of UXO type is difficult from only the typical responses of a few diffractions. Consequently, outside of circumstantial evidence and historical reports, identifying information must come from attributes within individual waveforms and the disposition of refection profiles horizons. Waveform attributes may include resonances induced on the target structure (Chen and Peters, 1997) or by target interaction with the geologic matrix (Arcone et al., 2006a). Profile attributes may include disruption of existing strata, or stratigraphic genesis subsequent to the UXO emplacement. In this case history we use the well known site history to aid our discussion of waveform and profile attributes that were and are still being generated by single to dense concentrations of highly probable fused practice bombs lying on or embedded within lacustrine sedimentation.

JEP had been used for practice bombing from 1942–1958, which suggested that most targets would be buried. Terrestrial UXO surrounding the pond was last discovered in October, 2006, so we expected UXO to be distributed about the pond itself. Although subbottom acoustic profiling had not been tried on JEP, our previous success with GPR in comparison with acoustic profiling on nearby lakes (Delaney et al., 1992; Sellmann et al., 1992) suggested that GPR would successfully detect subbottom objects at least 2–3 m beneath 10 m of water. In addition, the low conductivity, σ, of New England lake water, the dependence of permittivity upon clay mineralogy (Arcone et al., 2008), the vertical resolution offered by the shortened GPR wavelengths in water, and the expected well-developed lacustrine stratification, led us to the hypotheses stated earlier in regard to successful detection of subbottom objects such as 100–1000 pound bombs, even at > 10 m depth. GPR profiling of lake and river subbottom stratigraphy has been successful elsewhere (Moorman, 1998; Fuchs et al., 2004; Porsani et al., 2004) and we suspect that this success was also facilitated by the subbottom mineralogy.

Although the immediate objective of the JEP survey was to locate likely UXO for the Air Force, our more general purpose rapidly expanded to understand why the survey of both targets and geology was successful. Consequently, based on the above hypotheses, our indirect

objectives were to measure water conductivity, sediment mineralogy, signal penetration, migration velocities, and phase signatures, and to detect artificial strata disruption within reflection profiles recorded at JEP and two other lakes. The main JEP basin is only about 500 m in dimension. Given this small and ready-made site but only a line profile capability, we recorded 38 profiles in spring, 2006 in hopes of encountering many examples of stratigraphy, UXO and false targets on, and embedded within strata. After trials, we stayed with the 135-MHz dominant frequency antenna unit in expectation of consistently gaining 5–8 m of subbottom penetration with an in situ dominant wavelength in water of only 25 cm. We kept our antenna polarization perpendicular to transects direction to maintain the narrower beamwidth across transect. We compared our results with 1) a side scan sonar survey of bottom surface objects in JEP; 2) profiles recorded over a nearby pristine lake; and 3) profiles of controlled targets in a shallow frozen lake where our positional stability allowed us to test the consistency of target phase response. The pristine lake had far greater depths, similar conductivity, a similar source of sedimentation (glacial till), allowed bottom coring and some exquisite stratigraphy that made the cause of strata folding clear. Underwater photography and a dragged magnet supplied highly inadequate direct ground truth.

The primary munitions were 100–1000 pound "General Purpose" fragmentation bombs, and 350 pound depth charges, all of which have thin casings that explode into tiny fragments. According to our control studies profiles of small munitions such as grenade-size fragments or smaller should be undetectable at greater than 2 m depth. Consequently, we believe that the recorded diffractions were from complete bombs and not from large fragments. We have no knowledge of any other type of metal object on the bottom other than the original floating targets, which the side scan sonar survey revealed.

The JEP and Squam Lake profiles (**Figure 7**) contain most reflection and diffraction events seen in all other profiles. Event 1 is the reflection horizon for the bottom surface of the deeper basins and along the rising shores. At shallow depths, such as beyond 175 m in **Figure 7a**, event 1 is overlain by other, less reflective deposits. The $1 - + -$ polarity sequence of events 1 indicates that the subbottom sediments have a lower ε than water. We use $\varepsilon = 36$ for these sediments because we measured this value on land for a saturated sandy silt (Arcone and Delaney, 2003). If the value ranges from 30 and 44, then the depth error is no more than 11%.

Events 2 and 3 in **Figure 7a** are sedimentary foreset and bottomset beds, respectively. They occur between 125 and 150 m, where the horizons show both polarity sequences, and beyond about 220 m on the northeast side where they show more fully developed foreset and bottomset beds. Topset beds do not appear, most likely because they were eroded by the strong, event 5, discussed below.

Events 4 in both figures are bedrock horizons, which are composed of $- + -$ diffractions. In response to the rough surface, bedrock surface horizons are usually characterized by closely spaced diffractions, whether beneath sediment (Arcone et al., 1998) or ice (Arcone, 2002; Welch and Jacobel, 2005).

Events 5 are reflection horizons from subbottom sedimentary interfaces. Their consistent $- + -$ polarity suggests that they are thin layers with an ε' that is lower than that of the silt. A relatively lower ε' indicates a higher coarse silt to fine sand content, which very likely results in relatively less clay mineral content (at a similar volumetric water content; Arcone et al, (2008). The folds within these horizons are not deformational but are caused by draping over bedrock (**Figure 7b**). The most continuous of these horizons is strong enough to provide a multiple from 160 to 225 m in **Figure 7a**. They appear to be from storm events because the most extensive one

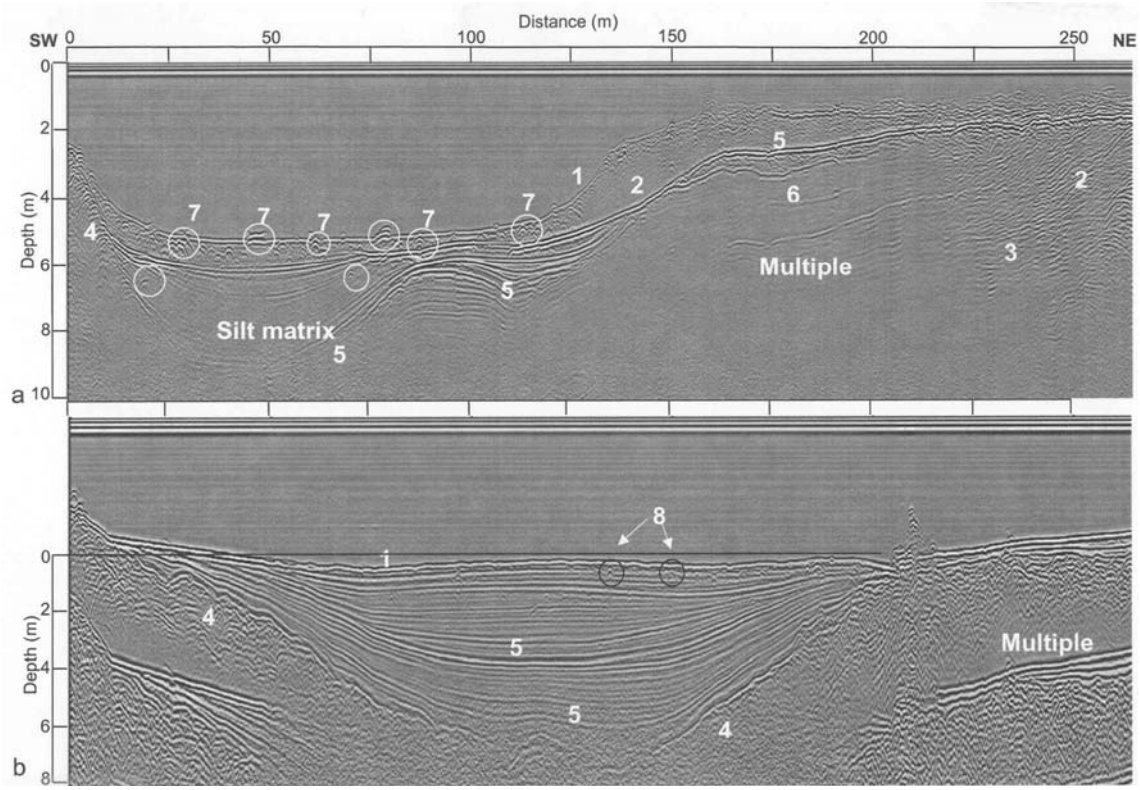

Figure 7. Profiles from T14 on JEP (a) and from Squaw Cove (b). The major horizons and events are: Bottom surface (1); foreset beds (2); bottomset beds (3); bedrock (4); basin sediments of mainly − + − horizons (5); a rare + − + horizon (6); + − + diffractions and short reflections (7; white circles); and − + − diffractions (8; black circles). Depth is calibrated for water in (a) and for saturated silt in (b).

(event 5) defines an erosional surface of the foreset beds at the far northeast side and in the deeper basin, where it further defines erosion of older sandy layers between 12 and 140 m distance. Many of these older layers fade as they penetrate into the deeper basin. Coring in Squaw Cove confirmed the presence of a more coarse-grain deposit. The only event with the opposite polarity, event 6 (**Figure 7a**), likely has more clay mineral content than the matrix.

Events 7 (**Figure 7a**; some are circled) have + − + polarity and so are metallic. They are therefore, likely UXO because there is no common material with $\varepsilon' > 81$. They appear as short reflections and diffractions, the density of which will be seen later to increase within the deeper basin. **Figure 8** shows details of these events. In **Figure 8a** the + − + events are near the sedimentary surface and the waveform at 46 m distance is from a target about 2 m long. In **Figure 8b** we have removed some of the stratigraphy with a horizontal filter to reveal all the − + − diffractions. The depth scale is for $\varepsilon' = 36$. We show a sample waveform from the diffraction centered near 180 m. Many event 7 diffractions occur near the surface and many are buried.

Events 8 in **Figure 7b** are from either boulders or logs because they have a − + − polarity sequence. Boulders are geologically unlikely in the basin whereas logs are common in the side scan sonar image shown later in **Figure 18**. Bundles of logs were often tied to make bombing targets. They especially appear as short reflections of 2–6 m apparent extent (**Figure 16)** and are discussed later in association with the side scan sonar results.

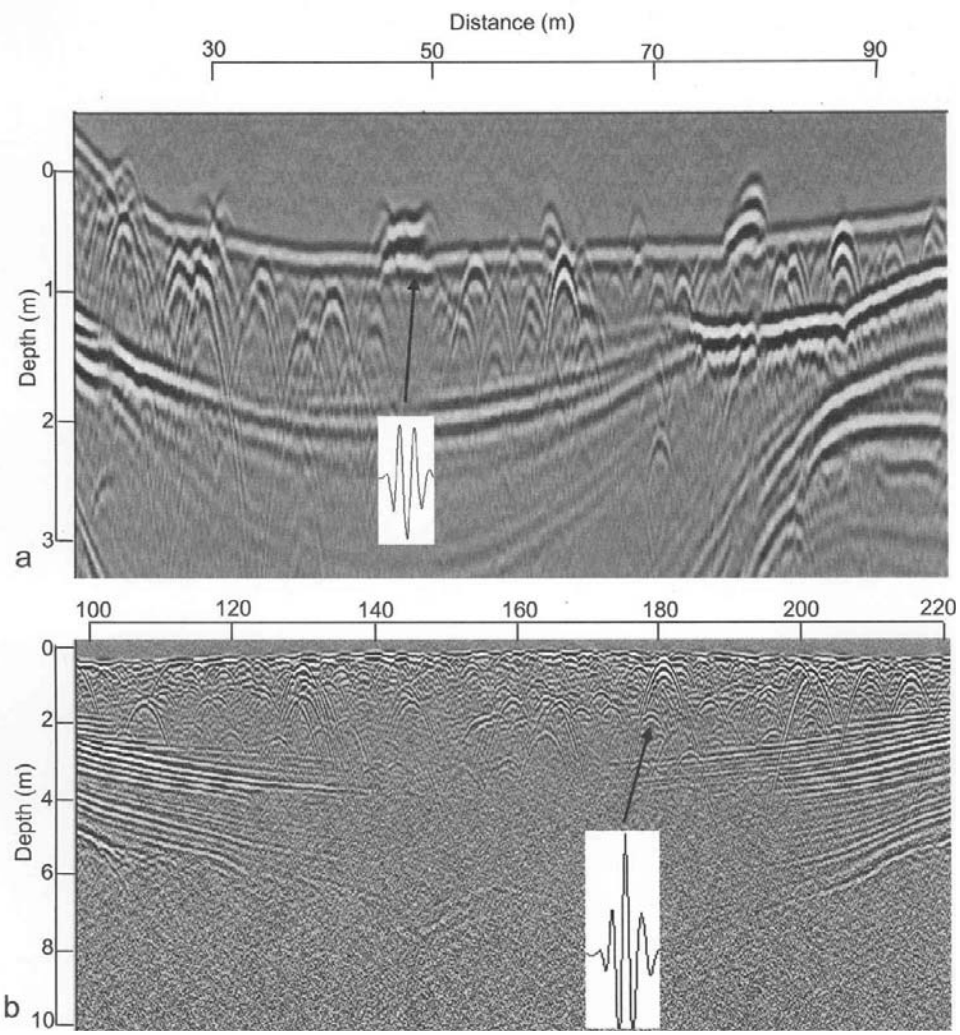

Figure 8. Profile segments from transect T14 (a) and from Squaw Cove (b) along with sample waveforms from the diffractions. The depth scale in (a) is for water while in (b) it is for $\varepsilon = 36$ and the reference level is the bottom surface reflection, the continuity of which has been severely affected by the horizontal filter. Note the different distance scales.

Phase

The most important aspect of interpretation for possible UXO is the differentiation between metal and non-metal targets. As discussed above, the phase polarity sequences of the successive half cycles of the waveforms from metal targets within a high permittivity matrix of saturated sediments are mainly opposite of those of embedded layers, rocks or boulders in this water environment. This is an easy task for short to extended reflection horizons, but for isolated diffractions it is not all that clear because the aspect of the target relative to the incident polarization direction might conceivably cause change in waveform.

We performed controlled experiments to check that the phase polarity sequence remained consistent for obliquely incident waves. Our experiments were carried out on a small, shallow and completely frozen lake in interior Alaska (Arcone et al., 2006). The ice surface allowed us to position our antennas exactly with respect to the target axes, and the metal nature of the targets precluded any importance to the value of the overburden ε, regardless of whether it was water or ice. Our target was a 250-pound all purpose fragmentation bomb and we used the Model 5103

antenna unit that radiated a 400-MHz (actual dominant frequency) pulse. All profiles showed a consistent + − + polarity sequence regardless of whether the antennas were polarized parallel, perpendicular or obliquely with respect to the target axes. **Figure 9** shows the results for oblique incidence, for which the profiles were recorded along a transect oriented at 45° to the target axis. As shown by the waveforms, the diffractions are consistently of the same polarity sequence. Consequently, we assume that any metal target will provide the same + − + sequence regardless of orientation with respect to incident polarization. Similarly, the consistency of the − + − sequence from trees or logs suggests that these objects could never provide a + − + sequence.

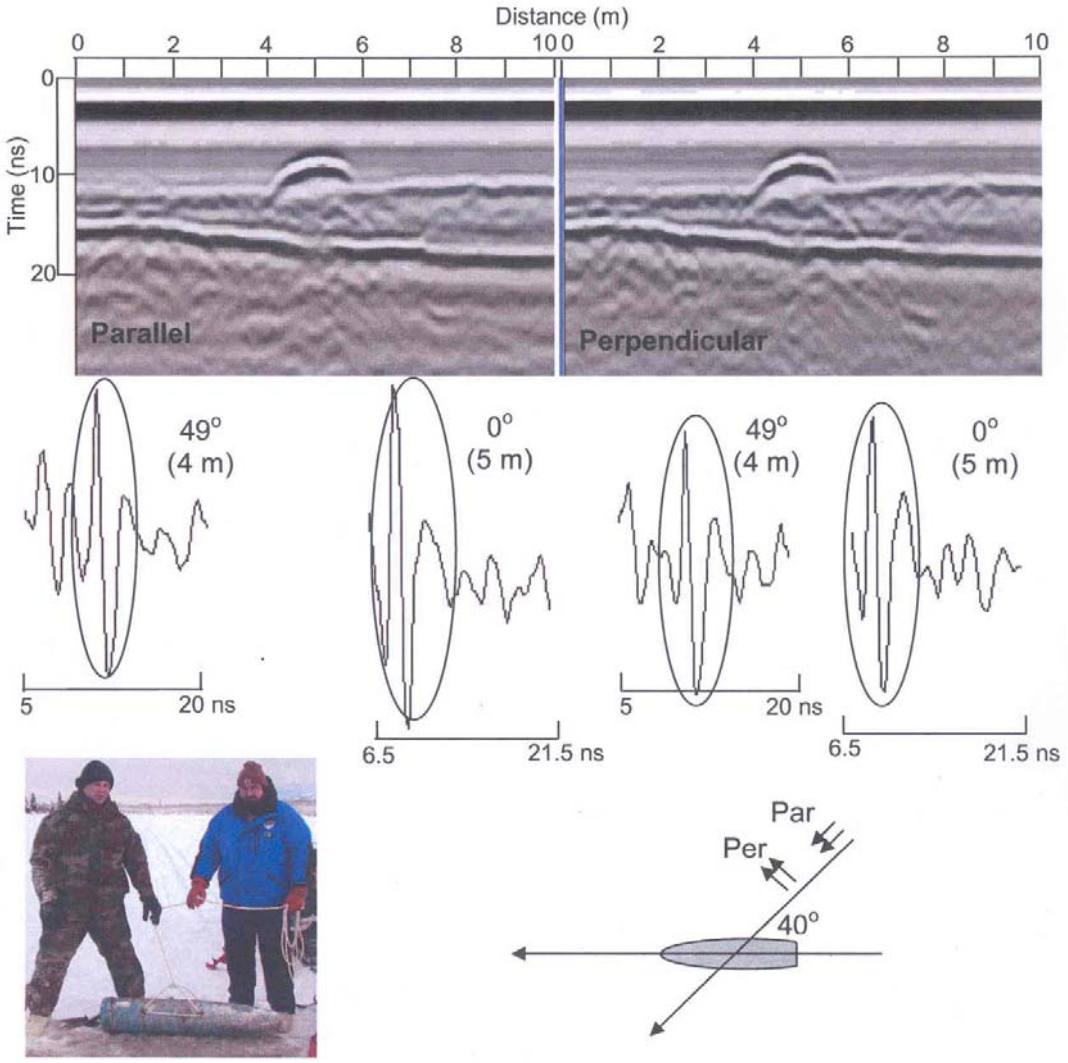

Figure 9. Parallel and perpendicular 400 MHz polarized profiles (top left and right, respectively) recorded at a 40° transect angle across a 1.3 m, 250 pound bomb emplaced under ice, and waveforms extracted from the profile above the bomb and at 49° angle off the bomb axis. The amplitudes are exaggerated for display. The waveforms are consistent regardless of polarization or angle of transect. The ε' of the overburden, whether 3.2 (ice) or 81 (water) is irrelevant because of the extremely high conductivity of the target. Photograph shows the bomb before insertion.

Water conductivity

The water penetration is made possible by the low water conductivity. **Figure 10** compares the theoretical one-way attenuation rates for the JEP and Squam Lake conductivities of $\sigma = 0.004$ S m^{-1} with that of typical freshwater in the U.S., $\sigma = 0.05$ S m^{-1}. There is more than an 8 dB m^{-1} difference per meter near 135 MHz based on conductivity alone. Surprisingly, the Debye relaxation centered near 20 GHz makes a relatively significant contribution for the lower conductivity case and boosts the total two-way value to 1.5 dB m^{-1}. Consequently, the round trip loss by 8.5 m depth is 13 dB. At the 30 m reached at 60 MHz in Squam Lake, the round trip loss was only 1 dB.

Regardless of depth, the bottom surface reflection maintained a center frequency between about 130−140 MHz. Consequently, dispersion caused by water propagation was not a factor. This is definitely not the case for more conductive water like on the Mississippi River, where pulse center frequencies can drop from about 300 to 200 MHz after slightly less than 4 meters round trip propagation (Arcone et al., 2006b).

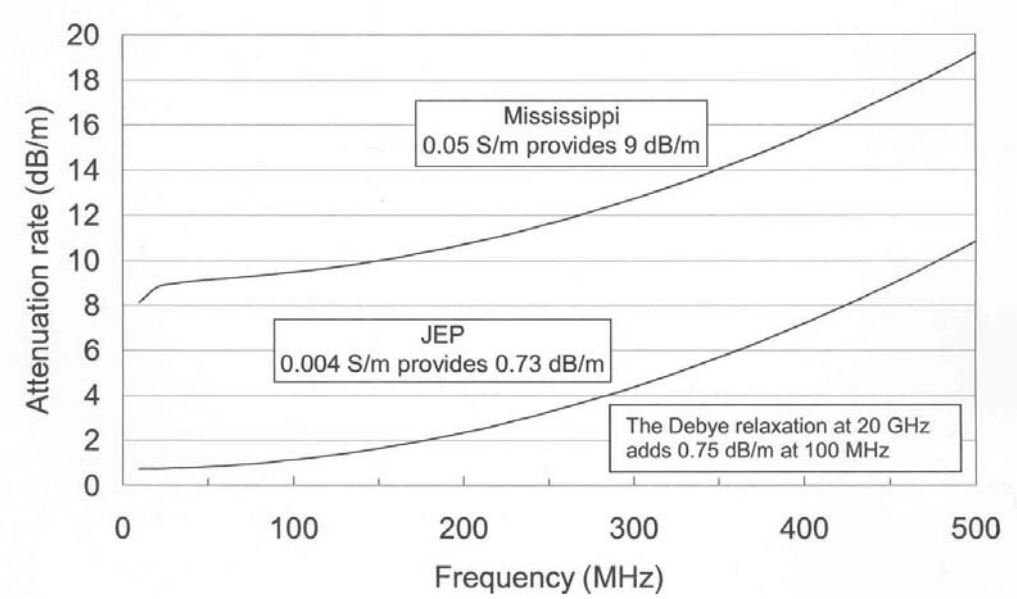

Figure 10. Attenuation rates as a function of frequency in water for two conductivities. The Debye relaxation is included in these calculations.

Narrow beamwidth and migration

The hyperbolic shape of the diffractions in all profiles conform very closely to that generated by model hyperbolas using $\varepsilon' = 81$. This conformity is caused by the relatively narrow beamwidth in the antenna E-plane, which crossed the profile direction and alleviated out-of-plane reflections and diffractions. The virtual two-way antenna directivities in the E- and H-planes for any unit are shown in **Figure 11**. We computed them for finite size antennas on water of zero conductivity with zero offset (Arcone, 1995). The high ε of the water considerably narrows the far field 3-dB beamwidths from what they would be in earth media of much lower ε and provides a half 3-dB width in the E-plane (perpendicular to the transect direction) of only 20^0. However, at 8.5 m depth the two-way E-plane half beamwidth is down 2 dB at a ray angle of 15^0 and the extra 0.3 m traveled by a ray at this angle experiences an additional 1 dB of two-way attenuation

caused by σ= 0.004 S/m and a relaxation frequency of 19 GHz. Consequently, the 3-dB half beamwidth is actually 15^0, which avoids out-of plane events and makes 2-D migration work well.

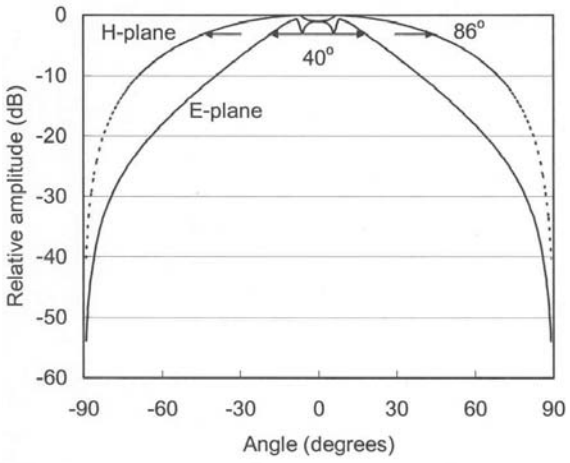

Figure 11. Two-way antenna directivity patterns for a finite size dipole in water for σ= 0.0. The patterns are virtually those of the bistatic antenna systems we used wherein the antenna separation was only 0.3 m.

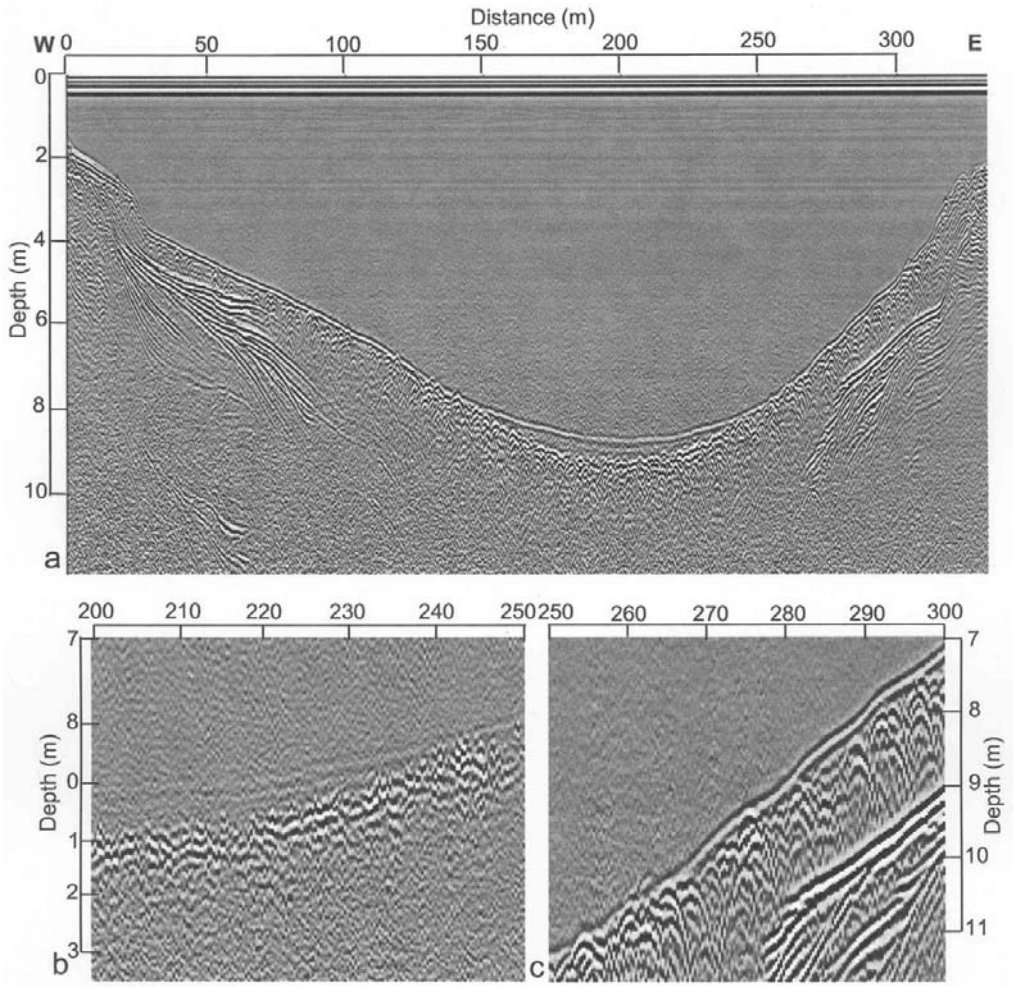

Figure 12. Unmigrated profile segment of deep basin below T18 (a), detail of migrated segment showing − + − section (oval) (b); and detail of draping over targets (c). Depth scale is for water (a); water and sediment (b) and sediment (c).

In addition, to improved target location, proper single layer 2-D migration occurs when targets are on or near the bottom, which confirms the confinement of the beam directivity within the H-plane. Targets in the deeper basin are likely to have settled slowly upon the bottom and undergone shallow burial. We show a profile segment below T18 (**Figure 12a**) its migration (**Figure 12b**) using the water velocity ($\varepsilon' = 81$) and a detail of one of the slopes (**Figure 12c**). The numerous targets in **Figure 12b** form an almost continuous horizon and it is difficult to establish their individual polarity sequences. The migration however, shows one segment that migrates to a layer with a − + − structure and so are not metallic objects (migrations of individual targets preserve the polarity sequence). There is about 0.8 m maximum sediment buildup in the deepest part, and a second layer has formed here. There is also no appearance of any strata beneath this central section. The targets would have to be spaced closer than one half in situ wavelength in the direction of the transect (perpendicular to the polarization direction) in order for these strata to be masked. For $\varepsilon = 36$, the spacing is then < 0.2 m at 135 MHz. A profile recorded at 60 MHz across this part of the lake also failed to reveal deeper stratification.

The enlarged segment in **Figure 12c** shows sediment with a wavy surface because it is draped over targets. The slope of this section is only 3.8°. The ~ 10 m periodicity in the draping is too large to indicate the dimension of single targets. However, the 0.37 m pulse length (in water) of the sediment reflection horizon appears long enough to have covered most targets within this section.

Subbottom penetration and resolution

Visualization of signal penetration was made possible by the deltaic deposits and bedrock. In each example the attenuation rate must be a few dB m^{-1} or less to allow such round trip propagation. The deepest signals appear to return from about 8 m depth for which a round trip rate of only 5 dB m^{-1} would result in a total attenuation loss of 80 dB. When added to to geometric spreading losses, water attenuation losses, layer transmission and reflection losses and system losses, the total loss would more than likely reach the theoretical 110–120 dB estimated performance figure of the radar.

The bedrock type was mapped by Billings (1955) and later by Lyons et al. (1998) as quartz-mica schist. This schist constitutes some of the hardest rock in New Hampshire but there is no way of knowing its competence beneath the lake, nor are there any reference measurements of attenuation rates. We assume that this rock type exhibits extremely low conductivity and attenuation rates of less than 1 dB m^{-1} because of the predominance of nonconductive minerals such as quartz and mica.

Bedrock occurs most frequently near the southwest shore, beneath the base of a steep hill. **Figure 13a** shows a segment of transect T5 with bedrock rising to this hill. The close diffractions appear to form a continuous horizon, which occurs in the migrated section (**Figure 13b**). All waveforms of the diffractions and the sedimentary horizons have the − + − polarity sequence. For the migrated diffractions in **Figure 13**, 10–12 all retain the phase polarity sequence of their apices. This reflects the fact that the entire diffraction exhibited the same sequence. However, the orientation of the target relative to the incident polarization is not known.

Figure 14 gives two examples of signal penetration into bedrock and within which several − + − diffractions appear. **Figure 14a** shows bedrock protruding along T19. The surface appears smooth and the diffractions from it are not obvious because their asymptotes are not extended. The narrow beamwidth and the conformity of the hyperbola shapes to models generated for $\varepsilon = 81$ show that the events are from within the rock and are not out-of-plane diffractions. The bedrock interface horizon fades beneath the small sedimentary basin, but then emerges to rise toward the shoreline. **Figure 14b**, from along T8, reveals internal stratification that is likely sheet fractures, which is common throughout New Hampshire (Jahns, 1943; Arcone, 1984) and most other parts of the world (Holzhausen, 1989; Glasser, 1997). The phase polarity of

these features varies, indicating fracture fill to be either air (− + −), quartz-rich mineral (− + −), carbonate-rich mineral (+ − +) or water (+ − +).

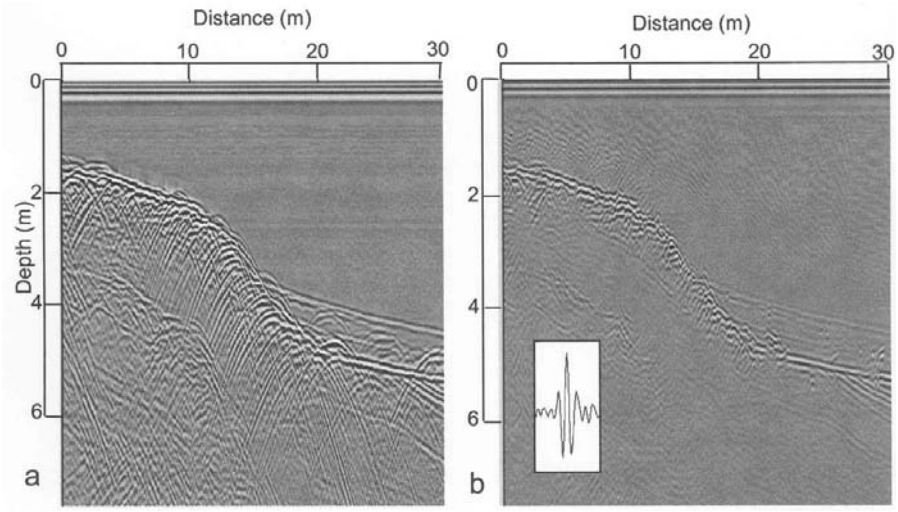

Figure 13. Profile segment from near SW shoreline of transect T5 before (a) and after migration (b). The 30 ns segment of inset waveform (scan 59, 7 m distance) shows the − + − polarity sequence of the migrated surface, although this waveform varies. Migration velocity based on $\varepsilon = 81$. Other diffractions and horizons are also − + −.

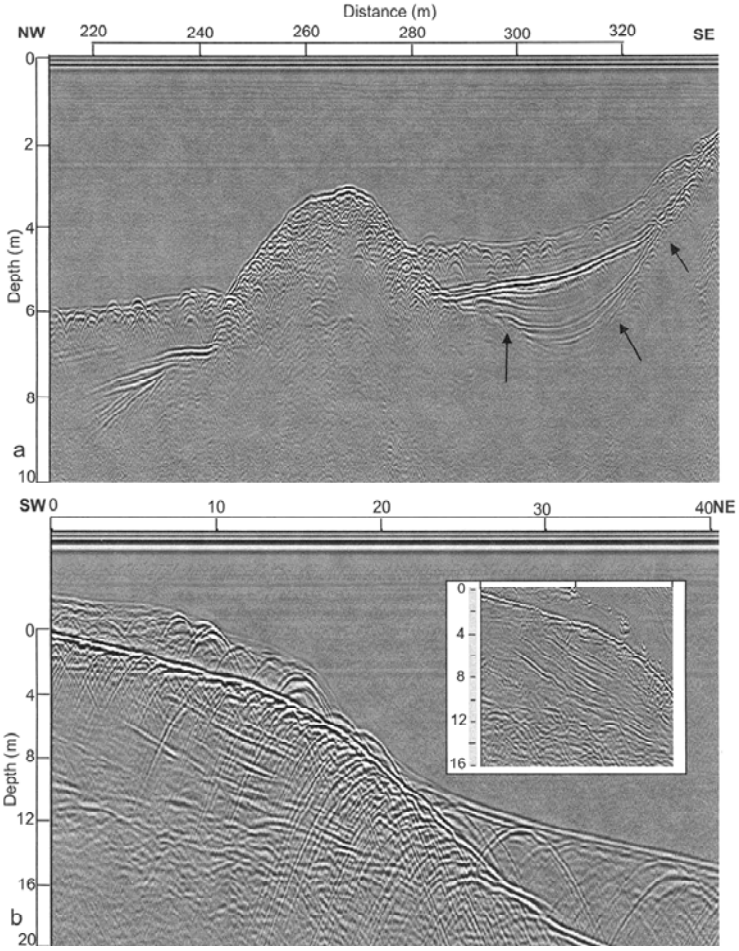

Figure 14. An example of a bedrock protrusion along T19 that shows internal diffractions (a), and shoreline bedrock along T8 exhibiting internal interfaces (b). The bedrock surface in (a) fades beneath the sedimentary basin, but then can be followed to the shoreline (arrows).

In either **Figure 13a or 14a** there are no + − + diffractions along the bedrock surface, but there are + − + diffractions on either side of the protrusion in **Figure 13a** and within the sediments above bedrock in **Figure 14b**. Consequently, it appears that any UXO that fell on these bare rock surfaces then moved downslope. Both profiles of **Figure 13** exhibit numerous diffractions within and on the sedimentary strata to the sides of, and above the rock (**Figure 13b**). Most are so close or superimposed that their polarity sequence cannot be determined. A few are strong and isolated enough to discern their polarity (inset, **Figure 13b**).

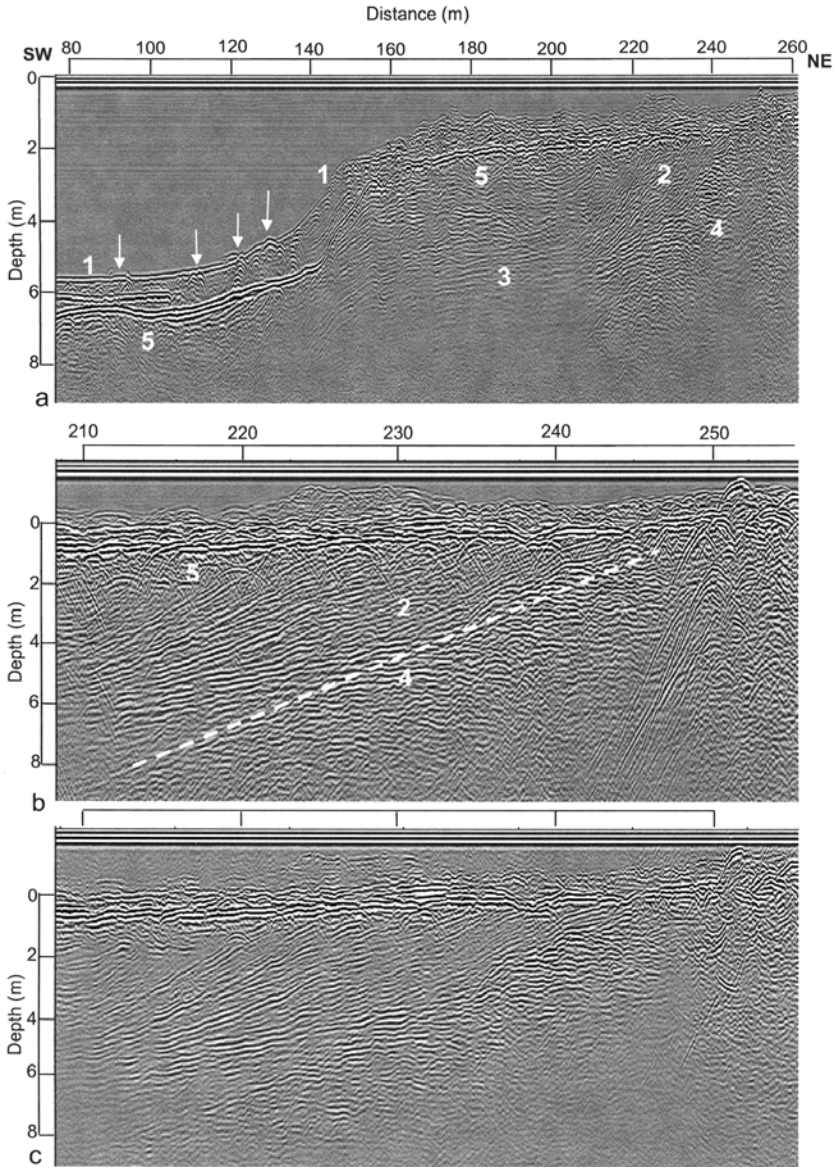

Figure 15. Deltaic deposits under the shallow north end of T13 (a), detail of the last 47 m (b), and its time migration (c). The labeled events are sediment surface (1); foreset beds (2), bottomset beds (3), bedrock (4), and sand layer (5). Arrows indicate − + − diffractions. A second set of foreset beds occurs from 140–160 m distance in (a). The dashed line in (b) indicates the diffraction horizon that defines bedrock. Depth scale in (a) is for water, for $\varepsilon = 36$ in (b) and (c) for which it is approximately referenced to horizon (5).

The deltaic deposits occur on the northeast side and were profiled almost perpendicular to the shore along transects T13–17. A first example was seen along T14 (**Figure 7a**), where there are two sets of foreset beds. The damming of the lake suggests that they were formed when the lake was about 2 m lower. **Figure 15a** shows a segment of profile T13, which is stacked to better image the transition of the foreset (events 2) into bottomset (events 3) beds. The bedrock, horizon 4, appears to define the depositional surface. In the detail (**Figure 15b**), the depth scale is calibrated for muck $\varepsilon = 36$ and the deepest bedrock signal is at approximately 9 m within the sediment. The migration (**Figure 15c**) improves the image of these beds because it has collapsed the diffractions just beneath event 5. Event 5 appears to define the erosional surface of the foreset beds, having removed the topset beds.

We believe that the penetration is caused by a lack of almost any phyllosilicate clay minerals within the sediments, and this is discussed extensively below. The most severe of these is smectite, the most common of which is the swelling clay known as montmorillonite. Relaxations related to solvated ions, particularly sodium, within the water galleries are centered between 1 MHz and 1 GHz and therefore overlap the GPR bandwidth.

Strata distortion by UXO?

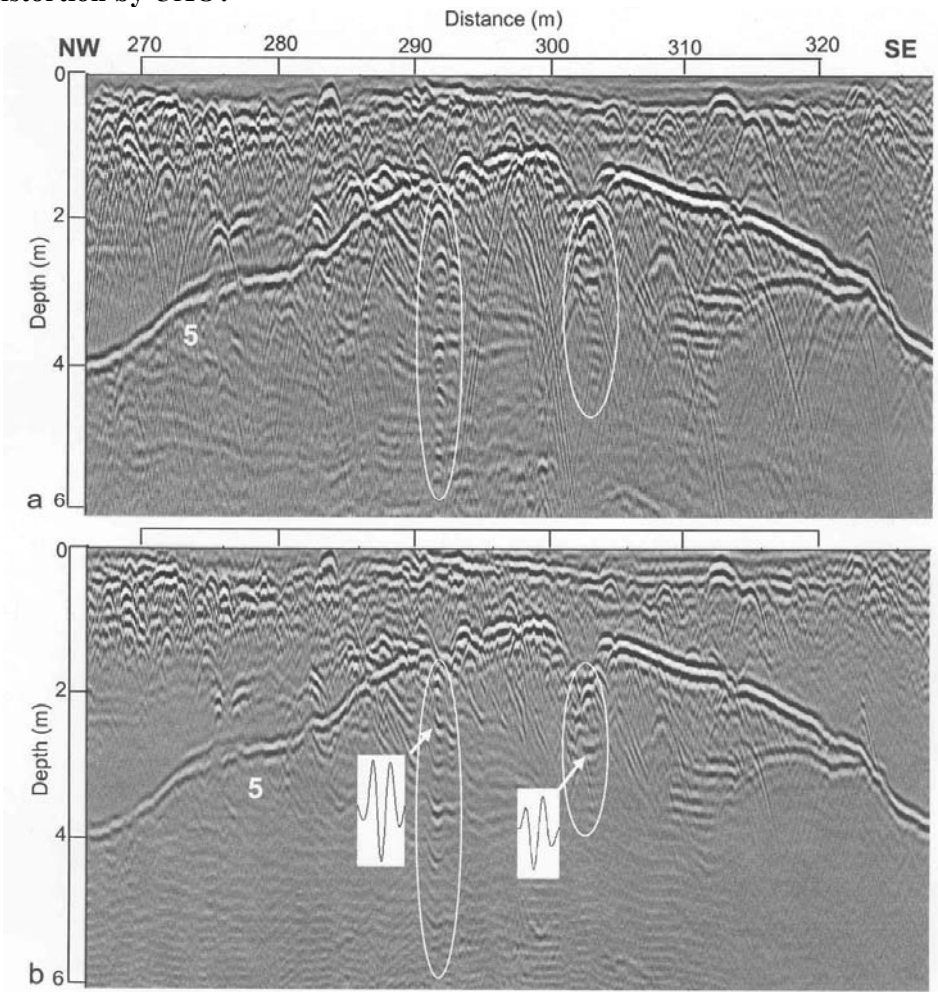

Figure 16. Segment of T27 which shows several depressions in horizon 5 before (a) and after single velocity time migration (b), and + − + waveforms of events beneath the depressions. The ovals contain events which have + − + polarity sequences and evidence of reverberation.

Our profiles contain many examples of strong + − + diffractions buried 2–4 m within sediments beneath shallow water. In these near shore areas we would expect to find stratigraphic evidence of perforation, but there are only a few cases. Two of these are shown in **Figure 16**. **Figure 16a** shows a segment of the profile along T27 with several apparent perforations or depressions in horizon 5. After single velocity time migration (**Figure 16b**) the depressions are slightly clearer, although the velocity must be too variable to migrate all diffractions properly. The top profile was statically corrected before migration. Both before and after migration, there are events beneath the depressions with + − + polarity sequences, and evidence of multiple reflections of these events. In particular, the + − + events in the right side oval cannot be reverberations of any − + − diffraction events above them because all major reflection interfaces are also − + − and so cannot have reversed phase. 30-MHz low pass filtering failed to reveal any continuous resonance associated with these events, such as discussed below and by Arcone et al. (2006), and so they are not related to reverberation with any interface. Consequently, they are likely to be associated with the structure of the target itself, such as the tailfin assembly (a bomb body is too large to resonate at these frequencies; Chen and Peters, 1997).

Maximum penetration

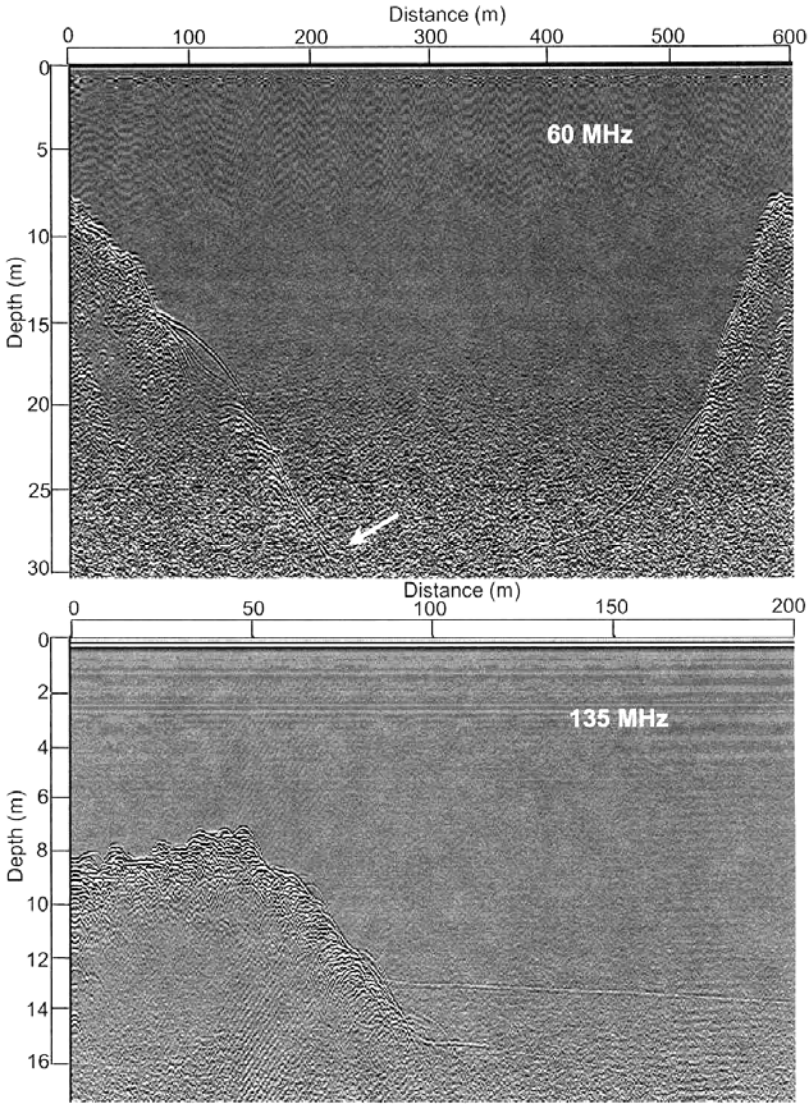

Figure 17. Two examples of deep signal penetration in central Squam Lake. The arrows indicate faint, deeper subbottom reflection horizons. All horizons have the − + − phase polarity sequence.

The maximum known depth of Squam Lake is 30 m, as determined by wintertime drop weight soundings performed by Bradford Washburn (ref map) over many years. **Figure 17** shows two segments recorded in the central section of Squam Lake using 60 and 135 MHz. The bottom varies from bedrock (horizons of diffractions) to sediment (smooth reflection horizons). Returns from 30 m depths are barely visible at 60 MHz (arrow), with additional subbottom penetration. At 135 MHz the water depth is only about 13–14 m, but there is an additional 3 m of subbottom penetration (arrow). At 30 m depth the two-way 60-MHz signal absorption in water alone is 1.7 dB/m giving a total of 52 dB. The additional two-way geometric attenuation (starting at a distance of 1 m) adds 35 dB. A bedrock reflection would give 5 dB of loss whereas a sediment reflection, assuming $\varepsilon = 36$ for saturated silty sediments, would give 14 dB of loss. This places the signal propagation loss for 30 m water depth at −92 to −101 dB at 60 MHz. These figures compare with the maximum 96 dB dynamic range possible for a 16-bit GPR system. The two-way antenna gain is approximately 40 dB for a 20^0 beamwidth in both planes, and this added performance must compensate severe system mismatch losses at the antenna-water interface. In none of our profiles did we obtain a flat interface reflection near 30 m depth.

All horizons have the − + − phase polarity sequence. The smooth sedimentary reflection horizons and the erratic bedrock diffraction horizons all represent material of lower ε than the water and so the waveform of the transmitted signal is preserved. As seen below, internal sedimentary layers are also primarily − + −.

Ground truth: side scan sonar survey, photography and other procedures

Regardless of the overwhelming GPR evidence for subbottom UXO at JEP, the results of a different approach are needed to absolutely identify a few targets. Unfortunately this has been difficult but we have not given up hope. The first procedure tried by Shaw Environmental was an EMI survey, conducted at depth just over the subbottom. As anticipated this survey revealed only the presence of metal objects whereas the GPR could also reveal depth, exact placement, and in some cases when the transect was in a favorable directions, length. The second procedure was a side scan sonar survey conducted by Garry Kozak, private consultant, October 10, 2006. The third procedure was bottom photography. In March, 2007, Mr. Kozak obtained limited bottom photography from the thick ice cover. The ice allowed precise positioning but little mobility, and the time of year minimized vegetation. In addition, there was no natural light to augment the spotlights he lowered and no results were obtained. A second photographic survey was conducted July 21, 2007 in which the camera and lighting were moved over several dozen transects. This revealed about 35 objects, all of which were partly covered by light sediment which precluded identification. Mr. Kozak concluded that many of the objects seen by the side scan sonar were probably not UXO but crayfish holes. The sedimentary covering confirms the GPR results.

A fourth procedure was a magnet demonstration conducted July 2008 by personnel from Tyndall Air Force Base. This method attempted to extract UXO from the near shore subbottom with a large electromagnet swept by a large excavator in 20 foot diameter arcs. The equipment was remotely operated at a distance of over 1850 feet (radius of shrapnel from a 100 pound bomb). The survey recovered 20 mm rounds, a 100 pound bomb casing and various shrapnel, and their locations was recorded with GPS. In anticipation of this procedure, we conducted a preliminary GPR survey of the shorelines in January, 2008, and will conduct a post survey January, 2009. Many targets recovered did in fact, occur where we found dense concentrations of targets. At the time of this writing, the long range plan is to use this magnet to dredge the entire pond from a pontoon platform. However, the possibility of detonation is serious and it appears there is no safety procedure for dealing with underwater explosions. Consequently I have

researched current understanding of underwater explosions with regard to effects at the surface and report this information, with references on p. 57–58.

Side scan sonar is a method for imaging the bottom; there is no subbottom penetration because of the very high frequency (100 kHz) of the signal. It was intended to identify all bottom surface objects and hopefully, to distinguish UXO from logs or boulders, the latter of which must have the − + − phase signature for their events. Some of these events occur as short reflections (**Figure 18**) of 2–6 m apparent length, which suggests they are logs, which were tied together and used extensively to support floating targets. It is also improbable that boulders would be situated within these sediments, especially near the surface. The side scan sonar results are shown in **Figures 19 and 20**. The targets detected are either very localized, or several meters long with a width much less than the length, and so are logs. Their frequency is most likely due to the detonations along the shores, which have been observed to immediately cut down trees. The area outlined in the center show virtually no targets, which is consistent with our deep basin results that show probable UXO under sediment layer.

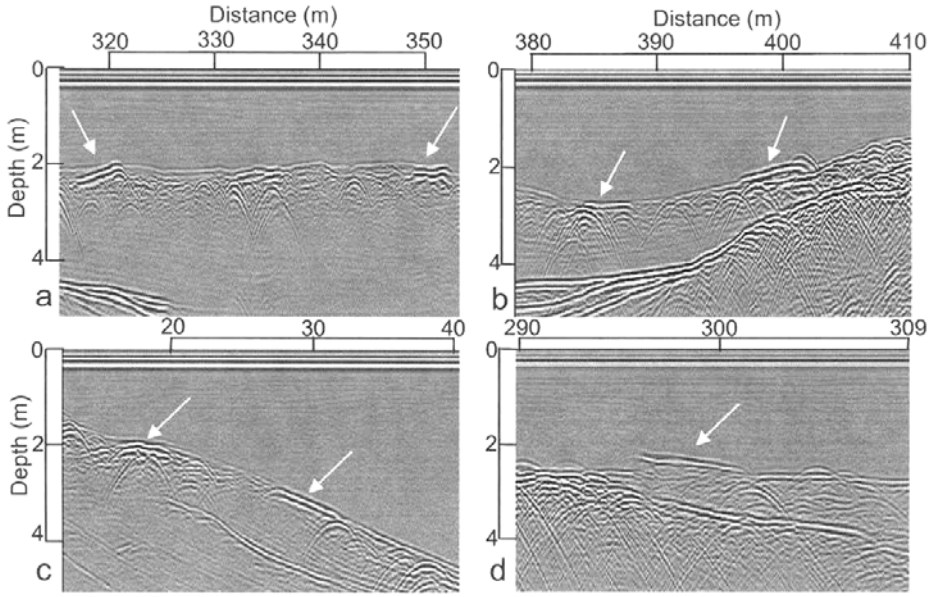

Figure 18. Examples (arrows) of extended reflections recorded along T26 (a, b), T25(c), and T20 (d), which we interpret to be logs.

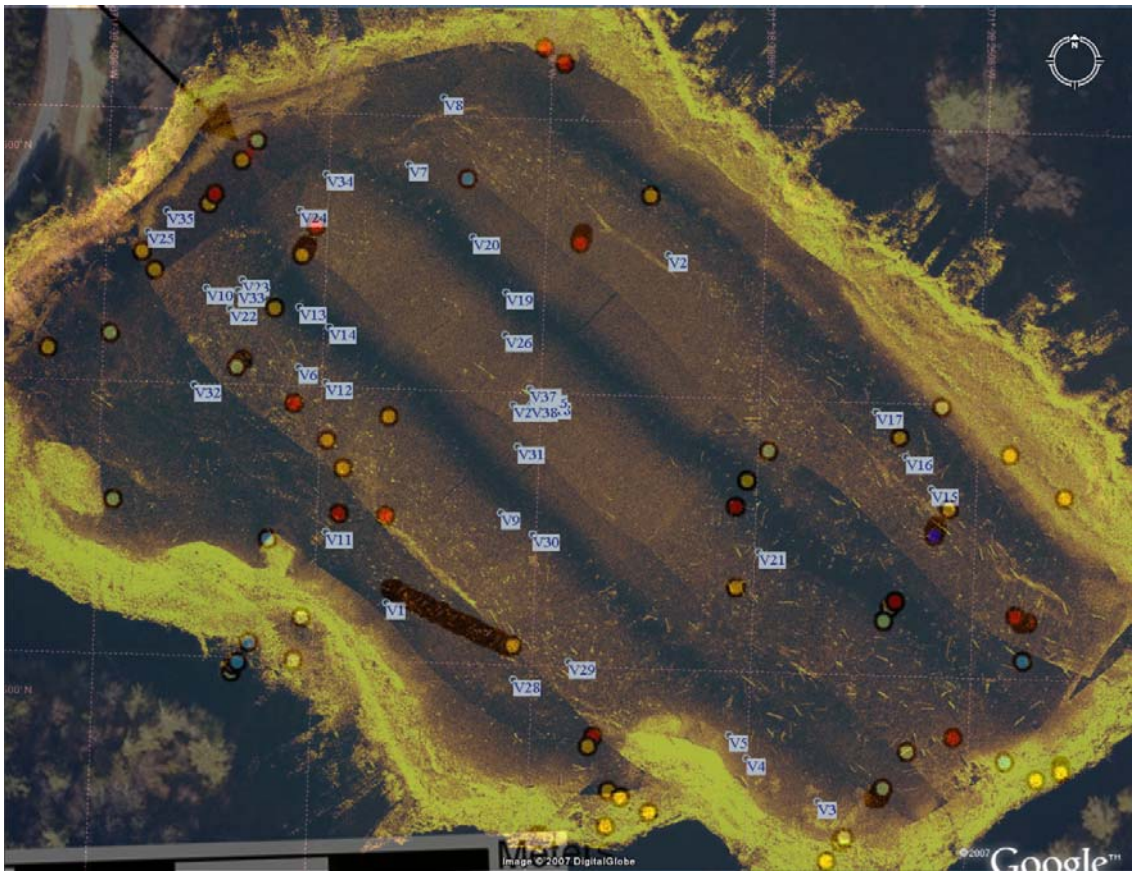

Figure 19. Overlap of GPR targets detected on the bottom surface, and those imaged by the photography.

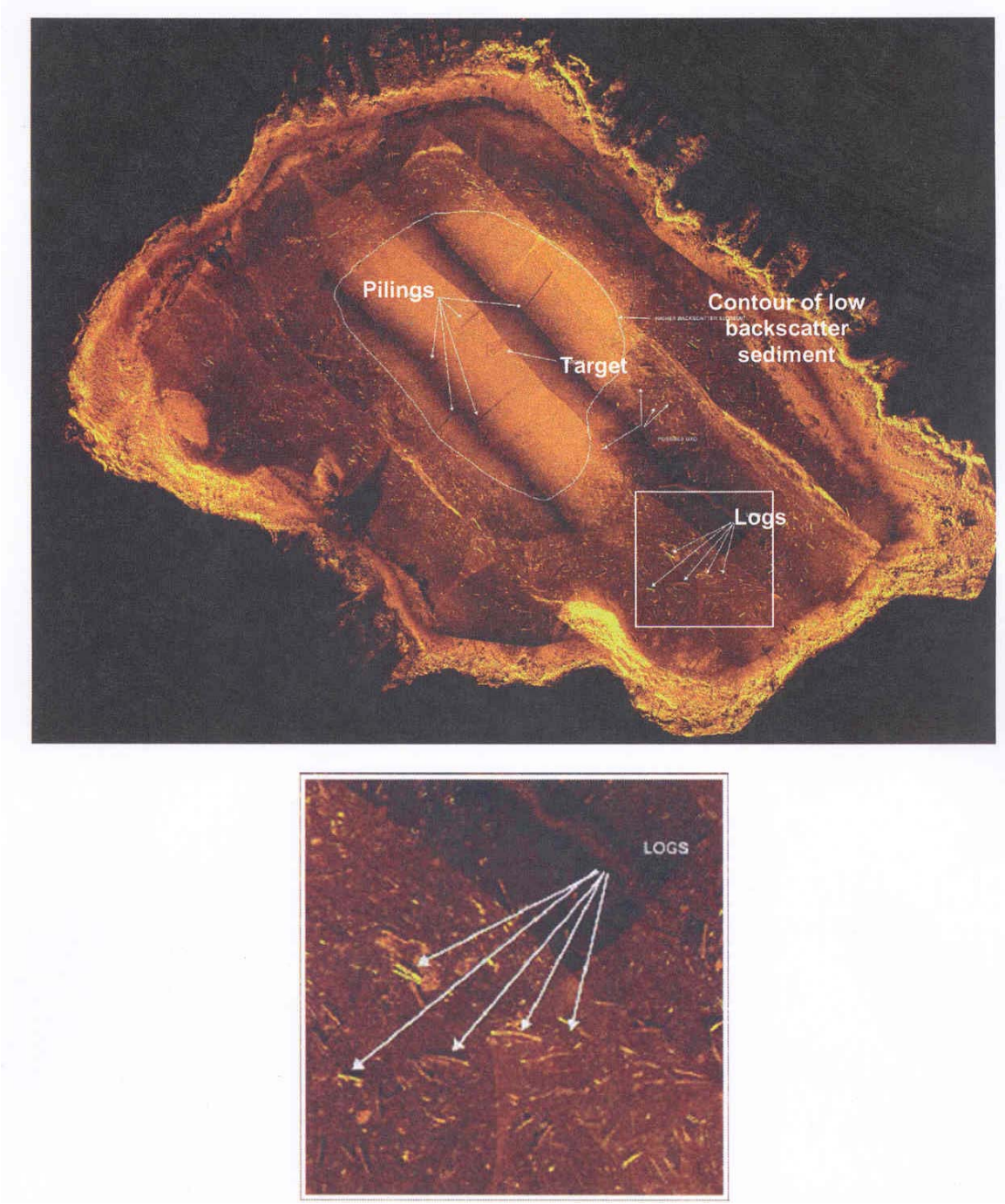

Figure 20. 100-kHz side scan sonar survey of JEP, and detail showing image of logs.

Table 2 shows the record of objects photographed. "Targets" means staging platforms. According to the contractor (Kozak) "The bottom of JEP was found to be heavy sediment and the visibility varied from poor to very poor. Targets located include varied metal objects, logs, bombing wood target, and misc. The many small point contacts observed from the side scan sonar are not UXO, and I suspect they are some other reflecting anomaly, possibly crayfish holes. Observations confirmed there is not a high density of visible targets as first concluded from the side scan sonar survey. Observations also showed that some logs were almost totally covered

with sediment. This leads to the conclusion that most small ordnance if present are beneath the sediment." This statement verifies the conclusions of the GPR that most targets are buried.

Table 2: Record of objects photographed beneath JEP, July 21, 2007.

VIDEO NUMBER	OBJECT DESCRIPTION	TIME	LATITUDE	LONGITUDE
V1	UNKOWN	15:35:38	42 56.0606	071 38.3836
V2	METAL OBJECT	15:46:06	42 56.1259	071 38.3219
V3	LOG AND STUMP	14:59:52	42 56.0266	071 38.2837
V4	METAL OBJECT	14:57:44	42 56.0341	071 38.3002
V5	LOG	14:56:53	42 56.0383	071 38.3044
V6	LOG	14:32:25	42 56.1034	071 38.4054
V7	BOMB?	14:28:13	42 56.1410	071 38.3818
V8	UNKOWN	14:26:47	42 56.1534	071 38.3743
V9	UNKOWN OBJECT	14:10:13	42 56.0777	071 38.3581
V10	CRAYFISH HOLES	13:49:04	42 56.1175	071 38.4268
V11	METAL OBJECT	19:04:49	42 56.0732	071 38.3978
V12	ROCKS OR METAL	18:59:45	42 56.1007	071 38.3990
V13	BOMB?	18:56:32	42 56.1144	071 38.4055
V14	UNKOWN OBJECT	18:53:57	42 56.1109	071 38.3986
V15	OBJECT	18:44:10	42 56.0842	071 38.2602
V16	LOG	18:42:40	42 56.0899	071 38.2662
V17	LOG	18:40:36	42 56.0982	071 38.2734
V18	ROCKS ?	18:25:29	42 56.0983	071 38.3491
V19	OBJECT IN MUD	18:22:54	42 56.1181	071 38.3586
V20	OBJECT	18:21:20	42 56.1280	071 38.3666
V21	TYPICAL BOTTOM	18:05:17	42 56.0718	071 38.2989
V22	BARREL OBJECT	17:45:26	42 56.1138	071 38.4214
V23	BOMB?	17:43:52	42 56.1191	071 38.4188
V24	LOG	17:41:43	42 56.1321	071 38.4061
V25	BURIED LOG	17:36:23	42 56.1275	071 38.4406
V26	SILT EXAMPLE	17:24:10	42 56.1103	071 38.3585
V27	OBJECT	17:08:01	42 56.0977	071 38.3561
V28	LEAVES	17:03:07	42 56.0473	071 38.3541
V29	LEAVES	17:01:42	42 56.0508	071 38.3414
V30	BOMB?	16:57:21	42 56.0739	071 38.3507
V31	2 SMALL TARGETS	16:55:15	42 56.0897	071 38.3548
V32	BURIED LOG	17:47:43	42 56.0997	071 38.4289
V33	TYPICAL BOTTOM	17:44:23	42 56.1172	071 38.4196
V34	TARGET OUT OF BOTTOM	17:40:45	42 56.1389	071 38.4004
V35	BLOCK	17:35:51	42 56.1313	071 38.4364
V36	OBJECT	17:31:35	42 56.0995	071 38.3500
V37	TARGET FOR BOMBING	17:26:27	42 56.1006	071 38.3525
V38	TARGET FOR BOMBING	17:30:20	42 56.0978	071 38.3522

ACCOMPISHMENTS: COMPLEX PERMITTIVITY AND MINERALOGY OF SEDIMENTS

Overview

Our two most important objectives are to understand the cause of signal penetration in subbottom sediments, and to interpret evidence for stratigraphic distortion and disruption by UXO. The penetration objective rests on understanding the role of fine-grained sediments. As detailed next, many have thought that it only takes a clay or silt-rich sediment to strongly attenuate. This does not seem to be the case. We believe it is the mineralogy and, in particular, the presence of phyllosilicate clay mineral the most important of which is smectite.

Wet clay minerals strongly absorb electromagnetic energy over a wide frequency range that extends across the 50–1000 MHz bandwidth of ground-penetrating radar (GPR). Although field observations show that clay-size fractions strongly correlate with GPR attenuation rates (Doolittle et al., 1998, 2002; Arcone et al., 2003), and laboratory measurements of ε^* on natural soils containing clay-size fractions have covered the GPR bandwidth (Hoekstra and Delaney, 1974; Peplinski et al., 1995; Sabburg et al., 1997), no one has attempted to quantify the roles of the individual grain sizes or the individual minerals without isolating them. The clay-size effect is enhanced by phyllosilicate clay mineralogy, which is generally, but not totally, confined to the clay-size range (Mitchell, 1993). The large, charged specific-surface areas of the phyllosilicate smectite minerals (hundreds of $m^2\ g^{-1}$) retain water within structures known as galleries. Mineral surface charge and hydrated ions within galleries produce extremely large complex permittivity (ε^*) values and strong dielectric relaxation centered below 1 MHz (Kaviratna et al., 1996; Rotenberg et al., 2005) that may compete with higher frequency relaxations centered at tens of MHz and related to the activity of the adsorbed water itself (Ishida et al., 2000; Hilhorst et al., 2001; Rotenberg et al., 2005). Above 1 GHz gallery water exhibits Debye-type relaxations characteristic of adsorbed and free water orientation polarization (Sposito and Prost, 1982; Rotenberg et al., 2005). Non-smectite phyllosilicates such as kaolinite and illite also produce large ε^* values as frequency drops below the GPR bandwidth (Ishida et al., 2000). In this paper we investigate the possible permittivity control of grain-size fraction and clay minerals within a natural soil.

Theoretically, particle size affects ε^* of soil because decreasing size increases specific surface area, which converts free water to adsorbed water. Water adsorbed directly on mineral surfaces has a significantly lower ε^* than does free water (Or and Wraith, 1999). However, below about 1 GHz, the only significant effects on ε^* should be provided by clay-size (< 2 μm grain diameter) particles because silt sizes (2–67 μm) have only a few (at most) $m^2\ g^{-1}$ of specific surface area. Consequently, we first sought to test the hypothesis that across the GPR bandwidth particles of silt size and larger, within a natural mineralogically complex soil and at a fixed volumetric water content, should show little dispersion, attenuation rates of a few dB m^{-1} or less, and consistent values of ε^*. Our objective, then, was to measure the frequency spectra of ε^* for various silt- to clay-sized grain fractions, including that of the whole soil from which the fractions were derived. We chose the natural Fairbanks silt (Péwé, 1955) to obtain a mixed mineralogy. Scanning electron micrographs we made (**Figure 6**) showed pits and etchings that might increase the surface area significantly. We used standard procedures to separate grain size fractions, and measured ε^* using full-reflection time domain spectroscopy (TDS) to provide a bandwidth of 25 MHz to 2–4 GHz. We used one temperature and held the volumetric water content, θ_W, for all

sizes near 0.3, which is below saturation yet sufficient to ensure significant, if not complete, hydration of silt and clay particles.

Our results however, contradicted our expectations for silt. The magnitude and progressive strengthening of the real (ε') and imaginary (ε'') parts of ε^* from coarse silt to clay-size fraction as frequency decreased below about 500 MHz suggested that either the silt sizes significantly affected ε^* or that clay minerals were not effectively removed from the silt-size fractions prior to measurement. Consequently, we expanded our objectives to determine the amount of clay minerals within the grain size fractions and their possible contributions to the ε^* spectra. We used X-ray diffraction (XRD) to identify the major minerals, ε^* measurements of the key clay phyllosilicates, and a mixing model that accounted for a spectrum of known relaxations in one clay mineral in an effort to reproduce our data and understand any competing processes between grain size and mineralogy.

Silt is a major component of many soils. In general, silts and sands in temperate and polar regions are composed primarily of quartz, feldspars and the mica minerals muscovite and biotite. Silty soils of glacial or aeolian origin cover thousands of square kilometers of the U.S. (Rodbell et al., 1997; Muhs et al., 1999; Grimley, 2000) and Alaska. Our Fairbanks silt (Péwé, 1955) is similar to these soils.

We argue that the clay mineral content within each grain size was the primary cause of variations in ε^* below about 2 GHz. The primary variations are in the strength of the low-frequency relaxations, as determined by the modeled volumetric water content of just the smectite mineral and the static value of permittivity for free water. The excellent fit of our smectite-based model with the measured ε^* for the two finest grain size fractions, and the similarity of the measured montmorillonite ε^* to that of < 2 μm fraction, strongly suggest that smectite dominated these fractions, and that kaolinite and illite may have been as effective as smectite for the two coarsest sizes.

Real component of ε'

The ε' for all fractions and the whole soil is shown in **Figure 21a**. More detail for ε^* of the individual grain sizes is shown later in our modeling exercises. The dependency on frequency appears to be divided into three regimes. Below about 500 MHz, ε' increases with decreasing frequency for all data sets and with decreasing grain size. The two finest sizes show the most rapid increase, with the < 2 μm size beginning to rise just below 1 GHz. Only ε' for the >20 μm size is reasonably constant between 100 MHz and 3 GHz. Below about 200 MHz, the values for the whole soil reside between those for the two coarsest grain sizes, and its overall behavior is most similar to that of the 10–20 μm fraction. Between about 500 MHz and 2–4 GHz is a crossover regime where all data sets except that of the > 20 μm fraction are near $\varepsilon' = 19.5$. The > 20 μm fraction is at about $\varepsilon' = 17$. Above about 4 GHz all sizes show a significant decrease in ε' with increasing frequency. Although this general behavior is expected because of free water relaxations, the decrease is too rapid. For example, the ε_∞ cannot be < ~ 4, given the θ_a and θ_w values of **Table 1**, but this value is nearly obtained for the 10–20 μm fraction by 10 GHz.

The error bars shown in **Figure 21** are based on our calibrations with ethanol and conductive water. They show a possible 13% experimental error (measured values are too low) in ε' by 5 GHz and 7% (too high) at 25 MHz. The error appears to be less than 3% from 200 MHz to 2 GHz; errors due to system performance within this frequency range appear to be negligible. Consequently, the closeness and crossing of ε' for the various grain sizes between 500 MHz and 2 GHz are real. Given the slightly different values of θ_w, the closeness may be caused

by differences in density and porosity (**Table 1**). However, our modeling (discussed later) suggests that this frequency range is where lower frequency clay relaxations modulate the ε' of water to keep these values close.

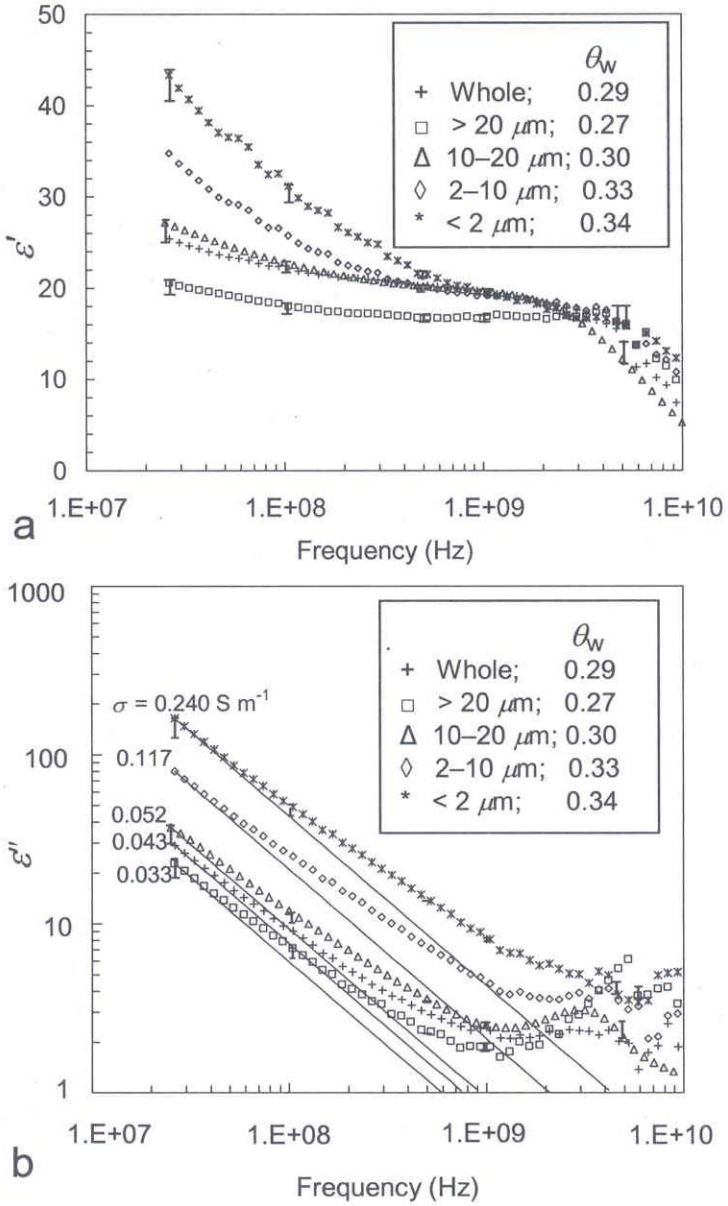

Figure 21. Plots of ε' (a) and ε'' (b) for the various grain sizes. The legend gives the grain size in μm followed by the total volumetric water content. Error bars are shown for the > 20, 10–20 and > 2 μm data sets. The straight lines in (b) plot the dependence of ε'' on σ alone for σ values based on the ε'' value at 25 MHz.

Imaginary component of ε'

As with ε', ε'' increases with decreasing frequency with decreasing grain size below 1 GHz (**Figure 21b**). Below about 2 GHz ε'' of the fractions are separated; i.e., there is no crossover, as seen in Figure 3a. In the log-log scale ε'' for all fractions appears to approach linear

behavior asymptotically below about 100 MHz, and with a first-order slope, which means it is becoming dominated by σ. The straight lines are ε'' values generated by the equivalent σ values derived from the value of ε'' at the lowest frequency. The whole soil, the >20 μm fraction, and the < 2 μm fraction appear to have achieved a linear logarithmic dependency below about 40 MHz, while the other two fractions are close to linear by 25 MHz. The equivalent σ values of 0.043 (whole soil) and 0.033 S m^{-1} (> 20 μm) at 25 MHz are close to field-measured values of 0.025 S m^{-1} at saturated water contents (Arcone and Delaney, 2003).

The relaxations above 1 GHz are associated with orientation polarization in water, and should be centered between 15 and 20 GHz for free water (Njoku and Kong, 1977; Ishida et al., 2000). The possibility of an orientation type of relaxation centered between about 1–4 GHz is discussed later. However, no peaks in ε'' occur at any fraction which compare in strength with the corresponding ε' at that frequency, as required by relaxation theory. Our calibrations suggest significant errors above 4 GHz are possible. Consequently, we think that the frequency placements of any relaxations above 1 GHz suggested in these data are unreliable.

Attenuation rates

The one-way attenuation rates (**Figure 22**) steadily increase with frequency because of the frequency dependence seen in equation (4). As with ε'', there is no crossover below 2 GHz. Some of these values are summarized later in **Tables 6 and 7** over different GPR bandwidths. The lowest rate at 100 MHz is still a significant 16 dB m^{-1} for the > 20 μm fraction. At 1 GHz the rate increases to 43 dB m^{-1}. The < 2 μm fraction varies from 70 to 171 dB m^{-1} between 100 MHz and 1 GHz. The round-trip rate of 140 dB m^{-1} at 100 MHz exceeds the performance figure of commercial radar systems at this pulse center frequency. The whole soil range of 18−50 dB m^{-1} at 100−1000 MHz is close to the range (22–53 dB m^{-1}) for the 10–20 μm fraction, even though this fraction constitutes only 7.5% by weight of the whole soil.

The attenuation rate for the three coarser sizes increases more rapidly above 1 GHz than below, but without overtaking the rates for the two finest sizes. This is caused by the better separation between the ε'' response to the orientation polarization relaxation and its response to the lower conductivity values.

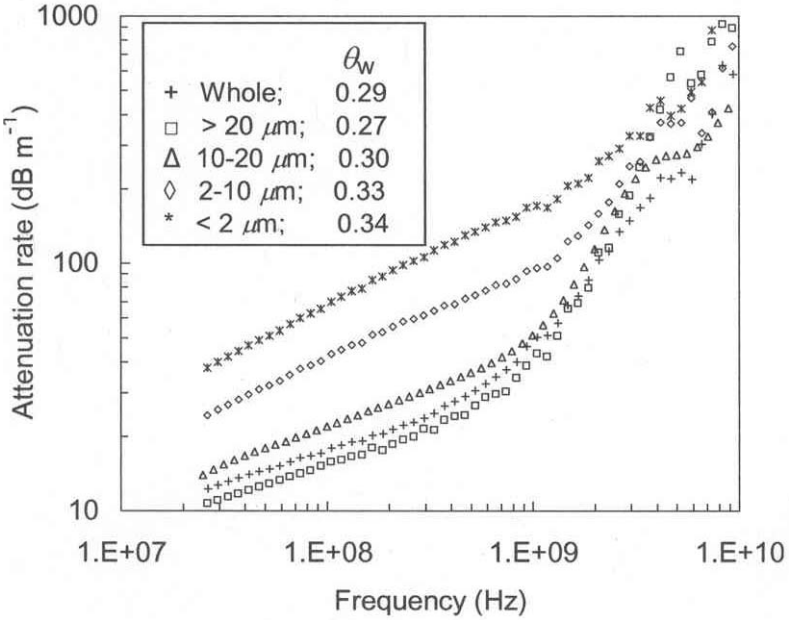

Figure 22. One-way attenuation rates for each grain size fraction.

Mineralogy

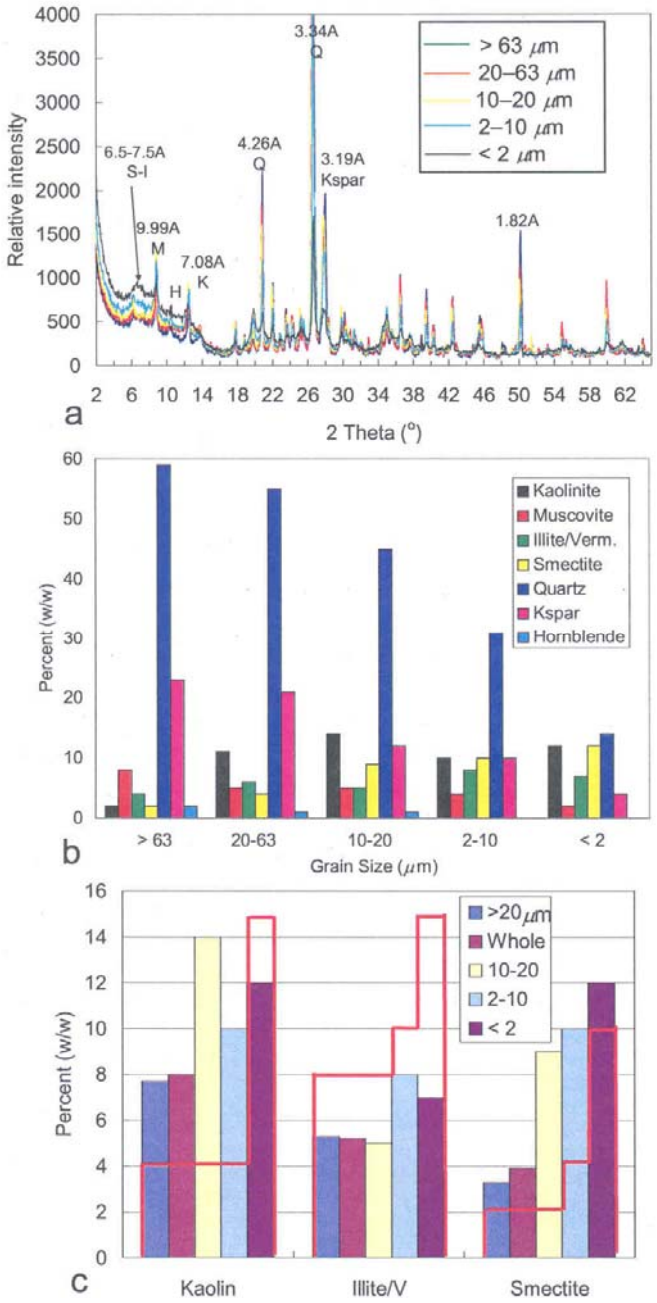

Figure 23. XRD spectra for all grain sizes (a), the mineral percentages for the whole fractions by weight (b), and the mineral percentages of the clay minerals for the fractions (c). The illite may include vermiculite (V). In (a) the major minerals identified are smectite (S), illite (I), mica (M), hornblende (H), kaolinite (K), quartz (Q), and potassium feldspar (Kspar). In (b), the whole weight reference includes the amount of amorphous material. The bar graphs in (c) are our measurements. The red lines in (c) are from the independent laboratory, which did not differentiate illite from mica.

We show a composite of the XRD spectra for all fractions in **Figure 23a** and summarize our XRD mineralogy percentage weight determinations in **Figures 23b** and **23c**. In **Figure 23c** and in **Tables 3 and 4**, discussed below, we averaged the > 63 and 20–63 μm values to determine the > 20 μm values. The important mineral peaks are identified in the spectrum. Those above 2 $\Theta = 30^{o}$ are other peaks of the same minerals. The amorphous (non-crystalline) components are accounted for to bring the total to 100% for each fraction in **Figure 23b**. We find the whole soil to have quartz at 52%, potassium feldspar at 20%, mica at 6%, hornblende at 1%, kaolinite at 8%, illite at 5%, smectite at 4%, and amorphous material at 3%. This gives a total of 17% for the

three phyllosilicate clays, which is appreciably more than the 2.4% clay fraction found by separation. At sizes >2 μm all three could exist as finer silt-size particles, as particles still adhered to surfaces (**Figure 6a**), as weathered products on or within the mica or feldspar grains (**Figure 6b**), or associated with aggregates that were not effectively dispersed during chemical pretreatment. Kaolinite and montmorillonite particles can occur as large as 10 μm (Mitchell, 1993). We have not identified the amorphous phases, but they may include secondary silica, possibly iron oxides and poorly crystalline phyllosilicate clays.

The independent laboratory reported 67% quartz and 15% feldspars; Péwé (1955) found 66–68% silica and 15–20% alumino-silicates (mainly feldspars and clay minerals) by weight using non-XRD methods. They also found kaolinite, illite, and smectite to be the main clay minerals and to exist in all fractions. They generally agreed with our finding that smectite generally increases in fractional percentage with decreasing grain size (**Figures 23b, c**) and that illite generally increases with decreasing grain size, but could not be distinguished from mica, which we found in comparable amounts. Of the three clay minerals, only smectite is an "expandable" mineral, which means that it retains water within the galleries between mineral surfaces. It is likely that the smectite is montmorillonite.

Table 3 summarizes the clay mineral percentages by weight in **Figures 23b or c**; i.e., the percentage of amorphous material in each fraction is considered. The table shows that the total clay mineral content was nearly constant for the three smallest grain size fractions, despite separation. However, **Table 4** shows different results when the total weights of all minerals are normalized to 100%; i.e., the percentage of amorphous material in each fraction is not considered. In this case all three clay minerals, as well their total, increases in percentage weight with decreasing grain size. This agrees qualitatively with the results of the independent laboratory, which found a general increase for each mineral (**Figure 23c**) and for the total clay mineral content with decreasing grain size, although they could not distinguish mica from illite. Specifically, they report total percentages of 15, 15, 20, and 40% for the > 20, 10–20, 2–10 and > 2 μm fractions, respectively. These results thus suggest that either smectite (which is the most hydrophilic), all three clay minerals or both had a significant role in determining ε^*. We therefore performed additional measurements of ε^* on each mineral.

Clay mineral	> 20 μm	10–20 μm	2–10 μm	< 2 μm
Kaolinite	8	14	10	12
Illite	5	5	8	7
Smectite	3	9	10	12
Total	16	28	28	31

Table 3. Mineral percentages by weight for non-normalized grain size fractions based on our XRD measurements; i.e., the percentage of amorphous material is considered.

Clay mineral	> 20 μm	10–20 μm	2–10 μm	< 2 μm
Kaolinite	8	15	14	24
Illite	5	5	11	14
Smectite	3	10	14	24
Total	16	30	39	62

Table 4. Mineral percentages by weight for normalized grain size fractions based on our XRD measurements; i.e., the percentage of amorphous material is not considered.

Clay mineral ε^*

Figure 24 compares our measurements of ε^* for sodium-saturated montmorillonite with sodium-saturated illite and sodium-saturated kaolinite. Sodium is a common cation found within the interlamellar galleries. For absolutely dry kaolinite, illite and montmorillonite Robinson (2004) reports ε' values of 5.1, 5.5, and 5.5, and Meunier (2004) gives measured specific surface areas of 20, 100 and 850 $m^2\ g^{-1}$, respectively. For our measurements the value of θ_W is slightly less for the montmorillonite (0.34) than for the illite (0.37) and slightly more than for the kaolinite (0.31). The wet bulk density for the montmorillonite (1.92 g cm^{-3}) is less than that of the illite (2.18 g cm^{-3}) and very slightly less than that of the kaolinite (1.96 g cm^{-3}).

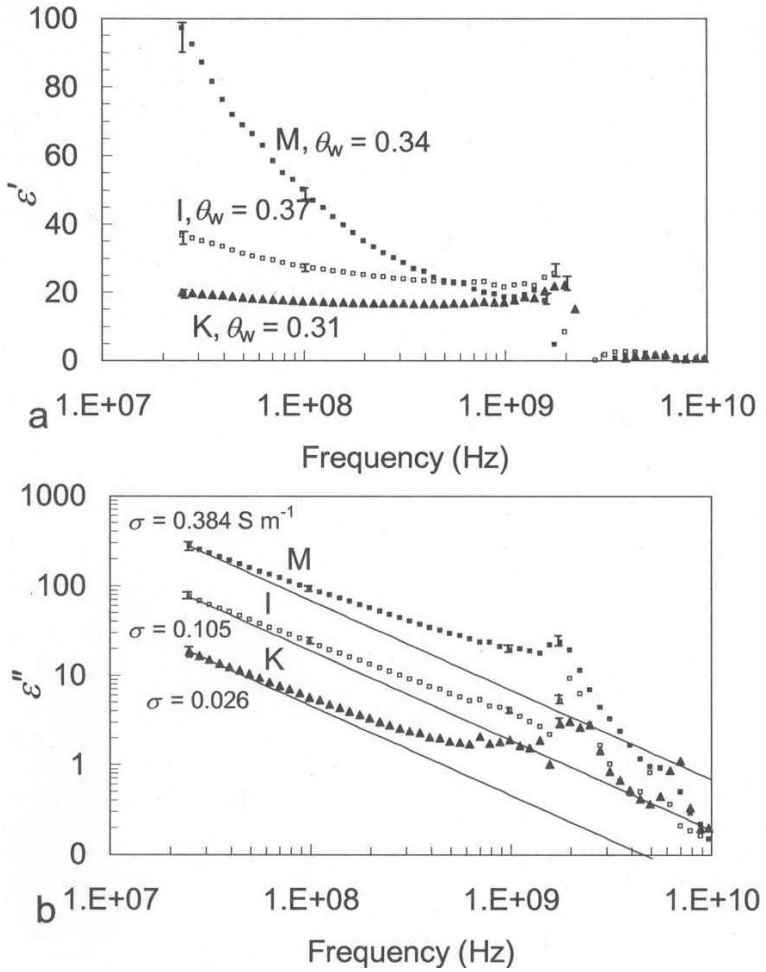

Figure 24. Comparison between the complex permittivities of sodium-saturated montmorillonite (M), illite (I) and kaolinite (K) at similar volumetric water contents of 0.34 (M), 0.37 (I) and 0.31 (K). Near-zero or negative values occur above 2 GHz in (a). Equivalent conductivity values calculated at the lowest frequency are shown in (b). Error bars not shown at 500 MHz and 1 GHz are equal to or less than the vertical width of the data points.

Despite the lesser values of θ_W and wet bulk density, as frequency decreases below about 600 MHz ε' of the montmorillonite increases more strongly than does ε' of the illite, and far more strongly than that of the kaolinite, which has a very similar wet bulk density and only 3%

less θ_w than does the montmorillonite (**Figure 24a**). By 25 MHz ε' reaches 97, 37 and 25 for the montmorillonite, illite, and kaolinite, respectively. From 500 MHz to about 2 GHz the montmorillonite and illite ε' values are similar, as they are for the grain fractions in Figure 3a. The illite and kaolinite ε' are slightly more and slightly less than that of the montmorillonite above 500 MHz, and this should be caused primarily by the slightly greater and lesser values, respectively, of θ_w. Error bars in ε' below about 2 GHz are of the same magnitude as shown in Figure 3a. Therefore, the closeness in ε' is also likely to be caused by free water in the smectite galleries, as discussed later, and around the illite and kaolinite because they have a far smaller specific surface area; at this high value of θ_w the illite and kaolinite surfaces are totally covered in adsorbed water, leaving much free water.

The values of ε'' for the montmorillonite are also greater and much stronger than ε'' for the < 2 μm fraction in **Figure 21b**. The greater montmorillonite equivalent σ value of 0.384 S m^{-1} (compared with 0.240 for the < 2 μm fraction) is consistent with a greater ionic mobility. As occurs for the < 2 μm fraction in **Figure 21b**, in the log-log scale a linear dependency on frequency appears to be approached below 100 MHz. Similar behavior has been reported for montmorillonite (Calvet, 1975; Bidadi et al, 1988; Ishida et al, 2000; Rotenberg et al., 2005) and sand-montmorillonite mixtures (Knoll and Knight, 1994) over portions of a wide frequency band ranging from several GHz to hundreds of Hz. Below about 1.5 GHz the 10.53 mm pin provides much more instability and values of ε'' appear unreliable.

Effective medium model: CRIM method

Although the percentages of smectite are not significantly different from those of illite and kaolinite across all fractions, the affinity of smectites for water, the results in **Figure 24**, and the increasing percentage of smectite with decreasing grain size make this mineral a primary candidate for dominating the permittivity of our grain size fractions. We constructed an effective medium model that incorporates the known properties of wet montmorillonite to test its influence on the gradient of ε' as frequency decreases below about 1 GHz, the dominance of conduction effects as frequency decreases, and the leveling of ε' at a moderately high value from 100 MHz to 1 GHz for the coarser grain sizes. We sought to keep our rms percentage errors < 5% and a total absolute rms error equal to or less than unity below 1 GHz in matching model to data.

We used the Complex Refractive Index Method (CRIM) (Wharton et al., 1980; Shutko and Reutov, 1982) to compute an effective complex refractive index, n^*_{eff}, such that

$$n^*_{eff} = \theta_a n^*_a + \theta_m n^*_m + \theta_{wf} n^*_{wf} + \theta_{ws} n^*_{ws} , \quad (5)$$

where

$$\varepsilon^*_{eff} = (n^*_{eff})^2. \quad (6)$$

The subscripts refer to the individual components of air (a), mineral matter (m), free water (wf) and water adsorbed within smectite galleries (ws), and θ is the component volumetric fraction. The quantity θ_{ws} is the volume fraction of water affected by both the low-frequency (centered below 1 MHz) relaxation that is characteristic of smectite clays (discussed below) and the high-frequency (centered above 1 GHz) relaxations of free water; we do not consider any high-frequency relaxation of adsorbed water, as discussed below. The quantity θ_{wf} is water affected

by only the high-frequency relaxation, which may or may not be in smectite galleries (discussed below). The total volumetric fraction of water is $\theta_w = \theta_{wf} + \theta_{ws}$. We assigned each component the same value of σ (except air; $\sigma_a = 0$). Generally, equation (5) should be considered when loss terms are significant, as our ε'' data shows. If not, then only the real parts need be considered such that

$$n'_{eff} = \theta_a n'_a + \theta_m n'_m + \theta_{wf} n'_{wf} + \theta_{ws} n'_{ws}. \quad (7)$$

The physical justification for equation (7) is that it applies to materials where the wavelengths are much greater than the dimensions of the dielectric or conductive inhomogeneities. An insitu wavelength of 1 cm for example (5 GHz at $\varepsilon' = 36$) is still 50 times greater than our maximum particle size of 200 μm. Consequently, the formula expresses a summation of average delay times through each soil constituent and so has been referred to as the Time of Propagation method (Knoll and Knight, 1994). The complex equation (5) also accounts for cumulative attenuations caused by the various components. This physical justification led us to choose this model rather than others based on different exponential mixing factors. There is no geometric structure factor in this simplified approach. Grains, parts of grains such as water layers bound by mineral surface charge, and mineral surfaces are considered polarizable entities in themselves and unaffected by neighboring entities.

Components

The minerals in Fairbanks silt are non-dispersive and virtually lossless in our frequency band. Their values of ε' are 4.5 for quartz, 5.6 for potassium feldspar (Olhoeft, 1989), 5.1, 5.5, and 5.5 for kaolinite, illite and montmorillonite, respectively (Robinson, 2004), and 6.2–8.0 for muscovite mica (Keller, 1988). Montmorillonite is the most common smectite.

We express the complex refractive index of our mineral component as

$$n^*_m = (\varepsilon'_m - i\sigma/\omega\varepsilon_0)^{0.5}, \quad (8)$$

for which the ε_m' values were determined with equation (7) and the mineral component percentages (the weight percentages are assumed equal to the volumetric percentages because the densities of each mineral are so similar) of each grain size fraction in **Figure 23b**. This procedure provides $\varepsilon_m' = 5.1 \pm 0.15$ for all fractions so we used $\varepsilon_m' = 5.1$. No significant change in the modeling results if a slightly lower or higher value is used, such as by decreasing the amount of quartz or increasing the amount of feldspar by several percent. We regard any electrical double layer on, or water adsorbed to the outside of grain surfaces to make an insignificant contribution to the permittivity relative to the smectite galleries, and only sufficient to supply the DC conduction.

We use the Debye form for dielectric relaxation processes for the water components. These relaxations may be caused by a variety of polarization mechanisms, the most likely of

which we describe below. The relaxation process may be described generally by the Cole-Cole formulation (Cole and Cole, 1941; von Hippel, 1954)

$$\varepsilon^* = \varepsilon_\infty + (\varepsilon_\infty - \varepsilon_s) / (1 + (f / f_r)^{1-\alpha}), \quad (9)$$

where ε_∞ is the high-frequency asymptotic value of ε', ε_s is the low-frequency or static value of ε', and f_r is the relaxation frequency (von Hippel expresses the ration in the denominator in terms of radian frequency and relaxation time). We express multiple relaxations as a linear combination of relaxation processes (Arkhipov, 2002) in which ε_∞ must be used only once. The exponent α lies between 0 and 1.0 and accounts for spectral broadening, caused by either molecular collisions or a continuum of relaxations. A value of α may reduce the variation within ε' and ε'' over the relaxation spectrum and extend the dispersion over a wider bandwidth.

We assume that the smectite portion of water, θ_{ws}, exhibits characteristic montmorillonite low-, mid- and high-frequency relaxations. The major low frequency relaxation is caused by polarization formed by the negative surface charge at the mineral surfaces and the adsorbed solvated cations close to it (Kaviratna et al, 1996; Dixon and Schulze, 2002; Rotenberg et al, 2005); there is no electrical double layer in the galleries. These ions are in flux both diffusing to and away from the mineral surfaces. Rotenberg et al. (2005) show this relaxation down to 40 Hz. Part of this relaxation appears in the saturated montmorillonite data of Ishida et al (2000). Our relaxation parameters are very close to those of Rothenberg et al. (2005). The low-frequency relaxation, $f_{rlo} = O(10^4$ Hz) and $\varepsilon_{slo} \sim O(10^5)$. We modify this to $\varepsilon_{slo} \sim O(10^4)$ because it should be lower as water increases beyond a few molecular layers (Rotenberg et al., 2005).

The mid-frequency relaxations occur mainly between $f = 10^6 - 10^9$ Hz (Sposito and Prost, 1982; Ishida et al., 2000; Hilhorst et al., 2001; Rotenberg et al., 2005) and are associated with this flux of diffusing ions and the activation of adsorption and desorption. For one or two water layers within galleries these relaxations may separate. For a lot of water they may coalesce from collision broadening and multiple relaxations. Consequently, this frequency range for very wet substances may be accounted for by using just one relaxation but with a large Cole-Cole α factor. In our case we apply an α factor to the low frequency relaxation (α_{lo}) to provide a similar effect to about 500 MHz.

The high frequency relaxations above 1 GHz are considered to be caused by orientation polarization (Hasted, 1973) of gallery water in either an adsorbed or free state. Rotenberg et al. (2005) find the relaxation frequencies for one and two water layers in smectite near 0.5 GHz and 3 GHz, respectively. This amount of water is extremely small volumetrically. These relaxation frequencies are consistent with Hoekstra and Delaney (1974) who found relaxation frequencies from 1–3 GHz, but required an additional relaxation with $f_{rhi} = 20$ GHz to model their data for clay-rich soils near 5% volumetric water content but of unspecified mineralogy. Therefore, there must be some minor relaxation near 1–3 GHz in our fractions. However, we declined to incorporate a 1–3 GHz relaxation in our model because at our large water contents the free water relaxation near or above 10 GHz dominates (Ishida et al., 2000); Hoekstra and Doyle (1971) and Sposito and Prost (1982) also found f_{rhi} near 10 GHz for the water within smectite galleries. Furthermore, only the 10–20 μm grain size shows a small suggestion of a relaxation in ε'' centered near 3 GHz. Other reasons justifying this assumption are discussed in the modeling results. Consequently, we assume $f_{rhi} = O(10^{10}$ Hz) and that $\varepsilon_{shi} \leq 78$ at 25° C (our laboratory temperature).

Finally, for the whole water system, we use the $\varepsilon_\infty = 5.6$ for free water (Arkhipov, 2002). Our expressions for n^*_{wf} and n^*_{ws} are then

$$n^*_{wf} = (\varepsilon^*_{hi} - i\sigma/\omega\varepsilon_0)^{0.5} \quad (10)$$

and

$$n^*_{ws} = (\varepsilon^*_{lo} + \varepsilon^*_{hi} - i\sigma/\omega\varepsilon_0)^{0.5}, \quad (11)$$

where ε^*_{lo} and ε^*_{hi} follow the form in equation (9).

We further constrained our models to our measured and known parameters: σ is close to what we calculated (**Figure 21**), θ_w and θ_a are what we measured (**Table 1**) and $\alpha_{hi} = 0$. Our choice of f_{rhi} helped to provide a good fit for ε'' over the whole frequency range. The ε_{shi} values we finally arrived at are effective values. As grain size increases it becomes 78. We keep α_{lo} fairly consistent throughout our models, and it becomes very close to values given by Sposito and Prost (1982; Table III). The critical tradeoff parameters that adjust the important dependency of ε' below 1 GHz are θ_{ws} and ε_{shi}. Consequently, in matching model to data we used a simple trial and error procedure, the checks upon which are that θ_{ws} should generally decrease with increasing grain size while ε_{shi} should generally increase.

Results

We show the CRIM results for all grain size fractions and the whole soil in **Figure 25**. The model parameters are given in the figures and in **Table 5**. The α_{lo}, f_{rlo} , ε_{slo} values are similar for all cases. It is the balance between θ_{ws} and θ_{wf} that primarily changes. We achieved the desired dependence of ε' and ε'' on frequency below about 1 GHz in all cases, while θ_{ws} progressively decreases from 9.0% at < 2 μm, to 7.0% at 2–10 μm, to 6.5% at 10–20 μm, to 5.0% at > 20 μm, and to 3.0% for the whole soil, and the value of ε_{shi} has changed from 60 for the two finest sizes to 78 for the three coarsest.

We obtained the best results for the two finest grain sizes (**Figures 25a, b**), for which the match appears to extend to about 5 GHz, and rms errors between model and data in ε' are less than 3% (< 2 μm) and 2% (2–10 μm) below 1 GHz. The σ values we matched to the measured data are close to the values determined for the real data. They appear nearly correct because they provide a good match for ε''. At lesser water contents we might expect more anomalous dependency upon frequency. Therefore, σ appears to be the main control on ε'' as frequency decreases. For the two coarser grain sizes and for the whole soil, ε' rises in the models but does not provide as good a match at the very lowest frequencies because it projects to higher values as frequency decreases (**Figures 25c, d, e**). The behavior of the experimental data for the two coarser sizes at low frequencies appears similar to that of the illite in **Figure 24** and so it appears that the illite and probably the kaolinite influenced ε^* for these sizes as well. **Tables 3 or 4** show that the percentage of at least one of these minerals is relatively greater than that of the smectite for the two coarsest sizes.

The major difficulty was in providing a match for frequencies above about 2–4 GHz. The match appears good for the < 2 μm and > 20 μm grain sizes, but there are severe mismatches for the others in either ε', ε'' or both. The most serious difficulty is that the values of ε' fall off faster than the modeled behavior. Error calibrations with water show that this is to be expected. Alternatively, attempts to match this falloff by either placing f_{rhi} below 20 GHz or incorporating a second relaxation in the 1–3 GHz range (as done by Hoekstra and Delaney (1974) at far lower water contents) resulted in unacceptably low values of ε' in the vicinity of 1 GHz, and unacceptably high values of ε''. The key is that the high values of ε' near 1 GHz can be maintained only by using ε_{shi} values of 60–78, although the ε_{shi} = 60 for the finer sizes suggest that some water adsorbed on mineral surfaces affected the high frequency behavior. These values require mainly free water relaxation, and therefore, values of f_{rhi} near or greater than 10 GHz.

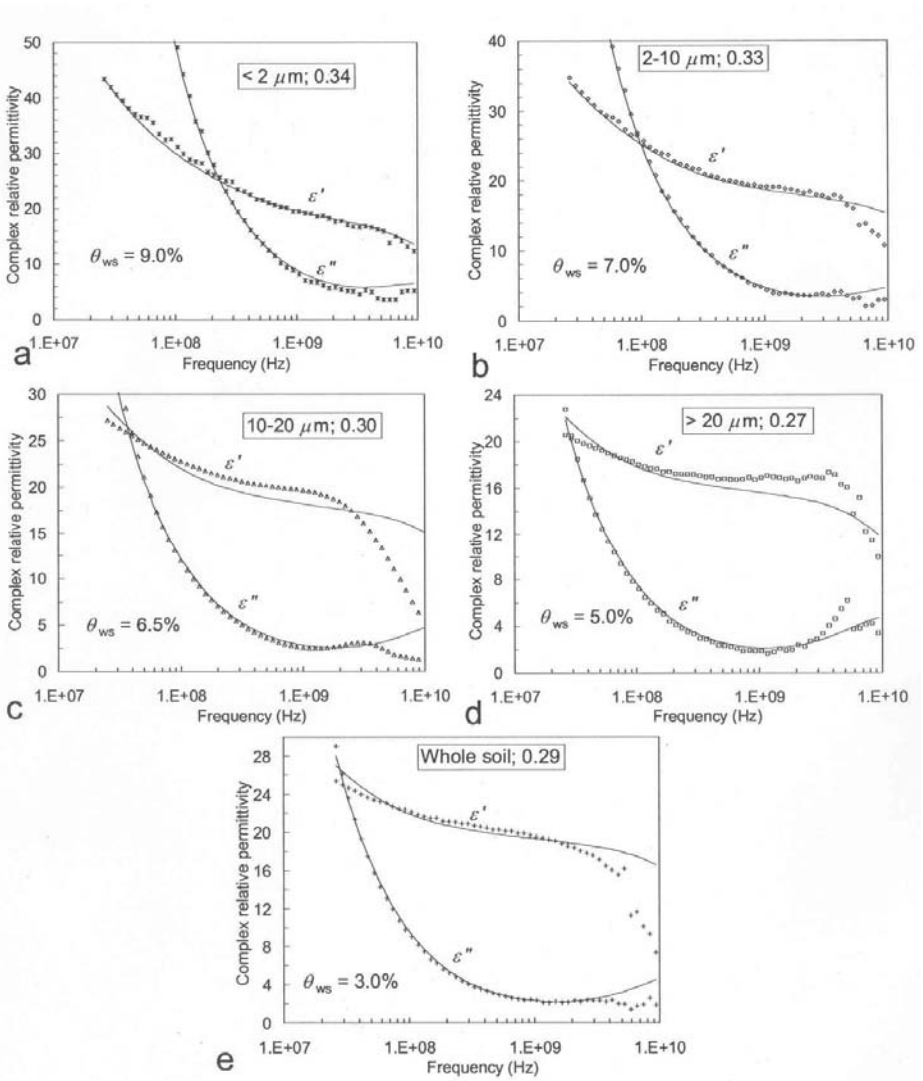

Figure 25. Measured complex permittivity (data points) for the < 2 μm (a), 2–10 μm (b), 10–20 μm (c), > 20 μm (d) and whole soil (e), and matching models (solid lines) for ε' and ε''. The text at top in each figure gives the grain size followed by the volumetric water content as a fraction. The text at bottom gives the smectite-affected volumetric water content (θ_{ws}) in percent. The model parameters for the two Debye relaxations and σ values are given in **Table 5**.

Size (μm)	ε_{slo}	f_{rlo} (kHz)	α_{lo}	ε_{shi}	f_{rhi} (GHz)	ε_{∞}	α_{hi}	σ (S m^{-1})	θ_{ws} (%)
Whole	12000	5	0.72	78	20	5.6	0.0	0.035	3.0
> 20	10000	5	0.62	78	12	5.6	0.0	0.033	5.0
10–20	12000	5	0.62	78	20	5.6	0.0	0.052	6.5
2–10	12000	10	0.62	60	20	5.6	0.0	0.120	7.0
< 2	12000	10	0.62	60	12	5.6	0.0	0.330	9.0

Table 5. Modeling parameters used in Figure 25.

The high water content, which is able to be totally adsorbed by the smectite, should then cause any relaxation centered near 1–3 GHz to be minor, which is consistent with the small variations in ε'' in this frequency range. Consequently, we think that the mismatches near the highest frequencies are caused by either errors generated by processing, the granular nature of the samples, or by a relaxation process far more complicated than just two Debye relaxations.

Volumetric water content

An alternative explanation for the increase in ε' with decreasing grain size is the slightly increasing values of θ_W with grain size (whole soil not included; the effect of water and density on whole soil vs. > 20 μm size is discussed below). However, there are three qualitative arguments based on Figure 3a against θ_W being an important factor. The first is that the increase of ε' with decreasing frequency to values far above what would be predicted by any air, free water and mineral mixing model that considers only water content is characteristic of wet clay minerals. Secondly, although θ_W increases by 3% from the > 20 μm to the 10–20 μm range, and then by 3% from the 10–20 μm to the 2–10 μm range while ε' increases by 32%, and then 28%, respectively by 25 MHz, θ_W increases by only 1% from the 2–10 μm range to the < 2 μm range yet ε' still increases strongly by 25%. In other words, ε' progressively increases strongly through the grain size ranges but volumetric water content does not. Thirdly, in the crossover region from 500 MHz to 2 GHz, the three finest grain sizes have almost the same ε' and θ_W values, but the modeling suggests that the equality in ε' is made possible by a suppression of ε_{shi} for the two finer fractions. The coarsest fraction (> 20μm) has a close ε' in this frequency range, but significantly less total clay mineral content, and the least value of θ_W.

In contrast, the plots for ε'' in **Figure 21a** exhibit clear separation below 2 GHz. This is characteristic of the influence of σ, which is determined by ion mobility and concentration. In each fraction the mobility is enhanced by decreasing grain size and water content, and the ionic concentration is enhanced by increasing clay content.

Mineralogy

The important question concerns the competing roles of the three clay minerals at all grain sizes. The modeling evidence for smectite dominance appears consistent for the < 2 and 2–10 μm fractions but is somewhat conflicting for the 10–20 and > 20 μm fractions. On one hand, the values of ε_{shi} = 60 for the two finer sizes and 78 for the coarser sizes are close to the free water value, which is consistent with the frequency relaxations reported by Sposito and Prost (1982) and Ishida et al. (2000), both of which imply that smectite water exists in a nearly free state within galleries. This suggests that smectite dominated at all fractions. If the water were primarily adsorbed onto mineral surfaces then the value of ε_{shi} would be far less, mainly due to its high viscosity (Or and Wraith, 1999; p. 374). On the other hand, the modeled behavior of ε'

near the lowest frequency for the two coarser fractions does not fit the smectite picture as well as it does for the finer sizes. The smectite content is too low for the > 20 μm fraction for this to be of concern. Although we find $\varepsilon_{shi} = 78$ for this fraction also, the slight mismatch at the lowest frequencies suggest that the illite and kaolinite played a significant role at these sizes. Given the high water contents and the lower specific surface areas of these minerals, most water not adsorbed into the smectite galleries would have primarily existed in a free state within the soil.

All the water in the two finest fractions could have been taken up by the smectite because water within montmorillonite can reach several times its weight if the interlayer cation is mainly sodium (Calvet, 1975; Meunier, 2004). For example, the < 2 μm fraction had $\theta_w = 0.34$, and modeling determined that $\theta_{ws} = 0.09$. Based on the mineral percentages for < 2 μm size in **Table 3,** the dry density of 1.21 g cm^{-3}, $\theta_a = 0.56$ and $\theta_{ws} = 0.09$, the smectite weight in 1 cm^3 of the < 2 μm size would be 0.105 grams while the total water content in 1 cm^3 is 0.34 gr, which is then well within it adsorption capacity. Montmorillonite also has a much greater attraction for water than does kaolinite or illite, as measured by its adsorption isotherm (Meunier, 2004) or demonstrated with mixtures of kaolinite and smectite (Likos and Lu, 2002). Consequently, this retention ability and our finding that $\theta_{ws} < \theta_w$ suggest that only a portion of the water within the smectite was affected by the low-frequency dispersion.

Phase velocity and attenuation rates

The low-frequency relaxation affects ε^* in the GPR bandwidth through the use of α, which may be a proxy for mid-frequency relaxations. **Table 6** demonstrates its effect with a comparison between measured (v_{phmeas}) and modeled (v_{phmod}) phase velocities of propagation at 100 MHz and 1 GHz. At 1 GHz we might expect v_{ph} to be controlled by the free, or nearly free value of ε_{shi}. The complex CRIM approach combines all real and imaginary parts of the refractive indices so that it is not possible to extract their individual contributions to v^*_{phmod} from the complex formulation in equation (5). We therefore also computed v'_{phmod} from the real part version (equation (7)) in which we used $\varepsilon' = \varepsilon_{shi} = 78$ (or 60, according to grain sizes shown in Figure 7) for the water component. The agreement between v_{phmeas} and v^*_{phmod} at both frequencies verifies what is obvious in the plots of **Figure 25**. However, the value of v'_{phmod} is significantly too large at 1000 MHz. Consequently, the comparison suggests that the combination of the smectite low-frequency relaxation and α lowers phase velocity even at 1 GHz.

Grain size	v_{phmeas} (cm/ns)	v^*_{phmod}	v'_{phmod}	1-way Att. (dBm^{-1})
Whole	6.3–**6.8**	6.3–**6.8**	**7.4**	18–**50**
> 20 μm	6.9–**7.3**	7.0–**7.6**	**8.0**	16–**43**
10–20 μm	6.1–**6.7**	6.2–**7.0**	**7.5**	22–**53**
2–10 μm	5.4–**6.8**	5.5–**6.9**	**7.7**	42–**95**
< 2 μm	4.4–**6.7**	4.6–**6.6**	**7.8**	70–**171**

Table 6. The ranges for the phase velocity, v_{phmeas}, calculated from our data, the phase velocity determined by the complex CRIM model, v^*_{phmod}, and the phase velocity, v'_{phmod}, determined by the CRIM model of equation (7), which uses only the real parts and the value of ε_{shi} for all water. The velocities are given in cm ns^{-1}. The last column gives the one-way attenuation rate at 100 and 1000 (bold type) MHz.

Grain size	v_{phmeas} (cm/ns)	1-way Att. (dBm^{-1})
Whole	6.2–**6.3**	16.7–**18.4**
> 20 μm	6.8–**7.0**	14.6–**16.1**
10–20 μm	6.0–**6.2**	20.8–**23.1**
2–10 μm	5.2–**5.5**	38.8–**44.8**
< 2 μm	4.3–**4.7**	62.7–**73.3**

Table 7. The ranges for v_{phmeas} and for the one-way attenuation rate for a pulse bandwidth of 83−118 (bold type) MHz.

In assessing GPR performance it is necessary to know if a distorted waveform resulted from changes in v_{ph}, β, or both across the pulse bandwidth. The small differences in v_{phmeas} between 100 MHz and 1 GHz at the larger grain sizes and for the whole soil (**Table 6**) might suggest that a GPR pulse centered near 100 MHz will show little distortion after 1–2 m of round-trip propagation within medium to coarse wet silt at these water contents or less. However, the differences in β seen in **Table 6** are significant so we look at values for a common case. A typical GPR pulse has a 3-dB bandwidth of 35% (Arcone et al, 2003), which places 88% of the energy for a 100-MHz pulse between about 83 and 118 MHz. **Table 7** shows that v_{phmeas} is almost constant across this bandwidth but that β is not for the three finest grain sizes; at 10–20 μm a 1-m round trip will find an attenuation difference of 4.6 dB and the round-trip rate difference is at least 3 dB m^{-1} for the coarser > 20 μm size and for the whole soil. Consequently, a 100-MHz pulse may not undergo significant dispersion, but will likely undergo distortion caused by a significant downshift in its dominant frequency should it survive a 2- to 4-m round-trip within wet silt.

Iron oxides

The removal of iron oxides from our dielectric samples was standard procedure for facilitating grain size separation, but it raises the question of whether or not this was fair treatment because water retention in iron oxides can cause GPR reflections (Van Dam et al., 2002). Although the characteristic brown color of Fairbanks silt indicates oxide coating, iron oxides were not removed from our XRD samples and were not detected. However, they could have been in the amorphous material. We also did not remove iron oxides from the sample of whole soil used for dielectric measurements.

We address this question with the data in **Figure 21a**, which shows that ε' for the whole soil nearly parallels that of the > 20 μm fraction from 25 MHz to 1 GHz. The whole soil runs only about 12% (19.5 at 1 GHz) to 24% (25.4 at 25 MHz) higher than does the > 20 μm fraction (16.9 and 20.6 at 1 GHz and 25 MHz, respectively), which constitutes 84% of the soil. The whole soil had a total clay mineral fraction of 17% (percent fraction weights in **Table 1** multiplied by percent clay mineral weights in **Table 3**) while the >20 μm oxide-treated fraction had 16%. Given this near equality, we use the real part version of the CRIM formula in equation (7) as an approximate check (regardless of clay content) to find if this 12% difference near 1 GHz could be accounted for by the 16% greater density, 23% less porosity and 2% greater θ_w within the whole soil. These factors would theoretically raise ε' by 15% (from 14.2 to 16.3) so we preclude any significant effect of iron oxides. In addition, the strong adsorption of the clay minerals could have removed most of the water from any oxides.

Tie-in to JEP and Squam Lake

Obtaining meaningful samples for dielectric testing from the JEP bottom was not feasible. Many samples were acquired by Shaw Environmental but they were supersaturated and the content may have had metallic fragments. Consequently we sampled the bottom of Squaw Cove. TM company of Wildomar, California supplied the mineralogy and grain size data in Figure 26. Chlorite, illite or mica, and kaolinite were less than 5% by weight each. Quartz was approximately 75% by weight and feldspar was 15%. The lack of any smectite such as montmorillonite is conspicuous and likely to have allowed the penetration of the GPR signals.

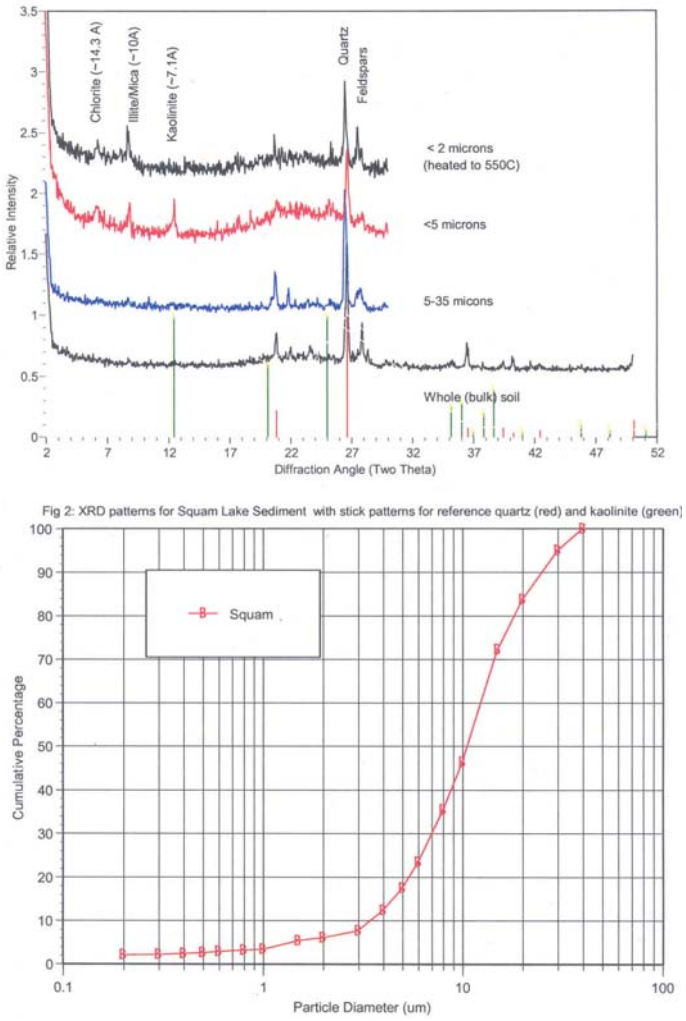

Figure 26. XRD determined mineral spectra (top) and grain size analysis (bottom) for a bottom sample from Squaw Cove on Squam Lake.

Dielectric testing of these samples has been difficult. We have difficulty reducing the water content. Our first try gave a volumetric water content of 78%, which is unrealistically high and should give a real permittivity value of between 50-60. The measured value was ~50, which held from 100 MHz to 1 GHz. However, the one way attenuation rate was very high at 40-50 dB/m. Therefore, the mineral analysis is consistent with the field observations but not the

permittivity measurements. The problem may lie in the super saturated values of volumetric water content and we are presently trying to lower these values to amore realistic 45-50%.

ACCOMPLISHMENTS: FALSE TARGETS AND RESONANCES

Overview

Prior to the JEP study, we conducted surveys on many lakes situated on formerly used bombing and artillery ranges in Alaska in search of subbottom ordnance. A few targets were found but were characterized by resonance phenomena rather than the large and prominent diffractions seen beneath JEP. Only by numerical modeling could we be sure that these targets were likely not to be UXO. No such resonances have yet to be found within JEP although the conditions necessary (large metal objects near interfaces of strong dielectric contrast) are very much present. Given that our JEP survey consisted of only 30 lines, many more profiles might reveal such resonances. Here we briefly review some of the results of this study, which is now published in the journal *Geophysics* (Arcone et al, 2006).

Resonances infrequently occur in ground-penetrating radar (GPR) reflection profiles and are generally associated with metal objects just beneath the surface. By resonance we mean events that are brief in distance, extensive in time, and usually contain multiple, vertically aligned and abbreviated diffractions at a nearly fixed frequency. Each diffraction must originate at the same depth because they do not appear to widen with increasing time. More frequently, geometrically simple targets usually provide single wavelet diffractions in response to GPR signals, with strength depending on pulse center frequency and polarization relative to the target axis. Such targets may be metal pipes, rebars and military ordnance. Resonances and diffractions may be the main options used to identify target characteristics because the wavelengths of GPR signals are generally too long to allow the target geometry to be outlined by reflection horizons. In this paper we discuss frequency characteristics of resonances within field data that are caused by the interaction of a target with subsurface stratification.

Resonance from targets may have several causes, aside from noise such as antenna mismatch. A first cause is target surface oscillations, especially for metal wires or cylinders, whereby induced currents will reverberate along the target surface at a frequency determined by the target length. These resonances are complex so that they experience large attenuation when the target diameter compares with a significant fraction of a wavelength; large cylinders usually do not support surface resonances. A second cause is target internal oscillations, which occur within a dielectric structure such as a hollow or water-filled plastic or concrete pipe. A strong contrast in relative dielectric permittivity, ε_r, between the target materials and the ground allows a small leakage of the resonance to the surface while the reverberation persists. The third type of resonance is similar to intralayer multiple reflections and occurs between the target and an interface across which exists a strong dielectric contrast. The most common situation is a utility just below the ground surface. Here we examine cases where we believe this third type of resonance exists, but at depth and not just below the surface.

Interfaces between materials of strong dielectric contrast are provided by the stratigraphy beneath lakes (the subbottom) because ε_r of water is generally much higher than that of any sediment or rock, whether saturated or not. High permittivity contrasts at depth will also occur beneath shallow lakes that freeze completely to (or even beneath) the water bottom because of the low ε_r of ice and the higher ε_r of either frozen or unfrozen silty or clay-rich sediments. This stratigraphic context is common in late winter within the many shallow lakes (< 2 m depth) that comprise more than 20% of the approximately 400 km^2 of artillery and bombing ranges on Forts Wainwright and Greely in interior Alaska. Consequently, these lakes are likely to supply another strong ingredient for resonance, that of metal targets.

We recorded GPR profiles in March 2005 when the lakes were completely frozen. The profiles feature many diffractions, a few resonances, and irregular horizons that define the lake bottom, the freeze/thaw boundary and sedimentary stratification. These lakes exist on frozen and unfrozen glacial outwash deposits, so boulders or localized deposits of clay or silt should be the source of most of the diffractions. In view of the fact that natural resonances are suppressed in typical, cylindrical shaped ordnance, we formed the hypothesis that the resonances were caused by metal targets near the major ice and freeze/thaw interfaces; a dielectric target would permit too much transmission loss upon successive reflections to sustain resonance. However, we needed a test to relate these low frequencies to layer structure because the resonances are typically characterized by frequencies well below the pulse bandwidth.

Based on our resonance hypothesis, our objective was to determine if the transit times between the onset of these resonances and those of the overlying interface reflections correspond with spectral peaks predicted by quarter-wave resonance theory for layers. This means that a spectral peak should occur at a frequency that equals the inverse of twice the transit time within the layer. If such frequencies exist, then 1) the resonances are caused by metal targets, or else an entire profile would be filled with resonance between the interfaces and the natural inhomogeneities; and 2) the target might be of wavelength size or more, so that resonance within or on the target itself is unlikely. The profiles we analyzed were recorded with GPR pulses centered near 280 MHz. The associated bandwidth has provided depth resolution of an ice sheet 1 m thick or less, and penetration of about 2−3 m in unfrozen and saturated silt. After removing the constant background scatter, we applied a low-pass frequency filter to reveal and locate the position of the resonances. We then were able to identify the origin of our resonant diffractions within the unfiltered profiles and to measure their transit time within the layer in which they existed. We use numeric and analytic models to help interpret the nature of the targets because excavation was prohibited.

Site

We recorded 400 MHz GPR profiles during March, 2005 on Longhorn and Dallas Lakes, located in the Texas Range, one of many artillery ranges located on greater Fort Wainwright, near Delta Junction, Alaska (**Figure 27**). These ranges are situated on at least 60 m of outwash sands and gravels generally known as the Donnelly moraine. The Texas Range has not been active since 1980. The lakes appear to have formed in pluvial and spring-fed depressions of a few hundred meters maximum dimension, sometimes surrounded by morainal ridges. Therefore, they do not have the typical deep lacustrine deposits of well-stratified silts and clays, but rather a rocky bottom with central sections of loess that have a thickness of about 1 m or less. Some of the northerly shorelines are mostly sandy or covered with small boulders, and so we presume this is the deeper horizon we see in our profiles. Southerly shorelines often contain tussocks beneath which the sedimentation generally has a loess cover. Ice-poor permafrost is sporadic throughout the area, and it is doubtful that any permafrost exists beneath the lakes. Longhorn Lake had at least 12 craters along its southern shore, each of about 2−3 m in the largest dimension (Figure 26).

We towed our antenna across the ice (**Figure 27**) behind a motorized vehicle and recorded kinematic GPS data simultaneously. The pulse center frequency was actually closer to 300 MHz due to antenna impedance loading. The antenna bandwidth however, was sufficient to induce resonances in what we surmised as metal targets.

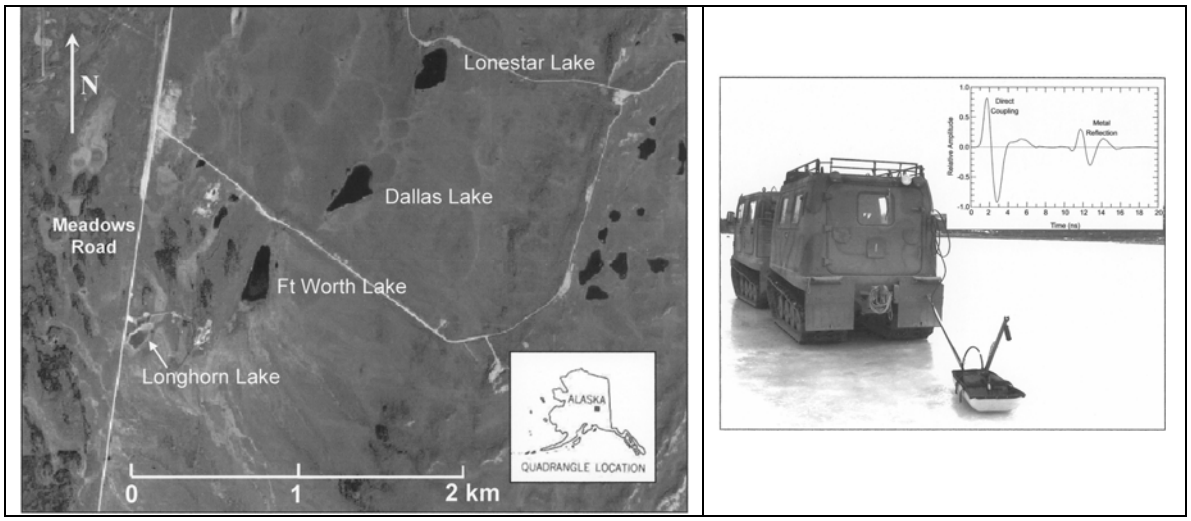

Figure 27. lakes surveyed on artillery ranges in Alaska (right), and survey procedure with 400-MHz antenna being towed behind a Hagglunds B111. Inset shows the transmitted waveform.

Resonance theory

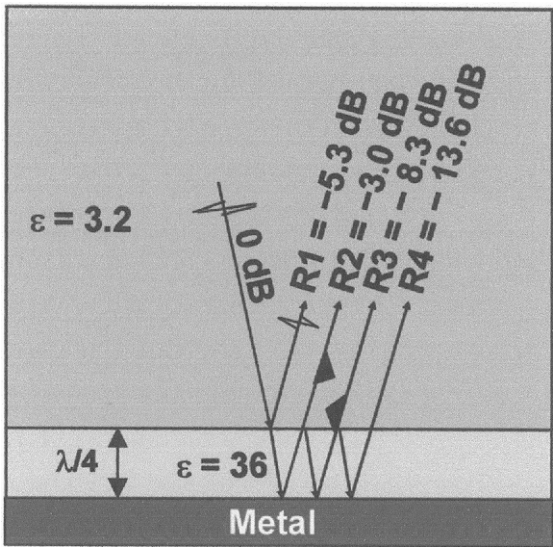

Figure 28. A ray diagram of quarter-wave resonance in a dielectric layer above a perfectly conducting substrate. The resonance is depicted by black filled triangles because its frequency is usually lower than the pulse bandwidth and so will modulate the reflection sequence.

We base our interpretations upon quarter wave matching theory. The quarter-wave requirement for reverberation is based on the same principles of the well known, quarter-wave matching criterion, but without other requirements upon the permittivity ratios for the layer materials. A quarter-wave matching layer (often used as an optical coating for lenses) is used to achieve near perfect transmission from one medium into another for monochromatic radiation. The layer causes its front reflection to be π out of phase (destructively interfere) with the reflection from its back. A π phase change occurs for any normally incident reflection from an

interface between lower permittivity material (in which resides the incident wave) above and higher below, or from metal. However, the key point is that the first back reflection does not totally cancel the front reflection; the successive intralayer multiple reflections must all add constructively when they leave the layer to help in the cancellation process and the ε_r of the matching layer must be the geometric mean of ε_r for the two layers surrounding it. The resonances we discuss exploit this constructive interference of the successive intralayer multiples; the ε_r of the layer only helps to determine the transit time. The schematic in **Figure 28** illustrates the phenomenon. The reflected waveform from the top of the layer (R1) is that of the incident pulse, but has undergone a π shift in phase and so the polarity sequence of its successive half cycles is reversed. The phase polarity sequence of much stronger, first reflection from the bottom (R2) will be the same as that of R1. At the correct frequency, the successive reflections (R3, R4, etc.) are multiples of 2π out of phase with R2 and so a resonance is constructed. There is no phase shift for a wave passing through an interface, nor for a wave reflecting from the underside of an interface if the material above, such as ice, has a lower ε_r than does the material of the resonating layer.

The resonant frequency f_r, in the metal target, quarter-wave case is given by

$$f_r = c/4dn \,, \qquad (12)$$

where the layer refractive index $n = \sqrt{\varepsilon_r}$. The combination of d and n directly determines the transit time t for round-trip propagation within the layer such that $t = 2dn/c$. For the quarter-wave case then, $f_r = 1/2t$. The resonant frequency is not necessarily the dominant frequency of the pulse because the pulse is broadband. Therefore, the resonant frequency can range from far below to near the pulse center frequency and can occur either as a modulation or as the dominant frequency of the total reflection sequence. The schematic illustrates the case where the frequency of the resonance is well below the pulse bandwidth and so it is represented as a wave of longer duration. For a metal target beneath a layer of frozen silt ($\varepsilon_r = 9$) that underlies ice, plane wave theory predicts that the first, top-of-the-layer reflection (R1) loses 11.6 dB of strength from the incident wave. The first reflection from the bottom of the layer (R2) then loses only 0.6 dB because it has undergone only interfacial transmission losses. Each successive intralayer multiple then loses 11.6 dB of electric field amplitude per reflection. If the resonant layer were unfrozen ($\varepsilon_r \sim 36$) under frozen silt, the successive multiples would eventually lose only 5.3 dB per multiple reflection and provide a much stronger and more sustained resonance (**Figure 28**). We do not account for intralayer attenuation because our resonant layers are so thin, but several more dB could be lost after 5 or more reverberations.

The layers discussed below and in which resonance occurs all have values of ε_r greater than that of the layer above them. If the layer is ice with metal on the bottom, the layer above is air ($\varepsilon_r = 1$). If the layer is frozen silt ($\varepsilon_r \sim 9$ or as high as 30 for marginally frozen silts or clays), the layer above is ice, and if it is unfrozen silt ($\varepsilon_r \sim 36$), the layer above may be ice or frozen silt.

Resonance sample results: Longhorn Lake Transect 26

The profile of transect 26 (**Figure 29a**) clearly reveals horizons 1 (base of the ice) and 2 (frozen-unfrozen interface). The phase structure of horizon 1 varies from + − + to − + −, but that of horizon 2 is consistently + − +. A brief horizon at the lower right has the characteristic phase structure (− + −) for an interface between a high permittivity material over a lower one and so may be horizon 3. There are several disturbances near 71 m, and it is not clear if they are closely spaced diffractions or resonances. Near 78 m a series of concentric hyperbolas of the same shape originate below horizon 2. Low-pass filtering (**Figure 29b**) reveals that the disturbance near 71 m is a resonance while the resonance near 78 m has been degraded. In the vicinity of the

resonances, the ice bottom horizon 1 starts at 6.6 ns (0.56 m of ice) and the start of the freeze/thaw horizon 2 varies between about 16−17 ns. Given the round-trip time difference of 10 ns and an $\varepsilon_r = 9$ for ice-rich material at a temperature of about ~ −7°C, the freeze/thaw interface is then ~0.50 m below the base of the ice. If the silt was ~ –1°C, then ε_r could be close to 30 and the freeze/thaw interface at ~0.27 m below the ice bottom.

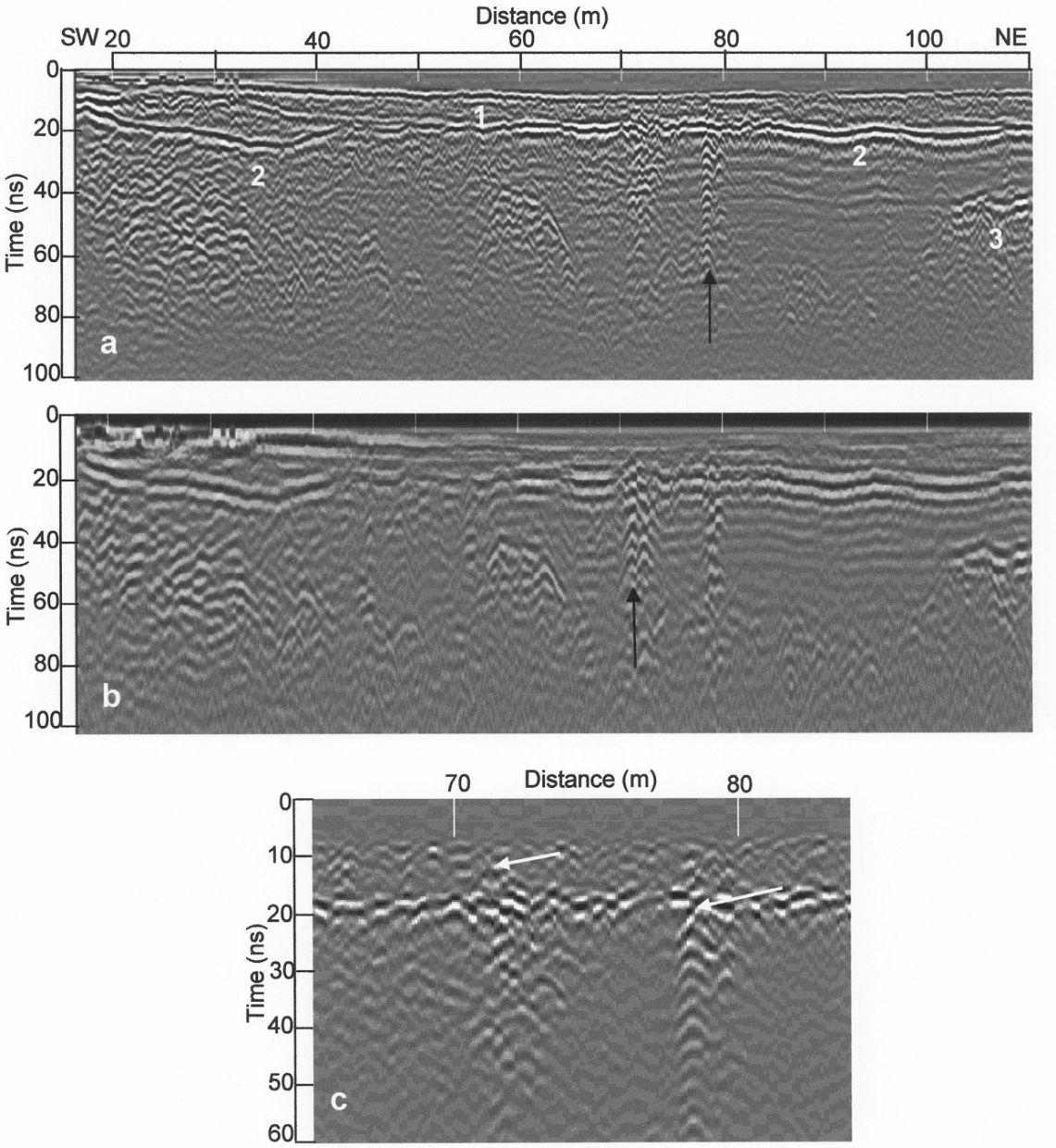

Figure 29. Profile of a segment of transect 26 on Longhorn Lake (a), same profile after the 100-MHz low-pass filtering (b), and same profile but with a 35-trace high-pass horizontal filter applied and displayed in a linear intensity format (c). The arrows in (c) indicate the start of the events that contain resonances. The unfiltered profiles (a, c) show almost no evidence of resonance at 71.1 m.

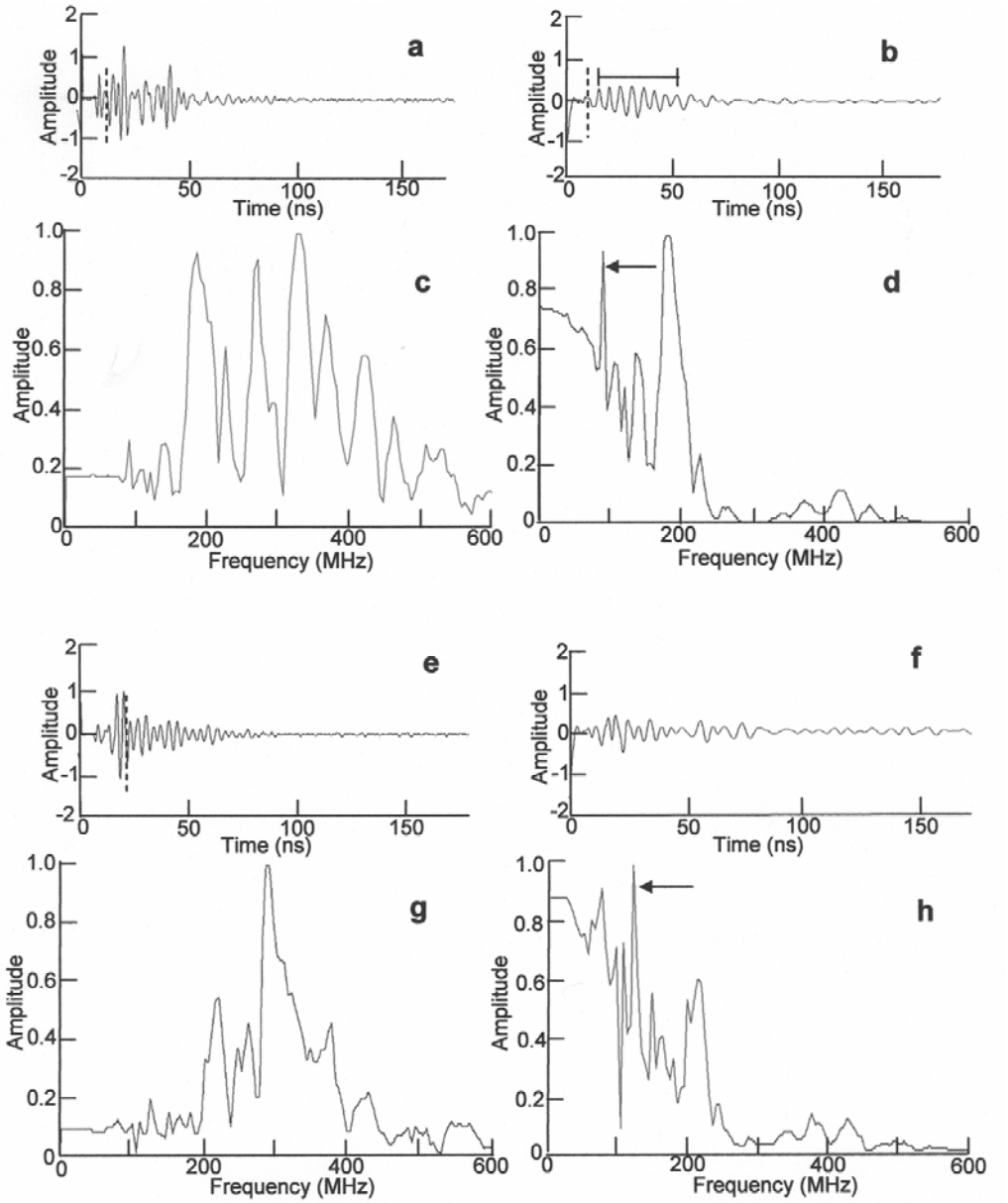

Figure 30. The trace at 71.1 m distance from the profile in **Figure 29** before (a) and after low-pass (100 MHz) filtering (b); their respective normalized spectra (c, d); and the trace at 78.5 m distance before (e) and after (f) filtering; and their respective normalized spectra (g, h). The dashed lines indicate the onset of resonance in the unfiltered traces, and the arrows indicate the quarter-wave peaks in the spectrum. The horizontal line with end bars in (b) indicates resonance duration. The amplitude scales are relative.

The 100 MHz filtered profile (**Figure 29b**) shows that the resonance is centered at 71.1 m. The enlargement of a horizontally filtered version of the profile (**Figure 29c**) shows that it starts at 12.0 ns, which places it above the freeze/thaw horizon 2 and in the frozen silt. The 12.0 ns transit time to the target gives a transit time of 5.4 ns in the frozen silt, which gives a quarter-wave f_τ = 93 MHz. Our timing accuracy places this frequency between 86 and 100 MHz. The filtered trace (**Figure 30b**) shows a spectral peak at 90 MHz (**Figure 30d**). However, the resonance is dominated by seven cycles lasting 37 ns (barred horizontal line), which provides the

186 MHz dominant frequency in the filtered profile and spectrum. Therefore, our 93 MHz spectral peak is a weak modulation. For $\varepsilon_r = 9$, 5.4 ns gives a thickness above the target of 0.27 m. If we increase ε_r to 30, then the thickness decreases to 0.15 m, and, of course, the theoretical resonant frequency is still 93 MHz.

A second resonance is centered at 78.5 m (**Figures 29a, 30e**). Its period of 3.6 ns gives a dominant frequency of 278 MHz, as measured from the profile. At this distance horizon 2 begins at 16.8 ns. Removal of horizon 2 with a 21-trace horizontal filter (**Figure 29c**) shows that the diffractions begin at 20.8 ns, which gives a transit time of 4 ns within the unfrozen silt below the freeze/thaw interface. This time predicts a resonant quarter-wave frequency of 125 MHz and a layer thickness above the target of ~ 0.10 m for an estimated $\varepsilon_r = 36$ for an unfrozen saturated silt. Given our timing accuracy, this predicted value could be between 114 and 139 MHz. The unfiltered spectrum in **Figure 30g** shows that the dominant resonance in the unfiltered profile is centered near the pulse center frequency at 280 MHz. The filtered profile (**Figures 29b, 30f**) has a dominant frequency of 216 MHz, and its spectrum (**Figure 30h**) has a strong peak at the predicted 125 MHz resonance.

Dallas Lake: Comparative surveys

In **Figure 31** we show results from just a few of the many profiles we did of munitions that we placed beneath this frozen lake. The results confirm our conclusions that no target resonates unless it is a complex structure. The first three targets (from left to right) are bombs and artillery shells with their axes placed perpendicularly to the profile direction and parallel to the wave polarization. The fourth target is vertically oriented and is nearly to the surface. The fifth target is a complex bomb with a tailfin assembly. This is the only one that resonates, but mainly in response to the 400 MHz signal. This target also resonates at 800 MHz, but not as strongly. In all cases and for all targets, the + – + polarity of the diffracted waveform is consistent throughout the entire diffractions, which means from very steep to very wide look angles.

The first main implication of these and our other results from Dallas and Longhorn Lakes is that the metal responses beneath JEP are most likely UXO because they are consistent regardless of look angle, frequency, and relative orientation of the target with respect the incident polarization direction. The fact that the targets were beneath ice and not water is not relevant; both cases represent a dielectric over metal. The second implication is that the resonances seen in the profiles above and in other profiles (Arcone et al., 2006) are definitely not from bombs or artillery shells. Such UXO structures will not resonate given no complex structures like a tailfin assembly.

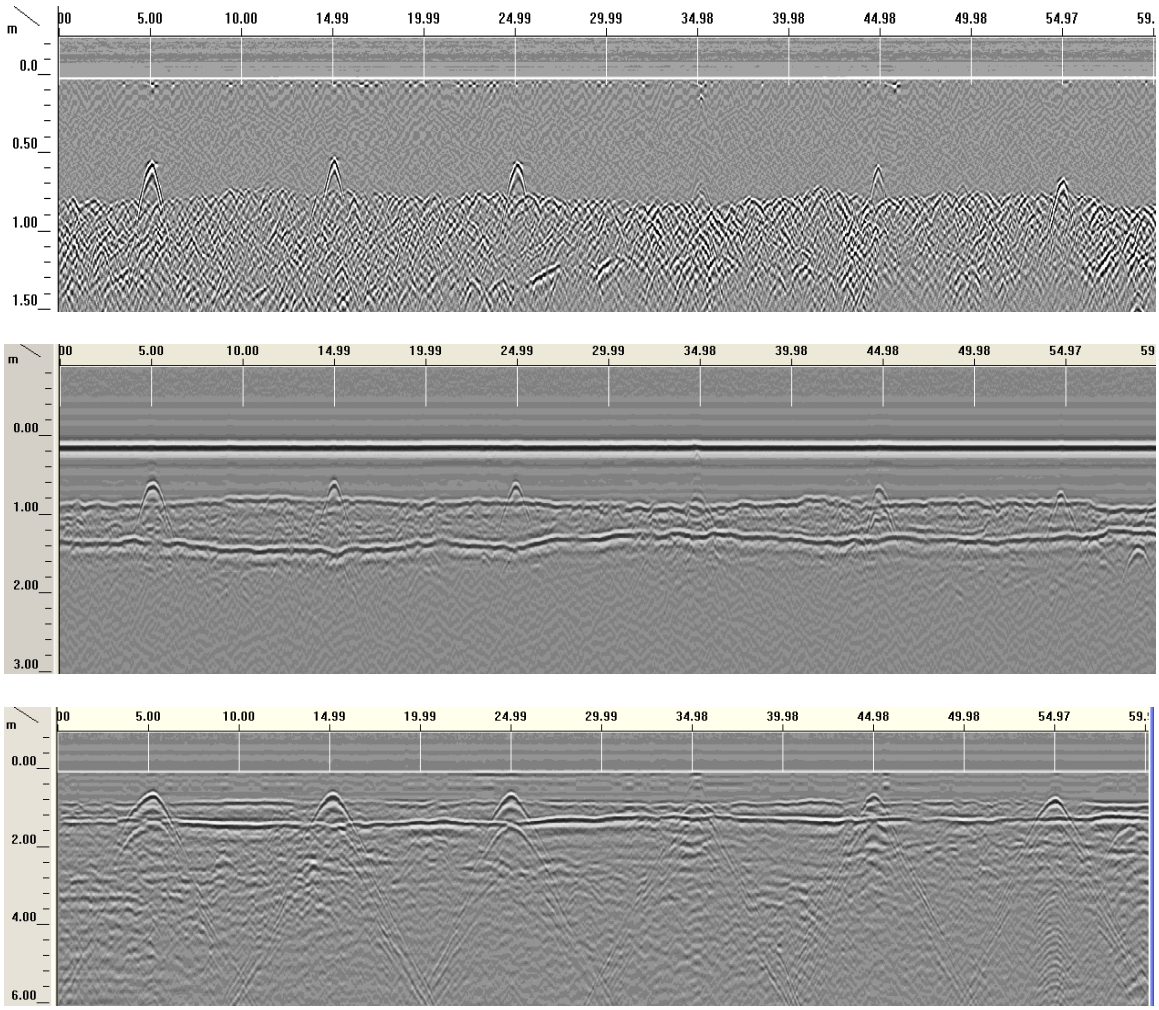

Figure 31. Profiles of the first six targets placed beneath Dallas Lake and recorded at 1500 (top), 800 (middle), and 400 MHz (bottom). From left to right, the targets are a 250 lb bomb, 155 mm artillery shell, 155 mm artillery shell, 155 mm artillery shell vertically oriented, BDU-33 practice bomb and a 3.5 inch rocket. All distances and depths are in meters.

Numerical Modeling

We performed numerical modeling in support of our resonance studies on Dallas and Longhorn Lakes. Our main result is that cylinders (UXO) do not resonate strongly in concert with the stratigraphy nor by themselves (**Figure 32**), but flat sheets do (**Figure 33**). Therefore, the resonances are a way of distinguishing false alarms. The figures illustrate how resonance develops weakly in cylinders but strongly in flat sheets beneath the model of a completely frozen lake.

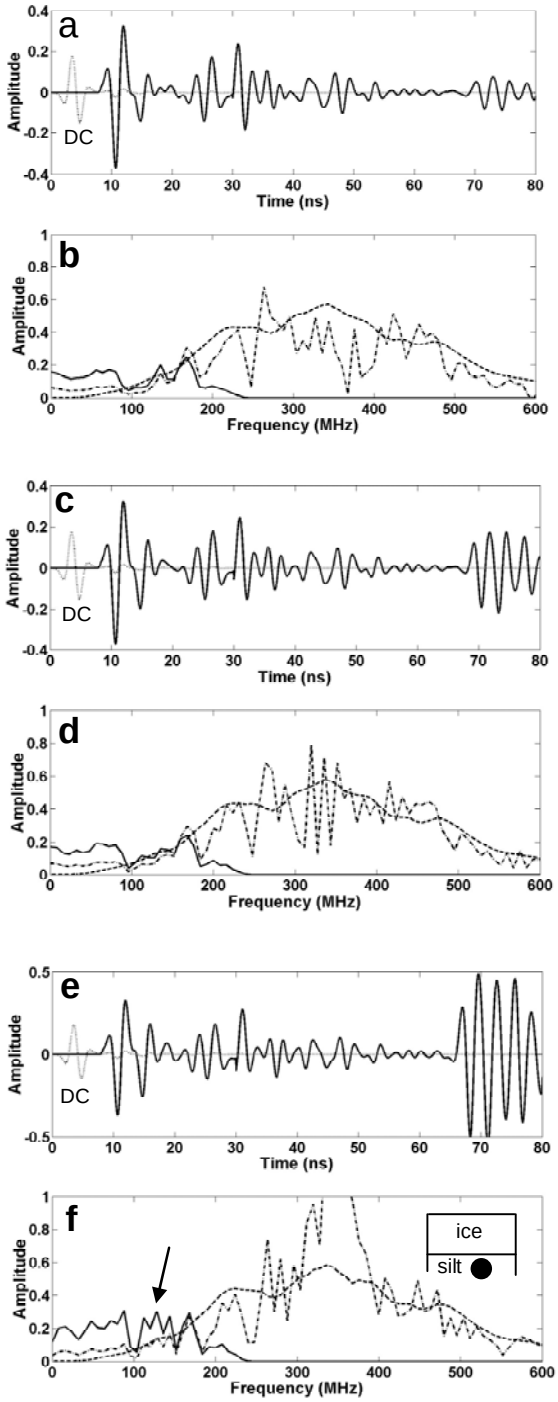

Figure 32. Traces of the response of a 280 MHz pulse to a 2-D model of ice over silt within which is a metal cylinder of 0.15 (a), 0.30 (c) and 0.60 m (e) diameters, and their respective spectra (b, d, f). The ice is 0.60 m thick and the top of the cylinder is 0.10 m beneath the ice bottom and within the silt, as shown in the insert in (f). The lighter traces are the actual responses, while the darker ones have had the direct coupling (DC) removed and range gain applied. The dashed spectra are for the raw traces, the dotted spectra for the range gained traces, and the solid spectra are for the range gained traces after application of a 100 MHz low pass filter. Only the largest cylinder shows a response near the predicted quarter wave resonance at 125 MHz (arrow).

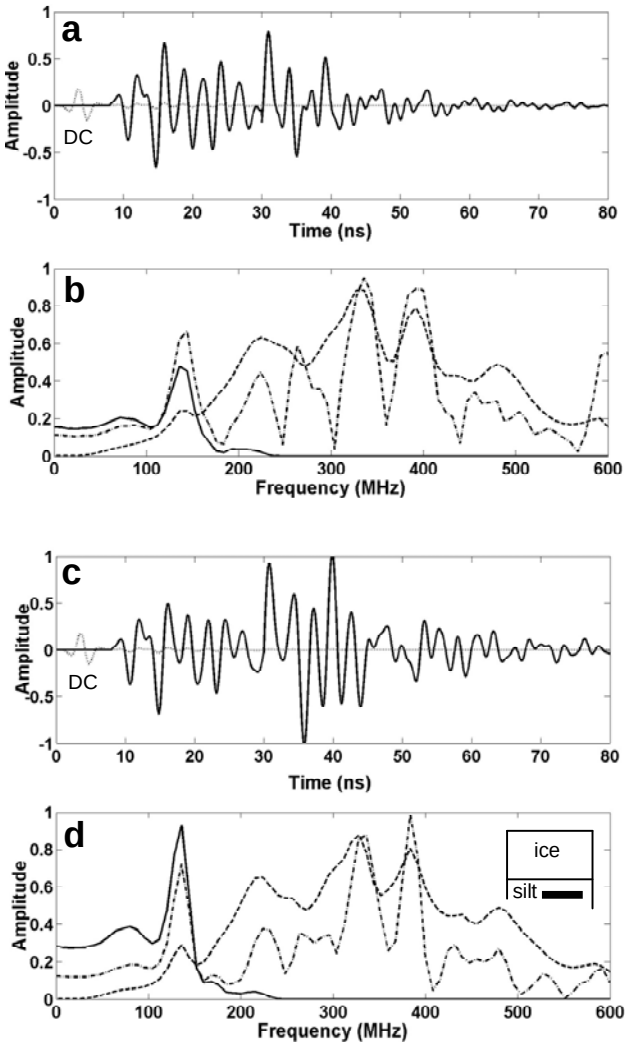

Figure 33. Traces of the response of a 280 MHz pulse to a 2-D model of ice over silt within which is a flat metal sheet of 0.5 (a), and 1.0 m (c) width, and their respective spectra (b, d,). The ice is 0.60 m thick and the top of sheet is 0.10 m beneath the ice bottom and within the silt, as shown in the insert in (d). The lighter traces are the actual responses, while the darker ones have had the direct coupling (DC) removed and range gain applied. The dashed spectra are for the actual traces, the dotted spectra for the range gained traces, and the solid spectra are for the range gained traces after a 100 MHz low pass filter was applied. Both cases show a strong response at the quarter wave resonance predicted at 125 MHz.

POTENTIAL FOR PRACTICAL IMPLEMENTATION OF GPR FOR ORDNANCE DETECTION AND CHARACTERIZATION

The potential for practical implementation of GPR for ordnance detection and characterization in lakes depends on several geologic, thermal and electromagnetic factors, each of which we discuss here.

1. **Stratification of bottom sediments:** All lake subbottoms are well stratified, almost by definition. Our results show that this is a benefit because 1) it can cause resonance between *false* targets and strata, thus allowing targets to be differentiated from false alarms; 2) it shows the penetration of the signals; and 3) it shows the possibility of burial of UXO. The stratification can host particularly strong contrasts in dielectric permittivity, such as between water and bottom sediments, and between saturated silts (typical of lake bottoms) and sandy or gravelly layers. Stratigraphy also collimates the antenna directivity and focuses it on the immediate bottom beneath an antenna. Consequently, this factor enhances detectability.

2. **Thermal stratigraphy:** The permittivity contrasts between ice and ice-rich silt, ice and saturated silt, and between frozen and unfrozen sediments are also strong and enhance detectability. Obviously then, season affects detectability.
3. **Distortion in stratigraphy caused by impact:** This phenomenon was hypothesized to exist in our proposal, and has been illustrated above. The primary distortions are draping of sediment over UXO, penetration of UXO through layers and its associated disruption, and the creation of entirely new layers consisting of UXO.
4. **Depth of penetration:** This depends primarily on water conductivity and sediment complex permittivity. In 3-5 m water depth, we have obtained up to 10 m penetration, and detected possible UXO at 2-4 m depth below the bottom surface. The conductivity was generally 0.004-0.005 S/m, which is typical of the Northeast US and also of Alaska. These values should be common throughout the US where there is no organic runoff (from farms). The sediments themselves must not contain significant of phyllosilicate clay minerals such as kaolinite, illite and in particular, montmorillonite.
5. **Practicality of frequency:** An antenna unit rated at 400 MHz, and actually radiating closer to 300 MHz, provided the best tradeoff between resolution and penetration for water depths up to 3 m. We find that a 200 MHz (actually radiates at 135 MHz) unit works exceptionally well for detecting objects beneath 3-8 m of water. These antenna units are small and practical to use.
6. **Practicality of system:** The commercial systems available all perform adequately, but there are limitations. Currently, no manufacturer is permitted to sell antennas below 200 MHz because current designs at these frequencies do not adequately shield the radiation above ground. All manufacturers sell a 400-MHz unit. The GSSI Company however, sells the SIR3000, which we used. It is battery operated, easy to use, and records data to a 1 GB flash memory. We have successfully trained field safety personnel in Antarctica in its use.
7. **Practical target characterization:** Targets are characterized and identified by their return pulse polarization, by their diffractions, by their disposition and by their evidence of penetration. Only metal targets provide the polarization we see and only UXO could have provided penetration. We also see evidence of flat lying objects, which we interpret to be UXO of approximately 2 m length.
8. **Practical target location:** The existence of an ice cover is what makes GPR practical to use on a lake. This makes for exact positioning once a target has been detected. If a lake is not frozen then positioning must rely on GPS processing for location, whether sonar, radar or any other type of method (EMI) is used. Kinematic GPS is currently accurate to about 10 cm resolution. Non differential GPS is accurate to about 2-3 meters. The narrowing of the antenna directivity in the E-plane enhances location accuracy (to beneath the antenna).
9. **Problems in Interpretation:** The first is the situation where an ice cover exists but the lake is not completely frozen. If a thin layer of water exists beneath the ice then the reverberation it causes throughout the record can mask a target. Fortunately, our resonance method may be able to retrieve a target in spite of such background reflections. A second problem is mobility on an unfrozen lake under high winds and chop. This has to be avoided. A third problem has been the proverbial needle in the haystack; how does one find a small target? However, beam-spread makes off axis detection possible. A fourth is absolute identification of a target. Consequently, this project has provided several ways to interpret data which enhance UXO interpretation.
10. **Survey safety**: There is no radiation hazard with GPR. Transmitted power is less than 8 Watts peak and milliwatts average. The antennas ride in a rubber dinghy with draw of only a few centimeters. We used a short shaft motor to drive our watercraft, so that extension into the water was less than 0.50 m.

Of far more important concern is the protection offered by the water in case of explosion, which is virtually none except for slowing of shrapnel. We find no published regulation by the Army Corps of Engineers, but considerable theoretical work has been done. The classic reference is that of Cole (1948) upon which most, if not all, subsequent work (e.g., Swisdak, 1978; Sulfredge et al., 2005) is based. The immediate danger is the bubble of TNT derivative gasses that expand from the charge, with surface velocity equal to the shock wave velocity. The maximum bubble diameter of a 1000 pound bomb, typically containing 500 pounds of explosive filler, would produce a bubble diameter of at least 26 feet, using the equations in Sulfredge et al. (2005; also, personal communication, 2008). The maximum depth of Joe English Pond is only 28 feet, and would be 22 feet after opening the dam before dredging. Thus, the gas bubble would vent to the atmosphere almost immediately upon reaching maximum expansion. This venting would preclude any secondary pressure pulses caused by bubble oscillations. Gas bubbles from smaller charges may not reach the surface but the shock wave will, as it propagates outward from the surface of the gas bubble once the bubble reaches its maximum expansion. Sulfredge estimates the initial shock wave pressure at the surface of the bubble at 26 feet to be about 5650 psi, enough to blow any large craft, such as a dredge, out of the water, and obviously, any associated equipment within the water.

Sulfredge has also communicated a real potential for sympathetic detonation, where the blast pressure sets off other UXO, given the number of duds that appear to have accumulated in the pond. Any weapons within a 30 foot radius of a 1000 pound bomb would have a significant chance of detonation.

TECHNOLOGY TRANSFER

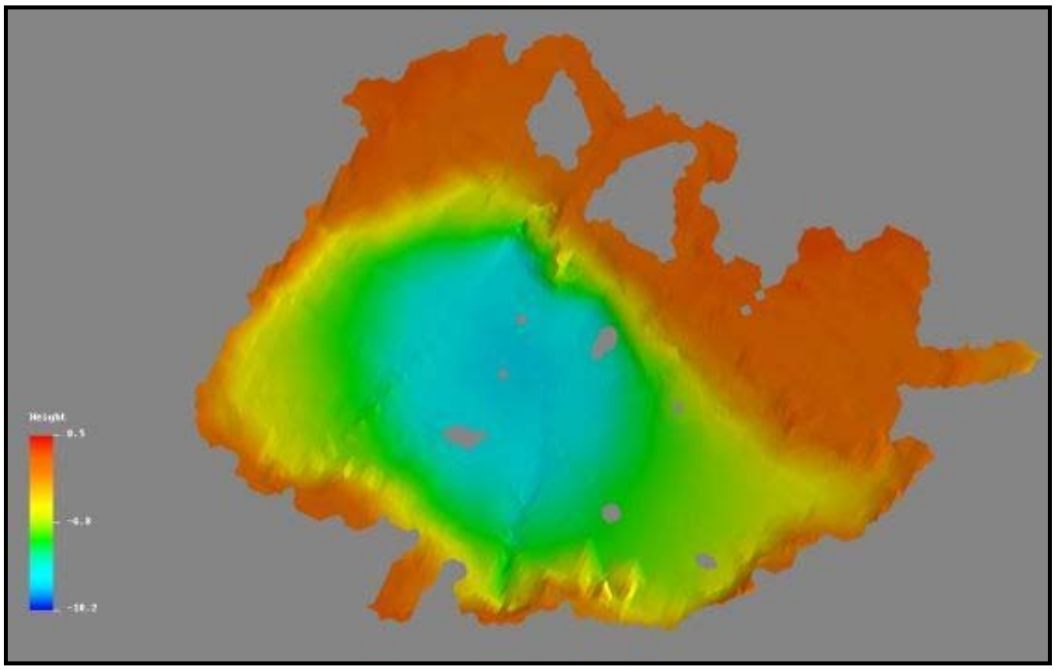

Figure 34. Bathymetry of JEP, determined from a 135 MHz GPR survey.

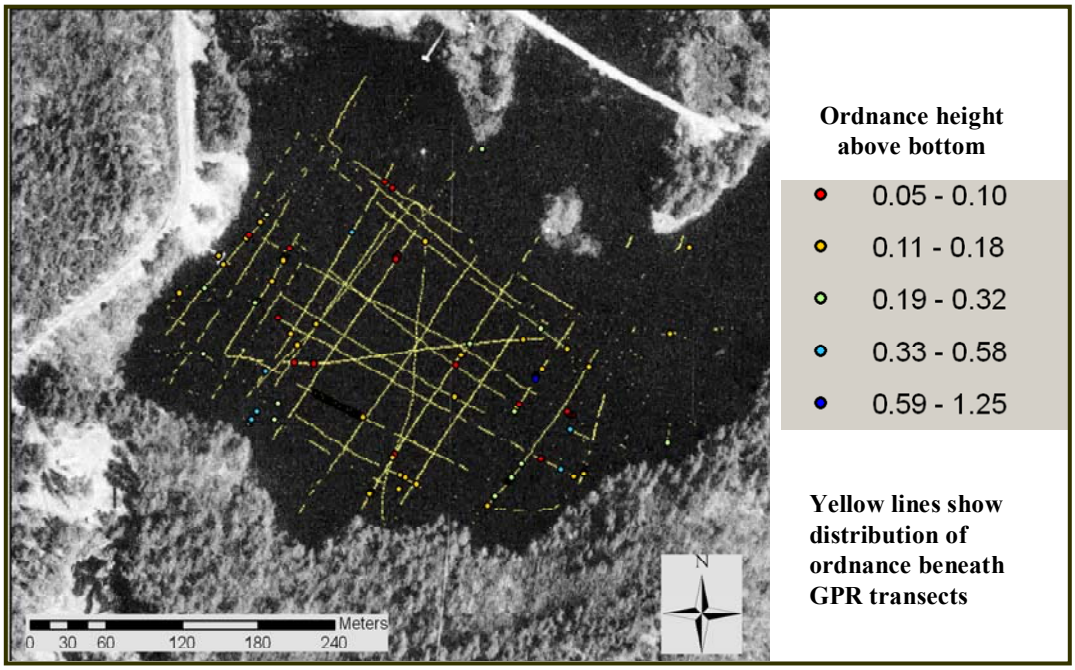

Figure 35. Distribution of suspected ordnance and height above bottom of protruding suspected ordnance in JEP.

Our most important result is the transfer of GPR/GPS technology to military organizations in need. Our success in finding metal targets on JEP has led to presentations (not by us) at Wright Patterson AFB and an interest in establishing CRREL as a center of expertise and referral for all GPR detection of UXO related to lakes and ponds. We have also obtained a contract to prove our expertise in delineating the extent and depth of landfills surrounding JEP. Two examples of our results are shown in **Figures 34 and 35**. **Figure 34** shows the bathymetry derived from our profiles. We did this by picking the depths along the profiles. The map is a considerable improvement over the 10–15 depth sounding upon which the previous mapping was based. **Figure 35** shows the distribution of metal targets and/or probable UXO along our survey lines. The yellow lines indicate detected ordnance. The colored dots indicate ordnance protruding above the bottom and are color coded to indicate their height.

LEVERAGING AND COLLABORATION

We have been fortunate to have the help and/or collaboration of the following people and organizations.

1. Steve Thurmond, Range Control Officer, Fort Greely, AK (range access)
2. Capt. Timothy Brecheen, New Boston Air Force Station, New Boston, NH (range access)
3. Major Tracey Swope, New Boston Air Force Station, New Boston, NH (range access)
4. Prof. Michael Prentice, Plymouth State University (Squam Lake access and coring)
5. Prof. Tom Shevenelle, Plymouth State University (Squam Lake access)
6. Prof. Webjorn Karlen, Stockholm University, Sweden (Squam Lake coring apparatus)
7. Prof. Lanbo Liu, University of Connecticut (numerical modeling)
8. Prof. Benjamin Bostick, Dartmouth College (XRD diffraction)

9. Jason Keener, MS student, University of Connecticut (TDS calibration)
10. Dr. Steven Grant, ERDC-CRREL (TDS programming)
11. Ginger Boitnott, ERDC-CRREL (TDS data acquisition and grain size analysis))
12. Allan Delaney, ERDC-CRREL (Ft. Greely project assistance and UXO emplacement)
13. Arthur Gelvin, ERDC-CRREL (Ft. Greely, project assistance and UXO emplacement)
14. David Finnegan, ERDC-CRREL (GPS and transect mapping)
15. Dr. Sampath Iyengar, TM Company, Wildomar, California (XRD and grain size analysis)
16. Mr. Garry Kozak, private consultant, Salem, NH (side scan sonar survey)

PUBLICATIONS AND PRESENTATIONS

1. Arcone, S. A., Delaney, A. J., and Finnegan, D. C., 2006. Subbottom stratigraphy of frozen lakes on Alaskan artillery ranges. Published, *Proc., 11th Intl. Conf. on GPR*, Columbus, Ohio, June, 2006.
2. Keener, J. A., Grant, S. A., Arcone, S. A., Boitnott, G., and Liu, L., 2006. The use of modern Fourier transform methods to measure the dielectric permittivity of wet sediments. Published, *Proc., 11th Intl. Conf. on GPR*, Columbus, Ohio, June, 2006.
3. Keener, J. A., 2006, Time-domain based dielectric permittivity measurements of saturated sediments, M.S. thesis, Univ. Connecticut, Storrs, Conn.
4. Arcone, S. A., Finnegan, D. C. and Delaney, A. J., 2006. Quarter-wave Resonances within GPR profiles: Interaction between Targets and Stratigraphy beneath Shallow, Frozen Lakes. *Geophysics*, 71(6), K119–K131.
5. Arcone, S. A., 2006. Quarter wave resonances between targets and stratigraphic interfaces within GPR profiles of shallow frozen lakes. Abstract presented at *AGU Spring Mtg., Baltimore, MD, May 23, 2006.*
6. Arcone, S. A., 2007. GPR profiling of lacustrine stratigraphy with embedded targets: A case history of UXO detection. Abstract presented at *AGU Spring Mtg., Acapulco, MX, May 25, 2007.*
7. Arcone, S. A., 2007. Field observations of GPR signals propagating within lake water, and within lake beds containing UXO. Abstract presented at *International Union of Radio Scientists Annual Meeting*, Ottawa, CA, July, 2007.
8. Arcone, S. A., Grant, S. A., Boitnott, G., and Bostick, B., 2008. Complex permittivity and clay mineralogy of grain size fractions in a wet silt soil. *Geophysics*, 73(3), J1–J13.
9. Arcone, S.A., Grant, S.A. and Boitnott, G. E. 2008. Complex permittivity spectra of three clay minerals at low water contents. *Proc. 12th Intl. Conf. on Ground-Penetrating Radar*, Birmingham, UK, June, 2008.
10. In preparation: GPR profiling of lacustrine stratigraphy with embedded targets: a case history of UXO detection. To be submitted to The Leading Edge, the SEG (Society of Exploration Geophysicists) flagship publication. We are awaiting documentation of objects recovered during the magnetometer survey of July 7–12, 2008.

REFERENCES
(Note: some are not cited above but are cited in our publications)

Arcone, S.A., 1995, Numerical studies of the radiation patterns of resistively loaded dipoles: J. Applied Geophysics, **33**, 39–52.

Arcone, S. A. 2002. Airborne-radar stratigraphy and electrical structure of temperate firn: Bagley Ice Field, Alaska: J. Glaciology, **48**, 317–334.

Arcone, S.A., Lawson, D.E., Delaney, A.J., Strasser, J.C., and Strasser, J.D., 1998. Ground-penetrating radar reflection profiling of groundwater and bedrock in an area of discontinuous permafrost: Geophysics, **63**, 1573–1584.

Arcone, S. A. and Delaney, A. J., 2003. Radiowave pulse refraction and ground wave propagation through permafrost and the active layer: VIII International Conference on Permafrost, Proceedings, 21–26.

Arcone, S. A., A. J. Delaney, and P. Peapples, 2003, GPR pulse attenuation in a fine-grained and partially contaminated formation: Journal of Environmental Engineering Geophysics, **8**, 57−66.

Arcone, S. A., Finnegan, D. C., and Liu, L., 2006a, Target Interaction with stratigraphy beneath shallow, frozen lakes: Quarter-wave resonances within GPR profiles: Geophysics, **71**, pp. K119-K131.

Arcone, S. A., Finnegan, D. C., and Laatsch, J. E., 2006b, Bathymetric and subbottom surveying in shallow and conductive water: XI International Conference on Ground Penetrating Radar, Proceedings.

Arkhipov, V. I., 2002, Hierarchy of relaxation times in water: Journal of Non-Crystalline Solids, **305**, 127–135.

Barthel, J., K. Bachhuber, R. Buchner, and H. Hetzenauer, 1990, Dielectric spectra of some common solvents in the microwave region. Water and lower alcohols: Chemical Physics Letters, **165**, 369–373.

Berberian, J. G., and E. King, 2002, An overview of time domain spectroscopy: Journal of Non-crystalline solids, **305**, 10−18.

Bidadi, H., P. A. Schroeder, and T. J. Pinnavaia, 1988, Dielectric properties of montmorillonite clay films: Effects of water and layer charge reduction: Journal of the Physical Chemistry of Solids, **49**, 1435–1440.

Billings, M. P., 1955, Geologic map of New Hampshire: New Hampshire Development and Planning Commission, Concord, NH.

Calvet, R., 1975, Dielectric properties of montmorillonites saturated by bivalent cations: Clays and Clay Minerals, **23**, 257–265.

Chen, C.-C., and Peters, L., Jr., 1997, Buried unexploded ordnance identification via complex natural resonances: IEEE Transactions on Antennas and Propagation, **45**, 1645–1654.

Cole, K. S., and R. H. Cole, 1941 Dispersion and absorption in dielectrics. I. alternating current field: Journal of Chemical Physics, **9**, 341–351.

Cole, R. H., 1948, Underwater explosions: Dover Publications, NY (first published by Princeton University press).

Cole, R. H., J. G. Berberian, S. Mashimo, G. Chrysikos, and A. Burns, 1989, Time domain reflection methods for dielectric measurements: Journal of Applied Physics, **66**, 793−802.

Delaney, A.J., Sellmann, P.V. and Arcone, S.A., 1992, Sub-bottom profiling: A comparison of short-pulse radar and acoustic data: IVth International Conference on Ground Penetrating Radar, Proceedings, 149–157.

Dixon, J. B., and D. G. Schulze, Eds., 2002, Soil mineralogy with environmental applications: Soil Science Society of America, Madison, WI.

Doolittle, J. A., M. E. Collins, and J. R. Mount, 1998, Assessing the appropriateness of GPR with

a soil geographic database: Proceedings of the Seventh International Conference on Ground-Penetrating Radar, Lawrence, KS, 393–400.
Doolittle, J. A., F. E. Minzenmayer, S. W. Waltman, and E. C. Benham, 2002, Ground-penetrating radar soil suitability map of the conterminous United States: Proceedings of the Ninth International Conference on Ground-Penetrating Radar, Santa Barbara, CA, 7−12.
Falorni, P., Capineri, L., Masotti, L., and Pinelli, G., 2004, 3-D radar imaging of buried utilities by features estimation of hyperbolic diffraction patterns in radar scans: Xth International Conference on Ground Penetrating Radar, Proceedings, 403−406.
Fuchs, M., Beres, M., and Anselmetti, F.S., 2004, Sedimentological studies of western Swiss lakes with high-resolution reflection seismic and amphibious GPR profiling: Xth International Conference on Ground Penetrating Radar, Proceedings, 577−580.
Glasser, N., 1997, The origin and significance of sheet joints in Cairngorm granite: Scottish J. of Geology, **33**, 125–131.
Goldthwait, J. W., 1950, Surficial Geology of New Hampshire: New Hampshire State Planning and Development Commission, Concord, NH.
Grimley, D. A., 2000, Glacial and nonglacial sediment contributions to Wisconsin Episode loess in the central United States: Bulletin of the Geological Society of America., **112**, 1475−1495.
Hasted, J. B., 1973, Aqueous Dielectrics: Chapman and Hall.
Hilhorst, M. A., C. Dirksen, F. W. H. Kampers, and R. A. Feddes, 2001, Dielectric relaxation of bound water versus soil matric pressure: Soil Science Society of America Journal, **65**, 311−314.
Hoekstra, P., and A. J. Delaney, 1974, Dielectric properties of soils at UHF and microwave frequencies: Journal of Geophysical Research, **79**, 1699−1708.
Hoekstra, P., and W. Doyle, 1971, Dielectric relaxation of surface adsorbed water: Journal of Colloid and Interface Science, **36**, 513–521.
Holzhausen, G., 1989, Origin of sheet structure, 1. Morphology and boundary conditions: Engineering Geology, **27**, 225–278.
Ishida, T., T. Makino, and C. Wang, 2000, Dielectric-relaxation spectroscopy of kaolinite, montmorillonite, allophane, and imogolite under moist conditions: Clays and Clay Minerals, **48**, 75−84
Jahns, R., 1943, Sheet structure in granites: Its origin and use as a measure of glacial erosion in New England: J. of Geology, **2**, 71–98.
Kaatze, U., 1997, The dielectric properties of water in its different states of interaction: J. Solution Chemistry, **26**, 1049−1112.
Kaviratna, P. D., T. J. Pinnavaia, and P. A. Schroeder, 1996, Dielectric properties of smectite clays: Journal of the Physics and Chemistry of Solids, **57**, 1897–1906.
Keller, G. V., 1989, Electrical properties, In: Practical Handbook of Physical Properties of Rocks and Minerals, R. S. Carmichael, Ed.: CRC Press.
Knoll, M. D., and R. Knight, 1994, Relationships between dielectric and hydrogeologic properties of sand-clay mixtures: Proceedings of the Fifth International Conference on Ground-Penetrating Radar, Kitchener, Ontario, CA, 45–61.
Kunze, G. W., and J. B. Dixon, 1986, Pretreatment for Mineralogical Analysis: Methods of Soil Analysis, 2nd Ed., American Society of Agronomy-Soil Science Society of America, 91–100.
Li, J., and eight others, 2004, Extracting rebar reflection from measured GPR data: Xth International Conference on Ground Penetrating Radar, Proceedings, 367−370.
Likos, W. J., and N. Lu, 2002, Water vapor sorption behavior for smectite-kaolinite mixtures: Clays and Clay Minerals, **50**, 553–561.

Lyons, J.B., W. A. Bothner, R. H. Moench, and J. B. Thompson, Jr., 1997, Bedrock geologic map of New Hampshire: U. S. Department of the Interior, U. S. Geologic Survey.
Mashimo, S., T. Umchara, T. Ota, S. Kuwabara, N. Shinyashiki, and S. Yaihara, 1987, Evaluation of complex permittivity of aqueous solution by time domain reflectometry: Journal of Molecular Liquids, **36**, 135−151.
Meunier, A., 2004, Clays: Springer.
Mitchell, J. K., 1993, Fundamentals of soil behavior, 2nd Edition: John Wiley & Sons.
Moorman, B. J. and Michel, F. A., 1997, Bathymetric mapping and sub-bottom profiling through lake ice with ground-penetrating radar: J. Paleolimnology, **18**, 61–73.
Muhs, D. R., J. N. Aleinikoff, T. W. Stafford, Jr., R. Kihl, J. Been, S. A. Maha, and S. Cowherd, 1999, Late quaternary loess in northeastern Colorado: Part I-Age and paleoclimatic significance: Bulletin of the Geological Society of America, **111**, 1861−1875.
Njoku, E. G., and J.-A. Kong, 1977, Theory for passive microwave remote sensing of near-surface soil moisture: Journal of Geophysical Research, **82**, 3108−3118.
Olhoeft, G. R., 1989, Electrical properties of rocks; *in,* Physical Properties of Rocks and Minerals, Y. S. Touloukian, W. R. Judd, and R. F. Roy, eds.: Hemisphere.
Or, D., and J. M. Wraith, 1999, Temperature effects on soil bulk dielectric permittivity measured by time domain reflectometry: A physical model: Water Resources Research, **35**, 371−383.
Peplinski, N. R., F. T. Ulaby, and M. C. Dobson, 1995, Dielectric properties of soils in the 0.3–1.3-GHz range: IEEE Transactions on Geoscience and Remote Sensing, **33**, 803–807.
Péwé, T. L., 1955, Origin of the upland silt near Fairbanks, Alaska: Bulletin of the Geological Society of America, **67**, 699–724.
Porsani, J.L., Moutinho, L., and Assine, M.L., 2004, GPR survey in the Taquari River, Pantanal wetland, west-central Brazil: IVth International Conference on Ground Penetrating Radar, Proceedings, 593−596.
Robinson, D. A., 2004, Measurement of the solid dielectric permittivity of clay minerals and granular samples using a time domain reflectometry immersion method: Vadose Zone Journal, **3**, 705−713.
Rodbell, D. T., S. L. Forman, J. Pierson, and W. C. Lynn, 1997, Stratigraphy and chronology of Mississippi Valley loess in western Tennessee: Bulletin of the Geologic Society of America, **109**, 1134−1148.
Rotenberg, B., A. Cadéne, J.-F. Dufrêche, S. Durand-Vidal, J.-C. Badot, and P. Turq, 2005, An analytical model for probing ion dynamics in clays with broadband dielectric spectroscopy: Journal of Physical Chemistry, **109**, 15548–15557.
Sabburg, J., J. Ball, and N. Hancock, 1997, Dielectric behavior of moist swelling clay soils at microwave frequencies: IEEE Transactions on Geoscience and Remote Sensing*,* **35**, 784−786.
Sellmann, P.V., A.J. Delaney, and S. A. Arcone, 1992, Sub-bottom surveying in lakes with ground-penetrating radar: CRREL Report 92-8, 18 pp.
Shutko, A. M., and E. M. Reutov, 1982, Mixture formulas applied in estimation of dielectric and radiative characteristics of soils and grounds at microwave frequencies: IEEE Transactions on Geoscience and Remote Sensing, **GE-20**, 29–32.
Sposito, G., and R. Prost, 1982, Structure of water adsorbed on smectites: Chemical Reviews, **82**, 554–573.
Sulfredge, C. D., R. H. Morris, and R. L. Sanders, 2005, Calculating the effect of surface or underwater explosions on submerged equipment and structures, proc. ANS International Topical Meeting on Probabilistic Safety Analysis (PS ’05), San Francisco, CA, Sept 11–15, 2005.
Swisdak, M. M., 1978, Explosion effects and properties: Part II-Explosion effects in water: NSWC/WOL/TR 76-116, Naval Surface Weapons Center, Dahlgren, VA.

Van Dam, R. L., W. Schlager, M. J. Dekkers, and J. A. Huisman, 2002, Iron oxides as a cause of GPR reflections: Geophysics, **67**, 536–545.
Von Hippel, A. R., 1954, Dielectrics and Waves: John Wiley & Sons.
Wharton, R. P., G. A. Hazen, R. N. Rau, and D. L. Best, 1980, Electromagnetic propagation logging: advances in technique and interpretation: Paper 9267, Society of Petroleum Engineers.